Entorhinal cortex vulnerability to human APP expression promotes hyperexcitability and tau pathology

Annie M Goettemoeller[1,2], Emmie Banks[1,2], Prateek Kumar[3], Viktor J Olah[1], Katharine E McCann[4], Kelly South[1,2], Christina C Ramelow[2,5], Anna Eaton[6], Duc M Duong[5,8], Nicholas T Seyfried[5,7,8], David Weinshenker[4], Srikant Rangaraju[3#] & Matthew JM Rowan[1,8*#]

[1]Department of Cell Biology, Emory University School of Medicine, Atlanta, GA, 30322
[2]GDBBS Graduate Program, Laney Graduate School, Emory University
[3]Department of Neurology, Yale University, New Haven, CT 06510
[4]Department of Human Genetics, Emory University School of Medicine
[5]Department of Neurology, Emory University School of Medicine
[6]Department of Biomedical Engineering, Georgia Institute of Technology, Atlanta, GA 30322
[7]Department of Biochemistry, Emory University
[8]Center for Neurodegenerative Disease, Emory University School of Medicine

# Denotes co-corresponding authorship

***Address for Correspondence:**

Matthew JM Rowan, PhD
Emory University School of Medicine
Department of Cell Biology
Atlanta, GA 30322
Email: mjrowan@emory.edu

Srikant Rangaraju, MD
Yale University
Department of Neurology
New Haven, CT 06510
Email: srikant.rangaraju@yale.edu

Keywords: APP; inhibition; PV interneuron; hyperexcitability; lateral entorhinal cortex; Alzheimer's Disease

Abstract

Preventative treatment for Alzheimer's Disease is of dire importance, and yet, cellular mechanisms underlying early regional vulnerability in Alzheimer's Disease remain unknown. In human patients with Alzheimer's Disease, one of the earliest observed pathophysiological correlates to cognitive decline is hyperexcitability. In mouse models, early hyperexcitability has been shown in the entorhinal cortex, the first cortical region impacted by Alzheimer's Disease. The origin of hyperexcitability in early-stage disease and why it preferentially emerges in specific regions is unclear. Using cortical-region and cell-type-specific proteomics coupled with *ex vivo* and *in vivo* electrophysiology, we uncovered differential susceptibility to human-specific amyloid precursor protein (hAPP) in a model of sporadic Alzheimer's. Unexpectedly, our findings reveal that early entorhinal hyperexcitability may result from intrinsic vulnerability of parvalbumin (PV) interneurons, rather than the suspected layer II excitatory neurons. This vulnerability of entorhinal PV interneurons is specific to hAPP, as it could not be recapitulated with increased murine APP expression. However, partial replication of the findings could be seen after introduction of a murine APP chimera containing a humanized amyloid-beta sequence. Surprisingly, neurons in the Somatosensory Cortex showed no such vulnerability to adult-onset hAPP expression. hAPP-induced hyperexcitability in entorhinal cortex could be ameliorated by enhancing PV interneuron excitability *in vivo.* Co-expression of human Tau with hAPP decreased circuit hyperexcitability, but at the expense of increased pathological tau species. This study suggests early disease interventions targeting non-excitatory cell types may protect regions with early vulnerability to pathological symptoms of Alzheimer's Disease and downstream cognitive decline.

Introduction

Alzheimer's Disease (AD) is the most prevalent neurodegenerative disease, yet current treatments are unable to prevent its initiation and progression. Although brain regions of early vulnerability have been known for over 30 years[1], our understanding of what makes certain areas more susceptible remains unknown. The first cortical region to display pathology and degeneration in AD is the Lateral Entorhinal Cortex (LEC)[1-4]. Notably, landmark studies identified Layer II (LII) neurons cells as highly vulnerable to early neurodegeneration with up to 60% cell death in mild AD patients and up to 90% in severe cases[2]. More recently, LII LEC principal neurons were also characterized as a cell population exhibiting amyloid pathology[4]. However, the distinctive features that impart vulnerability to neurons in the LEC AD remain unclear. Uncovering region-specific cellular mechanisms could improve our understanding of the initiating factors in the AD cascade and are imperative in determining potential interventions at a time when subsequent cognitive decline and neurodegeneration might still be prevented.

Hyperexcitability is one of the earliest pathophysiological biomarkers in the human AD brain, and its emergence correlates with severity of cognitive decline in individuals[5]. Hyperexcitability is also observed in recordings from *in vivo* and *in vitro* models of AD pathology[6-12], arising prior to amyloid plaque deposition[13] and likely contributing to spine degeneration[14]. Interestingly, hypermetabolism[15] and hyperexcitability[9,16] emerged in the LEC of a sporadic AD mouse model before spreading to other regions[3]. It is unclear whether cell-intrinsic changes in principal neuron excitability or other forms of circuit dysfunction are responsible for aberrant LEC activity in early AD. Hyperexcitability may also arise due to changes in local circuit inhibition from GABAergic interneurons, with several lines of evidence demonstrating impaired inhibitory tone[6,9,15], most notably from fast-spiking parvalbumin+ (PV) interneurons[7,10,13]. Whether the basal properties of PV interneurons in the LEC confer functional vulnerability with respect to PV cells in other regions is unknown. Thus, observing baseline cellular and regional differences coupled with adult-onset, region-specific APP or Tau expression is imperative to properly dissect inherent vulnerabilities underlying susceptibility of the LEC to early AD pathology.

Results

PV interneurons in an AD-vulnerable region are functionally and molecularly distinct

103 We first compared active and passive features of excitatory neurons in AD-vulnerable and non-
104 vulnerable cortical regions. Excitatory neurons in LII of Lateral Entorhinal Cortex (LEC) (highly
105 vulnerable to early AD pathology[4]) and L5 pyramidal cells (PCs) in Somatosensory Cortex (SS
106 Ctx) of wild type (WT) mice were chosen for comparison, as each represent projection output
107 neurons and are innervated by similar dominant inhibitory networks[17]. Despite differences in their
108 dendritic anatomy, axonal projections, and overall local circuit operations, these two cell types
109 showed striking overlap in their firing capacity, AP waveforms, and most other biophysical
110 features (Fig 1a-c), with only slight biophysical differences noted (Extended Data Table 1).
111 Because different cortical regions perform operations over non-overlapping frequency domains,
112 we hypothesized that differences in the intrinsic excitability of inhibitory interneurons might help
113 tune circuit activity locally. Thus, we assessed physiological phenotypes of 'fast-spiking' PV
114 interneurons in each region, using an unbiased, PV-specific enhancer-AAV fluorescent targeting
115 approach[18]. In the LEC, the E2 enhancer displayed high overlap (92.62±5.7%) with PV+ somas
116 from the previously established mouse model, PV-tdTom (Extended Data Fig. 7a,b). Surprisingly,
117 PV interneurons in the LEC maximally fired at only half the rate of SS Ctx PV interneurons (Fig.
118 1d,e), likely due to their far broader action potentials with respect to PV interneurons recorded
119 from SS Ctx (Fig. 1f-h)[17]. The first action potential of each AP train was also larger in amplitude
120 in the LEC PV interneurons (Fig. 1f-h). Furthermore, resting membrane potential and AP threshold
121 were significantly different for PV cells when compared by region (Extended Data Table 1,
122 bottom). Despite expressing similar passive features in LEC and SS Ctx (e.g., membrane
123 capacitance; 70.17 ± 5.46 pF vs. 71.91 ± 9.51 pF; LEC vs SS respectively, Extended Data Table
124 1), their starkly divergent excitability suggests unique molecular signatures which may also
125 underlie differential vulnerability in AD and other diseases.
126
127 We next sought to examine differences in the molecular signature of PV interneurons in each of
128 these regions. Single-neuron transcriptomics is a sound method for uncovering molecular diversity
129 between different brain cell types. Nonetheless, the functional relevance of these studies is limited
130 by substantial discordance between mRNA and protein in neurons[19]. Thus, we opted to isolate the
131 native-state proteomes of PV interneurons from each region using our recently developed neuron-
132 type-specific TurboID method[20] (Fig. 1i). This was achieved through systemic AAV injections to

133 achieve whole-cortex expression of a PV-specific, Cre-expressing enhancer-AAV in
134 Flex.TurboID mice[21] followed by region-specific microdissection (Fig. 1i; Extended Data Fig. 1a).
135 Flex.TurboID mice express an engineered biotin ligase (TurboID) in a cell-specific manner. After
136 recombination, TurboID will efficiently label the extranuclear proteins in cell types of interest.
137 Thus when coupled with subdissection, region- and cell-specific proteomic analyses can be
138 performed. Over 800 proteins were biotinylated in PV interneurons in each region, of which nearly
139 two hundred proteins showed region-specific differential abundances (unadjusted $p<0.05$ n=207;
140 n=185 below the permFDR 0.05 threshold; Extended Data Datasheet 1; Fig. 1j). Generally, LEC
141 PV interneuron proteomes showed biased enrichment in transmembrane and synaptic ion channels
142 and transporters, while SS PV interneuron proteomes showed biased enrichment in microtubule
143 binding, glycolysis, and fatty acid metabolism-related proteins (Extended Data Fig. 1b).
144

145 **Relationships between PV interneuron proteomic signatures with cognitive resilience in**
146 **human AD**

147 We next considered whether PV interneuron proteins differentially expressed by region (Fig. 1j)
148 were representative of proteins associated with cognitive stability during aging. To achieve this,
149 we used data from a protein-wide association study of cognitive resilience from human brain
150 samples (Religious Orders Study and the Rush Memory and Aging Project; 'ROSMAP'[22]). In this
151 study, rate of cognitive decline (cognitive slope) was correlated with post-mortem brain protein
152 levels quantified by mass spectrometry, identifying proteins positively associated with cognitive
153 stability (pro-resilience proteins) and those negatively associated with cognitive stability (anti-
154 resilience proteins) (Fig. 1k). We found that wild-type LEC PV interneurons displayed
155 significantly more 'pro-resilience'-associated proteins as compared to SS Ctx PV interneurons
156 ($p=0.0011$; Mann-Whitney test; Fig. 1k). As nearly all the LEC PV interneuron enriched proteins
157 were associated with cognitive stability during aging, we next explored whether expression of
158 these enriched proteins was perturbed throughout stages of AD pathology.
159

160 We examined whether expression of these enriched proteins was perturbed throughout stages of
161 AD pathology in humans. While several proteomics surveys of post-mortem brain tissues from
162 AD and control brain have been performed, few studies have published data comparing the
163 entorhinal cortex (EC) to neocortical regions, such as the frontal cortex (FC). This is true

164 particularly regarding disease staging. In a recent study[23], EC and FC regions from post-mortem
165 brains of control and AD cases (BRAAK stages I-III [early] and IV-VI [late]) were analyzed by
166 quantitative MS. This yielded 737 differentially-enriched proteins (DEPs) comparing AD to
167 control, at either early (BRAAK I-III) or late (BRAAK IV-VI) stages, which were significant in
168 either EC or FC regions. Among these, 93 human DEPs were observed in our PV-CIBOP proteome
169 (Extended Data Fig. 2a, Extended Data Datasheet 2). Of these, 23 proteins showed differential
170 levels in SS Ctx PV-INs as compared to LEC PV-INs (Extended Data Fig. 2b). Surprisingly, of
171 the regional PV-IN proteins that were altered in human AD brain, many were pro-resilience
172 proteins. Importantly, the LEC-enriched PV-IN proteins (including pro-resilience proteins)
173 showed decreased levels in the EC of human AD cases (Extended Data Fig. 2b). Thus, resilience
174 factors in PV-INs of the entorhinal cortex may be lost as AD pathology advances.
175
176 Based on observed associations between regional proteomic signatures of PV interneurons with
177 cognitive resilience and with early changes occurring in human AD brain, we further assessed
178 relationships between regional proteomic signatures of PV interneurons with APP and Tau protein-
179 protein interactomes. Many APP-interacting proteins have been identified. Of 243 APP interactors
180 identified from physical protein-protein interactors listed in the STRING database, 31 APP
181 interactors were identified in PV-CIBOP proteomes. From these, 14 proteins were highly enriched
182 regionally in PV interneurons. 10 proteins were highly enriched in SS Ctx PV interneurons
183 (including Numbl, Snca, Mapt, Bin1, Hspd1, Hspa4, Hspa8, Eno1, Gapdh, Mapk3) (Extended
184 Data Fig. 3a) and 4 were enriched in LEC PV-INs (Apoo, Grin1, Clstn1, Grin2a) (Extended Data
185 Fig. 3a, Extended Data Datasheet 3). However, these physical associations may be altered in AD
186 with either altered APP expression or mutations in the APP gene.
187
188 In a consensus analysis of tau protein interactors[24], over 2000 tau protein interactors were
189 identified across seven human post-mortem proteomics studies. Of these, 261 proteins were
190 identified consistently as interactors (represented in at least three of the studies), comprising a
191 high-confidence list of tau interactors. These proteins, as previously described[24], were enriched in
192 proteins involved in protein translation, mRNA processing and splicing, protein folding,
193 intracellular transport, proteasome assembly, and glycolysis. In our work, 107 of these were
194 labeled by CIBOP in PV interneurons (Extended Data Datasheet 3,4). Of these, 32 proteins had

195 higher levels in SS Ctx PV interneurons, 8 with higher levels in LEC PV interneurons, while 67
196 did not show regional differences (Extended Data Fig. 3b). In contrast, non-tau interactors were
197 more evenly distributed across SSC and LEC PV interneurons. This result suggests that tau
198 interactors are present at higher levels in PV-INs located in the SS Ctx as compared to those in the
199 LEC (Chi square statistic 20.7, p=0.00032). This seems to be consistent with higher levels of
200 MAPT in SS Ctx PV interneurons as well. Tau interactors in SS Ctx PV interneurons included 14-
201 3-3 proteins, heat shock proteins, extracellular vesicle proteins, actin/cytoskeletal proteins and
202 RNA binding proteins. Whether the higher abundance of MAPT and tau interactors in SS Ctx PV
203 interneurons influences the circuit's resilience to hyperexcitability at early time points is unclear.
204 To further explore differential responses of PV interneurons between the LEC and neocortex, we
205 utilized a model of adult-onset induction of AD-related pathology which could be regionally and
206 temporally controlled.
207
208 **Adult-onset human APP expression reduces PV interneuron excitability specifically in LEC**
209 Traditional rodent models of AD express various (typically mutant) forms of hAPP (and related
210 processing proteins), with transgene expression beginning while neuronal circuits are still
211 maturing, and also in a brain-wide fashion. To eliminate the substantial network effects of hAPP
212 during development[25] and to assess inherent vulnerability of individual areas independently, we
213 used an adult-onset, region-specific AAV approach. To explore whether differences in basal
214 excitability and proteomic signatures of PV interneurons described early conferred region-specific
215 vulnerability in an AD pathology context, we virally expressed wild-type hAPP in either the LEC
216 or SS Ctx in 8-12 week old (adult) mice. Full length hAPP (hAPP 770) (NM_000484.4), an
217 isoform showing increased expression in human AD[26,27] was expressed using the pan-neuronal
218 EF1a promoter (Figure 2a; AAV.Ef1a.hAPP). We assessed the impact of this hAPP isoform on
219 PV interneurons in the LEC and SS Ctx independently after 2-3 weeks of expression.
220
221 In LEC PV interneurons, we observed a dramatic reduction in PV interneuron firing (Fig. 2b,c)
222 potentially related to a reduction in input resistance (Fig. 2d), as no other relevant factors (e.g., AP
223 waveform, RMP, AP threshold, Membrane capacitance) (Fig. 2d; Extended Data Fig. 4) were
224 affected. Using unsupervised clustering of LEC 'fast-spiking' interneuron biophysical features,
225 control- and hAPP-expressing PV interneurons clustered separately (Extended Data Fig. 12b). By

226 contrast, PV interneurons in the SS Ctx displayed no change in firing rate (Fig. 2g) despite an
227 increase in the AP AHP (Extended Data Fig. 5d). All other active and passive features were
228 unchanged in SS Ctx (Fig. 2h; Extended Data Fig. 5b-e). The presence of hAPP mRNA and protein
229 was confirmed in PV neurons 2-3 weeks after viral injection (Fig. 2i-j; Extended Data Fig. 6) using
230 RNAscope and PV-specific flow cytometry respectively. Together, the intrinsic excitability of PV
231 interneurons was significantly reduced in the LEC, but not SS Ctx, following hAPP expression.
232

233 **Adult-onset murine APP expression does not affect PV interneuron physiology**

234 Several studies of different mouse models of APP-related pathology report altered intrinsic
235 excitability in GABAergic intereneurons[7-10,13]. Whether this is simply a result of hAPP
236 overexpression[28] during development or effects of its downstream cleavage products remain
237 controversial. To address this, we next injected a virus containing full-length murine APP (mAPP)
238 (NM_001198823.1) (Fig. 3a; AAV.Ef1a.mAPP) into the LEC. Despite a significant increase of
239 mAPP expression over endogenous background levels (Extended Data Fig. 8d,e), changes in PV
240 interneuron firing and input resistance seen following hAPP expression (Fig. 2) were absent
241 following 2-3 weeks of viral mAPP expression (Fig. 3b,c; Extended Data Fig. 8b,c). Importantly,
242 RNAscope studies confirmed that the magnitude of AAV-induced mAPP expression was similar
243 to that of hAPP in earlier experiments (Figure 3d), indicating that the differential physiological
244 effects were not due to variability in APP expression levels. Furthermore, as we saw no alterations
245 in the somatosensory cortex PV-interneurons after hAPP expression, we conclude this differing
246 response is not due to a specific inflammatory effect of the human protein alone. Thus, hAPP-
247 induced dysfunction of LEC PV interneurons cannot be explained by over-expression of APP
248 alone.
249

250 **Murine APP with a humanized amyloid-beta sequence moderately impairs PV interneurons**

251 We next investigated whether the effect of hAPP on PV interneuron function could be explained
252 by the differences in the amyloid-beta sequence of the human and mouse genes. To address this,
253 we cloned the full-length murine APP (mAPP) (NM_001198823.1) but humanized the three
254 differing amino acids in the amyloid-beta sequence, G676R, F681Y, and R684H (Fig. 3e;
255 AAV.Ef1a.mAPP/hAβ Chimera). After AAV-directed expression of this APP Chimera in the LEC
256 for 2-3 weeks, we observed a reduction in PV interneuron firing (Fig. 3f,g). However, the

mAPP/hAβ effect was less robust when compared to the fully human version (Fig. 3h; Extended Data Fig. 9d) and appeared to manifest in a mechanistically distinct fashion relative to hAPP (Extended Data Fig. 9). Thus, the contribution of the human amyloid-beta sequence leads to PV-interneuron hypofunction, but was not sufficient to induce the more drastic reduction seen with full-length human hAPP. Finally, to further evaluate a role Aβ in this process, we tested the effect of exogenous Aβ ($A\beta_{1-40,1-42}$; 0.25μM; 3 hours) incubation on PV interneurons in the LEC. Similar to hAPP, Aβ incubation alone also induced a robust reduction in AP firing (Extended Data Fig. 9f).

Adult-onset human APP expression does not affect excitatory cell intrinsic properties

Because recent studies using different mouse models of APP/Aβ pathology report altered intrinsic excitability of excitatory neurons[25,29], we also assessed the effects of 2-3 weeks of hAPP expression on principal excitatory cells in the LEC and SS Ctx (Fig. 4a,e). Consistent with unaltered PV firing in SS Ctx, no change in intrinsic firing frequency or passive properties were noted in pyramidal cells in the SS Ctx (Fig. 4f-h; Extended Data Fig. 11). Surprisingly, we also observed no impact of hAPP on intrinsic AP firing of LII LEC excitatory neurons (Fig. 4b,c). Further, membrane capacitance was unperturbed (Fig. 4d) suggesting no major alterations to LII cellular morphology. A modest but significant increase in dV/dt max was noted in LEC LII principal cells (Extended Data Fig. 10d), potentially via an hAPP-dependent modulation of Na_v channels in these cells. All other active and passive properties were unaltered (Fig. 4d; Extended Data Fig. 8). Importantly, RNAscope experiments confirmed increased hAPP expression in CaMKIIa+ cells (Fig. 4i-j), indicating that our AAV also targeted excitatory neurons as expected. Using principal component analysis (PCA) of several excitatory cell biophysical features from LEC recordings, clusters could be separated based on input resistance, membrane time constant, and resting membrane potential. These clusters likely arise due to sampling of both LII fan cells and LII pyramidal cells[30], suggesting our population of principal cells likely included both cell types (Extended Data Fig. 12a). When assessed, these excitatory populations showed no differential clustering when expressing hAPP (Extended Data Fig. 12a). Together, these results indicate that principal neurons are more resistant to changes in their intrinsic excitability following adult-onset hAPP expression compared to PV interneurons.

288 **hAPP expression induces basal circuit hyperexcitability in the LEC but not SS Cortex**

289 Although we observed no alterations in the intrinsic excitability of excitatory cells in either region
290 following hAPP expression, we wanted to assess whether the changes in PV interneuron
291 biophysics in LEC had an impact on local circuit activity. To examine this at population level, we
292 acquired spontaneous post-synaptic currents from principal cells in either region (Fig. 5a,d). In the
293 LEC, spontaneous inhibitory event (sIPSC) frequency was significantly decreased (increase in the
294 mean inter-event interval [IEI]) after 2-3 weeks of hAPP expression (Fig. 5b,c). Furthermore, we
295 analyzed the LEC sIPSCs for differences in the frequency in small and large amplitude events
296 (cutoff 40 pA derived from a previously published method[31]), to determine if the increase in sIPSC
297 IEI was related to distal inhibition (small amplitude) or proximal, peri-somatic inhibition (large
298 amplitude). We observed that while the frequency of small amplitude events was unchanged
299 ($p=0.52$, two-tailed unpaired t-test, $t=0.65$, $df=18$; Ctrl: 1.66±0.36 Hz, hAPP: 1.33±0.35 Hz), the
300 frequency of large amplitude events was significantly decreased in the LEC ($p=0.02$, two-tailed
301 unpaired t-test, $t=2.51$, $df=18$; Ctrl: 4.66±1.1 Hz; hAPP: 1.74±0.49 Hz), indicating a selective
302 effect on peri-somatically innervating inhibitory neurons. In layer II of the entorhinal cortex,
303 Reelin+ excitatory cells receive peri-somatic inhibition primarily from PV interneurons, rather
304 than CCK basket cells[17,32]. Thus these results are consistent with a reduction in intrinsic PV
305 excitability. In an apparent response to this reduced inhibitory tone, spontaneous excitatory event
306 (sEPSC) frequency increased in the LEC following hAPP expression (Fig. 5b,c). In contrast to the
307 LEC, recordings from SS Ctx (Fig. 5d,e) revealed no change in sIPSC or sEPSC frequency
308 following hAPP expression (Fig. 5f), in agreement with the lack of changes in intrinsic excitability
309 in the SS Ctx shown earlier. Spontaneous and miniature (excitatory or inhibitory) synaptic
310 amplitudes in the LEC and SS Ctx were unchanged in either region (Extended Data Fig. 13),
311 indicating that postsynaptic receptor alterations did not arise in excitatory neurons following short-
312 term adult-onset hAPP expression. mIPSC and mEPSC frequencies were also unaltered,
313 suggesting no change in the number of inhibitory or excitatory synapses at this point (Extended
314 Data Fig. 13b). Together, these results indicate that basal circuit activity in the LEC, but not SS
315 Ctx, becomes hyperexcitable following short-term hAPP expression, likely resulting from a
316 region-specific PV interneuron vulnerability.

317

318 **hAPP-induced network dysfunction is attenuated following PV interneuron activation *in vivo***

319 To understand how short-term expression of hAPP affected network behavior *in vivo*, we next
320 performed local field potential (LFP) recordings in the LEC of lightly anesthetized, head-fixed
321 mice 3 weeks after injection of hAPP or control (tdTom) virus (Fig. 6a-c). As predicted by our *ex*
322 *vivo* studies, we found a broad increase in activity across several frequency domains, similar to
323 previous findings in the LEC of a sporadic AD model[15]. Notably, the delta, theta, and low gamma
324 frequency domains showed significant increases in power (Fig 6e) indicating increases in neuronal
325 activity[33] (Extended Data Fig. 14b). Despite following a similar trend, frequency domains above
326 80 Hz (i.e., high Gamma and beyond) were not significantly altered (Fig. 6e, Extended Data Fig.
327 14b). Together with our mechanistic evaluations earlier, this suggests that hAPP-induced PV
328 interneuron dysfunction induces network hyperexcitability *in vivo*.
329 We next asked whether 'real-time' enhancement of PV interneuron excitability could
330 ameliorate hAPP-induced network hyperexcitability *in vivo*. To accomplish this, PV interneurons
331 in the LEC were activated chemogenetically using the E2 PV-specific targeting enhancer[18] to
332 express hM3Dq.DREADD (Gq.DREADD). For DREADD experiments, groups are denoted as
333 either Ctrl (Gq.DREADD/no hAPP) or hAPP (Gq.DREADD + hAPP) (Fig. 6f,h,j). Remarkably,
334 chemogenetic activation of PV interneurons with low-dose CNO (0.5mg/kg) could rapidly restore
335 the hyperexcitable LFP in hAPP-expressing mice to Ctrl levels (Fig. 6g,h) most notably in the
336 delta (Fig. 6i) and theta (Fig. 6k). Perhaps surprisingly, 0.5mg/kg CNO did not significantly reduce
337 LFP power in Ctrl (no hAPP) animals with respect to saline. Importantly, DREADD expression
338 itself or CNO administration without DREADD expression did not alter LFP power in either the
339 Ctrl or hAPP animal groups (Extended Data Fig. 14c,d). Thus chemogenetic enhancement of PV
340 interneurons in the LEC was sufficient to completely rescue the hAPP-induced hyperexcitability
341 *in vivo.*
342
343 **hTau co-expression with hAPP quells LEC hyperexcitability at the cost of increased**
344 **pathological tau species**
345 Beyond hyperexcitability, the LEC is also the first cortical region to develop tau pathology[1,34-37].
346 Although Alzheimer's is characterized by early hAPP/Aβ and later Tau pathology, respectively,
347 the relationship between hAPP, hyperexcitability, and Tau remains unclear. It has previously been
348 established that artificially increasing neuronal activity can accelerate tau pathology[38-40]. However,
349 long-term transgene expression of human Tau (hTau) may act to dampen circuit excitability[16,41,42]

350 (but see[43]). Thus, we sought to assess the interplay of hAPP-induced circuit hyperexcitability and
351 hTau expression in the LEC. To achieve this, we packaged full-length wild-type human Tau (hTau)
352 into a separate AAV to induce Tau expression locally in the entorhinal cortex. Spontaneous post-
353 synaptic currents were then recorded from LII principal cells, 3 weeks after hAPP alone, hTau
354 alone, or hAPP + hTau co-injection (Fig. 7a). With hAPP, we again observed an elevated E:I
355 frequency ratio (sEPSC frequency/sIPSC frequency, normalized to the Control dataset) as
356 described earlier (Fig. 7b). We hypothesized that hTau would result in a reduced E:I ratio with
357 respect to the control baseline. Although the E:I ratio with hTau alone was less than hAPP alone,
358 E:I balance surprisingly remained unchanged with respect to the Control (Fig. 7b). However, hAPP
359 + hTau resulted in an intermediate effect, which abolished the hyperexcitable phenotype seen with
360 hAPP alone (Fig. 7b). These results agree with a homeostatic role for Tau in maintaining circuit
361 excitability. Beyond synaptic event frequencies, all other spontaneous event properties (i.e.,
362 amplitude) were statistically similar between all groups (Extended Data Fig. 15a,b).
363
364 We next assessed whether the moderating effect of hTau on circuit activity came at the cost of
365 increased pathology, using antibodies for pSer202/pThr205 phosphorylated tau (AH36) or
366 oligomeric tau (T22). Both Control and hAPP-injected conditions showed low levels of AH36
367 positivity, likely due to endogenous labeling of murine tau (Extended Data Fig. 15c,d). While both
368 hTau and hAPP+hTau induced high levels of AH36-positive staining (Fig. 7c,d), it appeared that
369 hTau alone injected mice had mostly somatically located staining. In contrast, hAPP+hTau co-
370 injected mice displayed disperse staining (Fig. 7c) suggesting an interaction with hAPP which
371 promotes extracellular transport of pathological Tau. Oligomeric tau (T22) (Fig. 7e), which has
372 recently been shown in human tissue as a tau species that may spread transsynaptically from axons
373 to other regions[44], displayed a surprisingly robust increase, but only when hAPP+hTau were co-
374 expressed (Fig. 7e,f; Extended Data Fig. 15e,f). Thus, it appears that co-expression of Tau could
375 help restore APP-induced circuit hyperexcitability. However, a consequence of their co-expression
376 appears to be the amplification and translocation of known pathological tau species.
377
378 **Discussion**
379 Here we demonstrate that PV interneurons within the LEC are biophysically distinct from other
380 neocortical PV interneurons. Furthermore, differences in the native-state proteomes of PV

381 interneurons from the LEC and SS Ctx regions were marked. Although the WT PV firing
382 frequency in our LEC recordings is consistent with previous obervations[17], the striking biophysical
383 differences (i.e., AP waveform) with respect to PV cells in other cortical regions had not been
384 systematically evaluated. Interestingly, these LEC PV interneurons do resemble a previously
385 observed PV+ interneuron in other regions, such as the 'quasi fast-spiking interneurons' of the
386 subiculum[45], the 'fast-spiking-like cells' of the striatum[46], and the 'non-fast-spiking interneurons'
387 of the CA1[47]. However, where these cells represent a small subset of the PV+ interneurons of these
388 regions (~20% in CA1)[47], the majority of our recorded PV+ interneurons displayed this low-firing
389 phenotype. Whether the baseline low-firing frequency of PV+ interneurons in the LEC confers
390 vulnerability to hAPP-induced pathophysiology remains unclear. In addition to their different
391 intrinsic features, PV interneurons of the LEC displayed a multitude of differentially expressed
392 proteins in comparison to SS Ctx PV interneurons. Interestingly, compared to SS, we found that
393 PV interneurons residing in the LEC were significantly enriched in proteins associated with
394 cognitive resilience in humans. However, many of these LEC PV-IN pro-resilience proteins were
395 altered in the entorhinal cortex of AD patients. This suggests a regional and cell-type-specific
396 susceptibility to the progression of AD pathophysiology. Although a comparison of PV-CIBOP
397 regional proteomes with bulk human brain proteomes gives further insight into potential cell-type-
398 specific alterations in phases of AD, it is still limited by the inability to verify PV interneuron-
399 specificity of observed changes in human brain. As we only recently established the first, to our
400 knowledge, PV interneuron-specific proteome[21], we look forward to the advancement of
401 techniques to come in order to complete such a level of analysis in human tissue. Future studies at
402 the single-cell level in humans with early-stage AD will be necessary to confirm this assertion.
403
404 Recent work shows that APP expression moves outside of normal homeostatic levels in models of
405 late-onset AD risk alleles[48,49]. The ratio of different APP isoforms also shifts in human AD, from
406 mainly APP 695 to increasing levels of APP 770 and 751[26,27]. These longer isoforms show
407 increased expression following aging-related processes (e.g., after reproductive hormonal
408 production decline[50], hypercholesterolemia[51], and atherosclerosis[52]), all of which are also
409 associated with increased AD risk[53-56]. Thus, here we induced adult-onset expression of hAPP 770
410 to model these phenomena. Adult-onset expression of hAPP allowed us to avoid any alterations to
411 neurodevelopment which may arise with expression of a transgene early in development, as many

412 mouse models of AD exhibit. However, we acknowledge that this model does not encapsulate all
413 alterations that may arise throughout aging and early Alzheimer's Disease. Thus, further studies
414 must be conducted to assess these mechanisms in aging mice. At this time point, we found that
415 shortly after hAPP expression (2-3 weeks), LEC PV interneuron firing became severely disrupted.
416 Although viral hAPP expression was robust in both excitatory and inhibitory cells due to the
417 generic promoter used to express hAPP in our experiments, we observed no alteration to the
418 intrinsic excitability of excitatory cells in LEC LII. Despite this, there was a significant disruption
419 in the E:I balance in LEC slices. Thus, we propose basal network hyperexcitability observed arises
420 as a result of decreased PV-interneuron firing, resulting in a loss of tonic inhibition and thus,
421 increased firing propensity of surrounding excitatory neurons. Notably, our hAPP condition
422 displayed a large peak in LFP power in the delta frequency domain (1-4 Hz) *in vivo*, which was
423 returned to baseline upon rescue of PV interneuron excitability. This delta peak may represent
424 increased low-frequency excitatory neuron synchronicity. We also observed a broadband increase
425 in most other frequency ranges in the hAPP condition, including gamma power, which has been
426 previously described in AD patients[57] and in amyloid pathology mouse models[13].

427 Of the 26 amino acids differentiating the hAPP and mAPP proteins, only 3 are situated
428 within the amyloid-beta region. Of note, of the 'wild-type' versions of newly designed hAPP
429 knock-in mouse models[58,59] now in wide use, only the 3 amino acids within the amyloid region are
430 humanized. It has been shown that expression of WT hAPP can result in a substantial increase in
431 amyloid-beta[60], suggesting that PV interneuron hypofunction in the LEC phenotype results directly
432 from Aβ accumulation. Thus, we investigated if humanizing only the 3 amino acids could
433 recapitulate our findings of hAPP-induced impaired PV interneuron physiology. Interestingly, the
434 mAPP/hAβ Chimera did result in impaired PV-interneuron firing, but did not replicate the more
435 drastic alterations seen with full-length hAPP expression. This suggests amyloid-beta is not the
436 sole cause for early phase interneuron dysfunction, and may suggest a role for either full-length
437 APP or its other cleavage products in this stage of the neurodegenerative cascade. Alternatively,
438 the full-length hAPP may result in enhanced Aβ production with respect to the mAPP/Aβ chimera.

439 GABAergic interneurons require homeostatic APP levels for proper physiological function
440 and circuit activity control[61]. Furthermore, APP[62], as well its cleavage proteins[63-65] and
441 products[66,67], can modulate neuronal biophysics and alter the expression of ion channels, many of
442 which are essential for maintaining the 'fast-spiking' phenotype of PV interneurons. Modifications

443 to Na_v1 or K_v3 channel availability in different constitutive hAPP-expressing mice have recently
444 been linked to reduced PV excitability[7,13]. Although short-term full-length hAPP expression in this
445 study could significantly reduce PV firing, we observed no outward biophysical indicators
446 implicating changes to either Na_v1 or K_v3 availability which could underlie altered PV firing in
447 the LEC. However, this likely requires further evaluation of specific ion channel subtypes.
448 Although firing of PV interneurons in SS cortex were unaffected with short-term hAPP
449 expression, we did note a change in AP threshold, potentially attributable to alterations in Na_v
450 channels. It is likely that if expressed longer, hAPP expression in the SS Ctx may result in impaired
451 PV interneuron excitability[7,13]. Thus, alternative biophysical mechanisms are likely responsible
452 for our observations following short-term hAPP expression in adult mice. Notably, we observed a
453 substantial decrease in input resistance in LEC PV cells expressing hAPP. This could be due to
454 enhanced availability of leak channels or potentially low-voltage activating K^+ conductances, such
455 as KCNQ (K_v7), which have been shown to be regulated by APP cleaving proteins[63] and cleavage
456 products[66,6869]. Interestingly, the Gq-coupled hM3Dq DREADD system increases cell excitability
457 specifically by increasing input resistance in cells. Of note, here we show that recovery of reduced
458 input resistance in PV interneurons through specific activation of Gq.DREADDs was sufficient to
459 attenuate hAPP-induced hyperexcitability in the LEC *in vivo*.
460
461 The LEC is also the first cortical region to develop tau pathology[1,34-37]. Yet, the relationship
462 between hAPP, hyperexcitability, and Tau remains unclear. It has previously been established that
463 artificially increasing neuronal activity can accelerate tau pathology[38-40]. However, the expression
464 of hTau has been suggested to strongly dampen circuit excitability[16,41,42] (but see[43]). Here we
465 observed that hTau co-expressed with hAPP results in an intermediate circuit excitability level
466 when compared to hAPP or hTau injected alone. Synaptic spread of tau has been shown from the
467 entorhinal cortex to other brain regions[70,71], and most recently this effect has been suggested to
468 occur in human brain via the oligomeric tau species (T22+)[44]. Remarkably, although hTau co-
469 injection with hAPP somewhat normalized circuit excitability, it also resulted in a significant
470 increase and apparent extracellular translocation of phospho-tau and oligomeric tau species.
471
472 The LEC is the first cortical region to undergo end-stage cellular neurodegeneration[1] in AD,
473 specifically, Layer II[2] excitatory cells[4]. Conversely, one of the earliest pathophysiological

474 alterations seen in both humans with AD, and in mouse models of early- and late-onset AD
475 pathology[9,15,16] is altered local circuit excitability[3,72,73]. In agreement with our mechanistic cellular
476 and *in vivo* findings here, hyperactivity has been shown to preferentially emerge in the LEC
477 region[3]. As with others, our slice electrophysiology assessments of circuit excitability aligned with
478 our *in vivo* findings as good predictors of hyperexcitability in AD pathology studies[7,14,74]. Our
479 study suggests that hAPP-induced hyperexcitability in the LEC arises not from alterations in the
480 intrinsic or synaptic properties of AD-vulnerable LII excitatory cells, but rather from an initial
481 alteration in intrinsic excitability of surrounding interneurons. The fact that short-term hAPP
482 expression in SS cortex caused no changes in PV firing or overall basal circuit excitability supports
483 this notion. Circuit hyperexcitability is likely an influential factor in the early neurodegenerative
484 cascade[7575], as it has been shown to exacerbate release of amyloid-beta[76], and also promotes tau
485 pathology and subsequent trans-synaptic tau spread[39] which ultimately tracks with spine synapse
486 degeneration[14] and cell death[77]. Ultimately, regions that first undergo hyperexcitability may also
487 be among the earliest to display these pathological markers as the disease progresses[39,75]. Thus,
488 PV interneurons of the LEC potentially represent a prime target for therapeutic intervention in the
489 early stages of Alzheimer's Disease.
490

1 Vossel, K. A. *et al.* Incidence and impact of subclinical epileptiform activity in Alzheimer's disease. *Ann Neurol* **80**, 858-870, doi:10.1002/ana.24794 (2016).
2 Gomez-Isla, T. *et al.* Profound loss of layer II entorhinal cortex neurons occurs in very mild Alzheimer's disease. *J Neurosci* **16**, 4491-4500, doi:10.1523/JNEUROSCI.16-14-04491.1996 (1996).
3 Nuriel, T. *et al.* Neuronal hyperactivity due to loss of inhibitory tone in APOE4 mice lacking Alzheimer's disease-like pathology. *Nat Commun* **8**, 1464, doi:10.1038/s41467-017-01444-0 (2017).
4 Angulo, S. L. *et al.* Tau and amyloid-related pathologies in the entorhinal cortex have divergent effects in the hippocampal circuit. *Neurobiol Dis* **108**, 261-276, doi:10.1016/j.nbd.2017.08.015 (2017).
5 Braak, H. & Braak, E. Neuropathological stageing of Alzheimer-related changes. *Acta Neuropathol* **82**, 239-259, doi:10.1007/BF00308809 (1991).
6 Khan, U. A. *et al.* Molecular drivers and cortical spread of lateral entorhinal cortex dysfunction in preclinical Alzheimer's disease. *Nat Neurosci* **17**, 304-311, doi:10.1038/nn.3606 (2014).
7 Kobro-Flatmoen, A., Nagelhus, A. & Witter, M. P. Reelin-immunoreactive neurons in entorhinal cortex layer II selectively express intracellular amyloid in early Alzheimer's disease. *Neurobiol Dis* **93**, 172-183, doi:10.1016/j.nbd.2016.05.012 (2016).
8 Palop, J. J. *et al.* Aberrant excitatory neuronal activity and compensatory remodeling of inhibitory hippocampal circuits in mouse models of Alzheimer's disease. *Neuron* **55**, 697-711, doi:10.1016/j.neuron.2007.07.025 (2007).
9 Verret, L. *et al.* Inhibitory interneuron deficit links altered network activity and cognitive dysfunction in Alzheimer model. *Cell* **149**, 708-721, doi:10.1016/j.cell.2012.02.046 (2012).
10 Mondragon-Rodriguez, S., Gu, N., Manseau, F. & Williams, S. Alzheimer's Transgenic Model Is Characterized by Very Early Brain Network Alterations and beta-CTF Fragment Accumulation: Reversal by beta-Secretase Inhibition. *Front Cell Neurosci* **12**, 121, doi:10.3389/fncel.2018.00121 (2018).
11 Petrache, A. L. *et al.* Aberrant Excitatory-Inhibitory Synaptic Mechanisms in Entorhinal Cortex Microcircuits During the Pathogenesis of Alzheimer's Disease. *Cereb Cortex* **29**, 1834-1850, doi:10.1093/cercor/bhz016 (2019).
12 Hijazi, S. *et al.* Early restoration of parvalbumin interneuron activity prevents memory loss and network hyperexcitability in a mouse model of Alzheimer's disease. *Mol Psychiatry* **25**, 3380-3398, doi:10.1038/s41380-019-0483-4 (2020).
13 Johnson, E. C. B. *et al.* Behavioral and neural network abnormalities in human APP transgenic mice resemble those of App knock-in mice and are modulated by familial Alzheimer's disease mutations but not by inhibition of BACE1. *Mol Neurodegener* **15**, 53, doi:10.1186/s13024-020-00393-5 (2020).
14 Zhang, Z. *et al.* Hyper-excitability of corticothalamic PT neurons in mPFC promotes irritability in the mouse model of Alzheimer's disease. *Cell Rep* **41**, 111577, doi:10.1016/j.celrep.2022.111577 (2022).
15 Olah, V. J. *et al.* Biophysical K(v)3 channel alterations dampen excitability of cortical PV interneurons and contribute to network hyperexcitability in early Alzheimer's. *Elife* **11**, doi:10.7554/eLife.75316 (2022).
16 Siskova, Z. *et al.* Dendritic structural degeneration is functionally linked to cellular hyperexcitability in a mouse model of Alzheimer's disease. *Neuron* **84**, 1023-1033, doi:10.1016/j.neuron.2014.10.024 (2014).
17 Nilssen, E. S. *et al.* Inhibitory Connectivity Dominates the Fan Cell Network in Layer II of Lateral Entorhinal Cortex. *J Neurosci* **38**, 9712-9727, doi:10.1523/JNEUROSCI.1290-18.2018 (2018).

18 Vormstein-Schneider, D. *et al.* Viral manipulation of functionally distinct interneurons in mice, non-human primates and humans. *Nat Neurosci* **23**, 1629-1636, doi:10.1038/s41593-020-0692-9 (2020).
19 Titlow, J. S. *et al.* Systematic analysis of YFP traps reveals common mRNA/protein discordance in neural tissues. *J Cell Biol* **222**, doi:10.1083/jcb.202205129 (2023).
20 Rayaprolu, S. *et al.* Cell type-specific biotin labeling in vivo resolves regional neuronal and astrocyte proteomic differences in mouse brain. *Nat Commun* **13**, 2927, doi:10.1038/s41467-022-30623-x (2022).
21 Kumar, P. *et al.* Native-state proteomics of Parvalbumin interneurons identifies unique molecular signatures and vulnerabilities to early Alzheimer's pathology. *Nat Commun* **15**, 2823, doi:10.1038/s41467-024-47028-7 (2024).
22 Yu, L. *et al.* Cortical Proteins Associated With Cognitive Resilience in Community-Dwelling Older Persons. *JAMA Psychiatry* **77**, 1172-1180, doi:10.1001/jamapsychiatry.2020.1807 (2020).
23 Chen, C. *et al.* Early impairment of cortical circuit plasticity and connectivity in the 5XFAD Alzheimer's disease mouse model. *Transl Psychiatry* **12**, 371, doi:10.1038/s41398-022-02132-4 (2022).
24 Koo, E. H. *et al.* Differential expression of amyloid precursor protein mRNAs in cases of Alzheimer's disease and in aged nonhuman primates. *Neuron* **4**, 97-104, doi:10.1016/0896-6273(90)90446-m (1990).
25 Matsui, T. *et al.* Expression of APP pathway mRNAs and proteins in Alzheimer's disease. *Brain Res* **1161**, 116-123, doi:10.1016/j.brainres.2007.05.050 (2007).
26 Lehmann, L., Lo, A., Knox, K. M. & Barker-Haliski, M. Alzheimer's Disease and Epilepsy: A Perspective on the Opportunities for Overlapping Therapeutic Innovation. *Neurochem Res* **46**, 1895-1912, doi:10.1007/s11064-021-03332-y (2021).
27 Chen, L. *et al.* Progressive excitability changes in the medial entorhinal cortex in the 3xTg mouse model of Alzheimer's disease pathology. *bioRxiv*, doi:10.1101/2023.05.30.542838 (2023).
28 Tahvildari, B. & Alonso, A. Morphological and electrophysiological properties of lateral entorhinal cortex layers II and III principal neurons. *J Comp Neurol* **491**, 123-140, doi:10.1002/cne.20706 (2005).
29 Braak, H., Braak, E., Bohl, J. & Bratzke, H. Evolution of Alzheimer's disease related cortical lesions. *J Neural Transm Suppl* **54**, 97-106, doi:10.1007/978-3-7091-7508-8_9 (1998).
30 Desikan, R. S. *et al.* Amyloid-beta--associated clinical decline occurs only in the presence of elevated P-tau. *Arch Neurol* **69**, 709-713, doi:10.1001/archneurol.2011.3354 (2012).
31 Lue, L. F. *et al.* Soluble amyloid beta peptide concentration as a predictor of synaptic change in Alzheimer's disease. *Am J Pathol* **155**, 853-862, doi:10.1016/s0002-9440(10)65184-x (1999).
32 Naslund, J. *et al.* Correlation between elevated levels of amyloid beta-peptide in the brain and cognitive decline. *JAMA* **283**, 1571-1577, doi:10.1001/jama.283.12.1571 (2000).
33 Schultz, M. K., Jr. *et al.* Pharmacogenetic neuronal stimulation increases human tau pathology and trans-synaptic spread of tau to distal brain regions in mice. *Neurobiol Dis* **118**, 161-176, doi:10.1016/j.nbd.2018.07.003 (2018).
34 Wu, J. W. *et al.* Neuronal activity enhances tau propagation and tau pathology in vivo. *Nat Neurosci* **19**, 1085-1092, doi:10.1038/nn.4328 (2016).
35 Yamada, K. *et al.* Neuronal activity regulates extracellular tau in vivo. *J Exp Med* **211**, 387-393, doi:10.1084/jem.20131685 (2014).
36 Busche, M. A. *et al.* Tau impairs neural circuits, dominating amyloid-beta effects, in Alzheimer models in vivo. *Nat Neurosci* **22**, 57-64, doi:10.1038/s41593-018-0289-8 (2019).
37 Minkeviciene, R. *et al.* Amyloid beta-induced neuronal hyperexcitability triggers progressive epilepsy. *J Neurosci* **29**, 3453-3462, doi:10.1523/JNEUROSCI.5215-08.2009 (2009).

38 Hall, A. M. *et al.* Tau-dependent Kv4.2 depletion and dendritic hyperexcitability in a mouse model of Alzheimer's disease. *J Neurosci* **35**, 6221-6230, doi:10.1523/JNEUROSCI.2552-14.2015 (2015).
39 Colom-Cadena, M. *et al.* Synaptic oligomeric tau in Alzheimer's disease - A potential culprit in the spread of tau pathology through the brain. *Neuron* **111**, 2170-2183 e2176, doi:10.1016/j.neuron.2023.04.020 (2023).
40 Huang, Y. A., Zhou, B., Wernig, M. & Sudhof, T. C. ApoE2, ApoE3, and ApoE4 Differentially Stimulate APP Transcription and Abeta Secretion. *Cell* **168**, 427-441 e421, doi:10.1016/j.cell.2016.12.044 (2017).
41 Lee, S. I. *et al.* APOE4-carrying human astrocytes oversupply cholesterol to promote neuronal lipid raft expansion and Abeta generation. *Stem Cell Reports* **16**, 2128-2137, doi:10.1016/j.stemcr.2021.07.017 (2021).
42 Thakur, M. K. & Mani, S. T. Estradiol regulates APP mRNA alternative splicing in the mice brain cortex. *Neurosci Lett* **381**, 154-157, doi:10.1016/j.neulet.2005.02.014 (2005).
43 Bjelik, A. *et al.* Human apoB overexpression and a high-cholesterol diet differently modify the brain APP metabolism in the transgenic mouse model of atherosclerosis. *Neurochem Int* **49**, 393-400, doi:10.1016/j.neuint.2006.01.026 (2006).
44 Bjelik, A. *et al.* APP mRNA splicing is upregulated in the brain of biglycan transgenic mice. *Neurochem Int* **50**, 1-4, doi:10.1016/j.neuint.2006.07.009 (2007).
45 Dubal, D. B., Broestl, L. & Worden, K. Sex and gonadal hormones in mouse models of Alzheimer's disease: what is relevant to the human condition? *Biol Sex Differ* **3**, 24, doi:10.1186/2042-6410-3-24 (2012).
46 Notkola, I. L. *et al.* Serum total cholesterol, apolipoprotein E epsilon 4 allele, and Alzheimer's disease. *Neuroepidemiology* **17**, 14-20, doi:10.1159/000026149 (1998).
47 Kivipelto, M. *et al.* Apolipoprotein E epsilon4 allele, elevated midlife total cholesterol level, and high midlife systolic blood pressure are independent risk factors for late-life Alzheimer disease. *Ann Intern Med* **137**, 149-155, doi:10.7326/0003-4819-137-3-200208060-00006 (2002).
48 Honig, L. S., Kukull, W. & Mayeux, R. Atherosclerosis and AD: analysis of data from the US National Alzheimer's Coordinating Center. *Neurology* **64**, 494-500, doi:10.1212/01.WNL.0000150886.50187.30 (2005).
49 Saito, T. *et al.* Single App knock-in mouse models of Alzheimer's disease. *Nat Neurosci* **17**, 661-663, doi:10.1038/nn.3697 (2014).
50 Baglietto-Vargas, D. *et al.* Generation of a humanized Abeta expressing mouse demonstrating aspects of Alzheimer's disease-like pathology. *Nat Commun* **12**, 2421, doi:10.1038/s41467-021-22624-z (2021).
51 Mehr, A. *et al.* Lack of APP and APLP2 in GABAergic Forebrain Neurons Impairs Synaptic Plasticity and Cognition. *Cereb Cortex* **30**, 4044-4063, doi:10.1093/cercor/bhaa025 (2020).
52 Yamamoto, K., Yamamoto, R. & Kato, N. Amyloid beta and Amyloid Precursor Protein Synergistically Suppress Large-Conductance Calcium-Activated Potassium Channel in Cortical Neurons. *Front Aging Neurosci* **13**, 660319, doi:10.3389/fnagi.2021.660319 (2021).
53 Agsten, M. *et al.* BACE1 modulates gating of KCNQ1 (Kv7.1) and cardiac delayed rectifier KCNQ1/KCNE1 (IKs). *J Mol Cell Cardiol* **89**, 335-348, doi:10.1016/j.yjmcc.2015.10.006 (2015).
54 Lehnert, S. *et al.* Ion channel regulation by beta-secretase BACE1 - enzymatic and non-enzymatic effects beyond Alzheimer's disease. *Channels (Austin)* **10**, 365-378, doi:10.1080/19336950.2016.1196307 (2016).
55 Wong, H. K. *et al.* beta Subunits of voltage-gated sodium channels are novel substrates of beta-site amyloid precursor protein-cleaving enzyme (BACE1) and gamma-secretase. *J Biol Chem* **280**, 23009-23017, doi:10.1074/jbc.M414648200 (2005).

633 56 Manville, R. W. & Abbott, G. W. The Amyloid Precursor Protein C99 Fragment Modulates Voltage-
634 Gated Potassium Channels. *Cell Physiol Biochem* **55**, 157-170, doi:10.33594/000000397 (2021).
635 57 Furukawa, K., Barger, S. W., Blalock, E. M. & Mattson, M. P. Activation of K+ channels and
636 suppression of neuronal activity by secreted beta-amyloid-precursor protein. *Nature* **379**, 74-78,
637 doi:10.1038/379074a0 (1996).
638 58 Mayordomo-Cava, J., Yajeya, J., Navarro-Lopez, J. D. & Jimenez-Diaz, L. Amyloid-beta(25-35)
639 Modulates the Expression of GirK and KCNQ Channel Genes in the Hippocampus. *PLoS One* **10**,
640 e0134385, doi:10.1371/journal.pone.0134385 (2015).
641 59 Harris, J. A. *et al.* Human P301L-mutant tau expression in mouse entorhinal-hippocampal network
642 causes tau aggregation and presynaptic pathology but no cognitive deficits. *PLoS One* **7**, e45881,
643 doi:10.1371/journal.pone.0045881 (2012).
644 60 Pickett, E. K. *et al.* Spread of tau down neural circuits precedes synapse and neuronal loss in the
645 rTgTauEC mouse model of early Alzheimer's disease. *Synapse* **71**, doi:10.1002/syn.21965 (2017).
646 61 Cope, Z. A., Murai, T. & Sukoff Rizzo, S. J. Emerging Electroencephalographic Biomarkers to
647 Improve Preclinical to Clinical Translation in Alzheimer's Disease. *Front Aging Neurosci* **14**,
648 805063, doi:10.3389/fnagi.2022.805063 (2022).
649 62 Kelberman, M. A. *et al.* Age-dependent dysregulation of locus coeruleus firing in a transgenic rat
650 model of Alzheimer's disease. *Neurobiol Aging* **125**, 98-108,
651 doi:10.1016/j.neurobiolaging.2023.01.016 (2023).
652 63 Bero, A. W. *et al.* Neuronal activity regulates the regional vulnerability to amyloid-beta deposition.
653 *Nat Neurosci* **14**, 750-756, doi:10.1038/nn.2801 (2011).
654 64 Olney, J. W. Brain lesions, obesity, and other disturbances in mice treated with monosodium
655 glutamate. *Science* **164**, 719-721, doi:10.1126/science.164.3880.719 (1969).
656 65 Rodriguez, G. A., Barrett, G. M., Duff, K. E. & Hussaini, S. A. Chemogenetic attenuation of neuronal
657 activity in the entorhinal cortex reduces Abeta and tau pathology in the hippocampus. *PLoS Biol*
658 **18**, e3000851, doi:10.1371/journal.pbio.3000851 (2020).
659 66 Taylor, A. L. What we talk about when we talk about capacitance measured with the voltage-
660 clamp step method. *J Comput Neurosci* **32**, 167-175, doi:10.1007/s10827-011-0346-8 (2012).
661 67 Chan, K. Y. *et al.* Engineered AAVs for efficient noninvasive gene delivery to the central and
662 peripheral nervous systems. *Nat Neurosci* **20**, 1172-1179, doi:10.1038/nn.4593 (2017).
663 68 Johnson, E. C. B. *et al.* Large-scale deep multi-layer analysis of Alzheimer's disease brain reveals
664 strong proteomic disease-related changes not observed at the RNA level. *Nat Neurosci* **25**, 213-
665 225, doi:10.1038/s41593-021-00999-y (2022).
666 69 Rangaraju, S. *et al.* Quantitative proteomics of acutely-isolated mouse microglia identifies novel
667 immune Alzheimer's disease-related proteins. *Mol Neurodegener* **13**, 34, doi:10.1186/s13024-
668 018-0266-4 (2018).
669 70 Rayaprolu, S. *et al.* Flow-cytometric microglial sorting coupled with quantitative proteomics
670 identifies moesin as a highly-abundant microglial protein with relevance to Alzheimer's disease.
671 *Mol Neurodegener* **15**, 28, doi:10.1186/s13024-020-00377-5 (2020).
672 71 Perez-Riverol, Y. *et al.* The PRIDE database resources in 2022: a hub for mass spectrometry-based
673 proteomics evidences. *Nucleic Acids Res* **50**, D543-D552, doi:10.1093/nar/gkab1038 (2022).
674 72 Galea, E. *et al.* Multi-transcriptomic analysis points to early organelle dysfunction in human
675 astrocytes in Alzheimer's disease. *Neurobiol Dis* **166**, 105655, doi:10.1016/j.nbd.2022.105655
676 (2022).
677 73 Hanzelmann, S., Castelo, R. & Guinney, J. GSVA: gene set variation analysis for microarray and
678 RNA-seq data. *BMC Bioinformatics* **14**, 7, doi:10.1186/1471-2105-14-7 (2013).

679

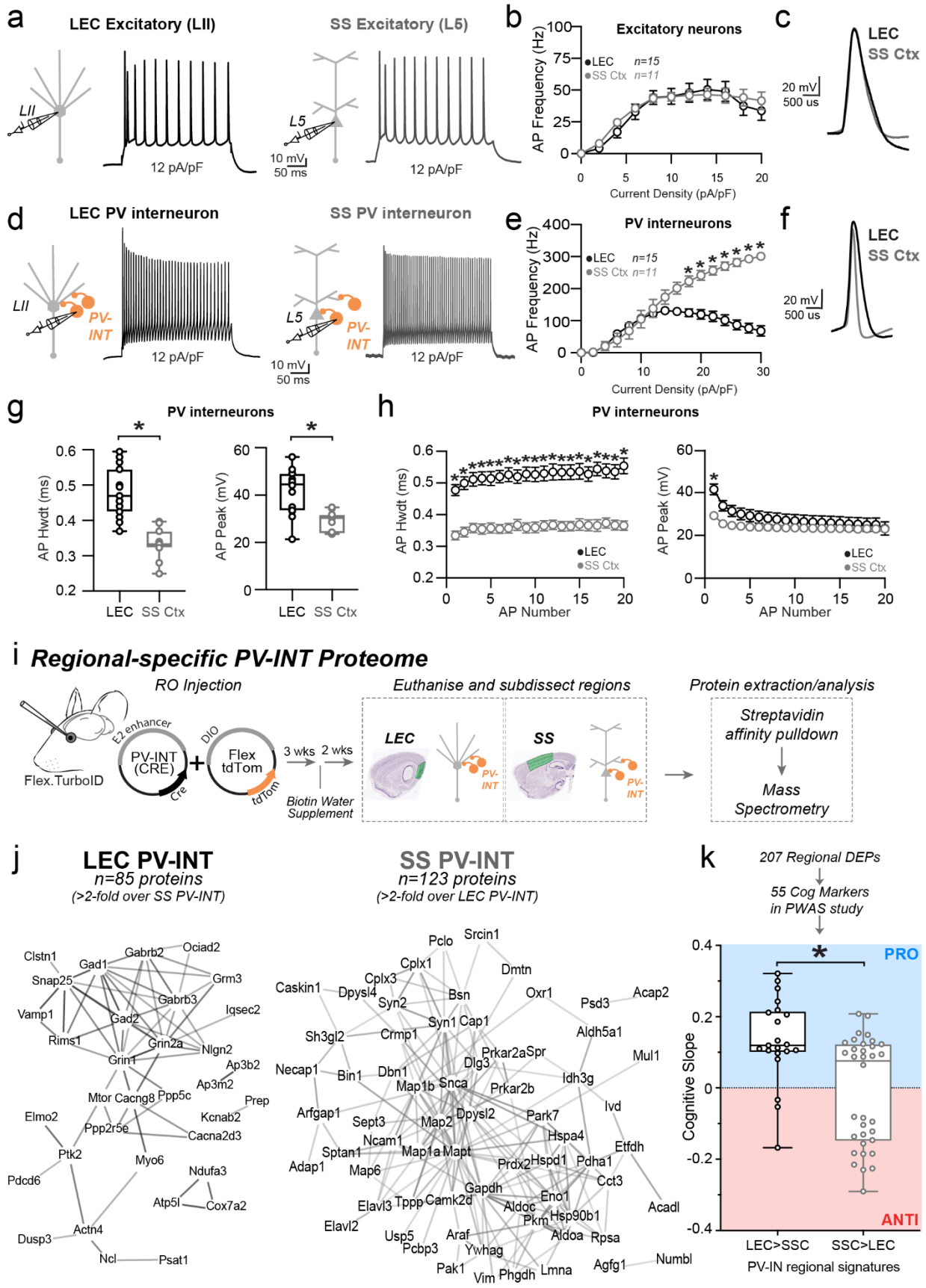
a
LEC Excitatory (LII)
SS Excitatory (L5)
LII
L5
12 pA/pF
10 mV
50 ms
b
Excitatory neurons
AP Frequency (Hz)
LEC n=15
SS Ctx n=11
Current Density (pA/pF)
c
LEC
SS Ctx
20 mV
500 us
d
LEC PV interneuron
SS PV interneuron
PV-INT
e
PV interneurons
f
g
PV interneurons
AP Hwdt (ms)
AP Peak (mV)
LEC
SS Ctx
h
AP Number
i
Regional-specific PV-INT Proteome
RO Injection
Euthanise and subdissect regions
Protein extraction/analysis
Flex.TurboID
E2 enhancer
PV-INT (CRE)
Cre
DIO
Flex tdTom
tdTom
3 wks
2 wks
Biotin Water Supplement
Streptavidin affinity pulldown
Mass Spectrometry
j
LEC PV-INT
n=85 proteins
(>2-fold over SS PV-INT)
SS PV-INT
n=123 proteins
(>2-fold over LEC PV-INT)
k
207 Regional DEPs
55 Cog Markers in PWAS study
PRO
ANTI
Cognitive Slope
LEC>SSC
SSC>LEC
PV-IN regional signatures

681 **Figure 1. PV-INTs in an AD vulnerable region display reduced baseline firing**

682 **a,d.** Graphical summary of AAV.E2.tdTom stereotactic injection in either the Lateral Entorhinal
683 Cortex or Somatosensory cortex. PV-interneurons were fluorescently targeted for whole-cell
684 current clamp recordings (d) as well as nearby excitatory cells (a). AP firing elicited by square
685 pulse current injections of varying magnitude normalized to cellular capacitance during recording
686 in excitatory cells (a) and PV-interneurons (d) mice from L2 LEC (left) and L5 SS Ctx (Right) at
687 12 pA/pF.

688 **b.** Group data summary of AP firing frequency in WT mice. Excitatory cells between LEC and SS
689 Ctx showed no difference in AP Frequency (Hz) Ctx (LEC: Max: 50.42±5.63 Hz, SS Ctx: Max:
690 46.35±5.51 Hz, p=0.46).

691 **c.** AP waveforms of excitatory cells were compared at 12 pA/pF square pulse injections in WT
692 mice from L2 LEC and L5 SS Ctx. Aps from the 1st spike in the train are superimposed for
693 comparison.

694 **e.** Group data summary of AP firing frequency in WT mice. PV interneurons in L2 LEC show a
695 strong reduction in AP max firing frequency at higher current densities when compared to PV
696 interneurons of L5 SS Ctx (LEC: Max: 131.6±11.48 Hz, SS Ctx: Max: 301.1±27.59 Hz, p=<0.0001
697 for 16 pA/pF and above).

698 **f.** AP waveforms of tdTom+ PV interneurons were compared at 12 pA/pF square pulse injections
699 in WT mice from L2 LEC and L5 SS Ctx. Aps from the 1st spike in the train are superimposed for
700 comparison.

701 **g.** Summary data of AP properties. L2 LEC PV interneurons display a significantly increased AP
702 peak (LEC: 41.86±2.66 pA, SS: 28.75±1.30 pA, p=0.0002, t= 4.83, df=24, two-tailed unpaired t-
703 test) and AP Hwdt (LEC: 0.48 ± 0.02 ms, SS: 0.33 ± 0.01 ms, p=<0.0001, t=6.10, df=25) for the
704 first AP of the spike train. Individual data points and box plots are displayed. Significance is
705 defined as p<0.05, unpaired t-tests.

706 **h.** Relationship between AP peak or width, in WT mice and AP # during spike trains elicited with
707 a 12 pA/pF current injection.

708 **i.** Experimental approach for Regional-specific PV-interneuron Proteomes: E2 enhancer Cre AAV
709 was retro-orbitally delivered to WT (Control) or Rosa26TurboID/wt (PV-CIBOP) mice (n=3 per
710 genotype, including males and females) followed by 3 weeks of Cre-mediated recombination, and

711 2 additional weeks of biotin supplementation (drinking water). The brain was then microdissected
712 into LEC and SS Ctx and prepared for biochemical studies.
713 **j.** STRING analysis of PV-enriched proteins for LEC PV-INTs (left) and SS Ctx PV-INTs (right)
714 (>2-fold enriched over other region) shows synaptic receptors, synaptic vesicle and exocytosis
715 related proteins including GAD1/2, GABAb2/3, and complexins.
716 **k.** Enrichment of PWAS-identified proteins associated with cognitive slope in LEC (left) or SS
717 Ctx (right) PV-enriched proteomic signatures. Cognitive slope was estimated in ROSMAP cases.
718 Positive slope indicates cognitive stability or resilience when proteins are present while a negative
719 slope indicates cognitive decline when proteins are present. Proteins positively correlated with
720 cognitive slope are referred to as pro-resilience proteins while those negative correlated with
721 cognitive slope are anti-resilience proteins. Enrichment of previously identified 'pro' and 'anti'
722 resilience proteins within the PV protein dataset identified by CIBOP were assessed after
723 weighting based on strength of association between proteins and cognitive slope. (LEC: 0.13± 0.03
724 and SS Ctx: -0.01±0.03; p=0.001, t=3.71, df=53, two-tailed Mann Whitney test).
725 For b, e, and h: For all summary graphs, data are expressed as mean (± SEM). Statistical
726 significance is denoted as *=p<0.05, as determined by Two-way ANOVA with Sidak's multiple
727 comparison test. For all summary graphs, data are expressed as mean (± SEM).
728
729 Also see Extended Data Figure 1 for related analyses and datasets.

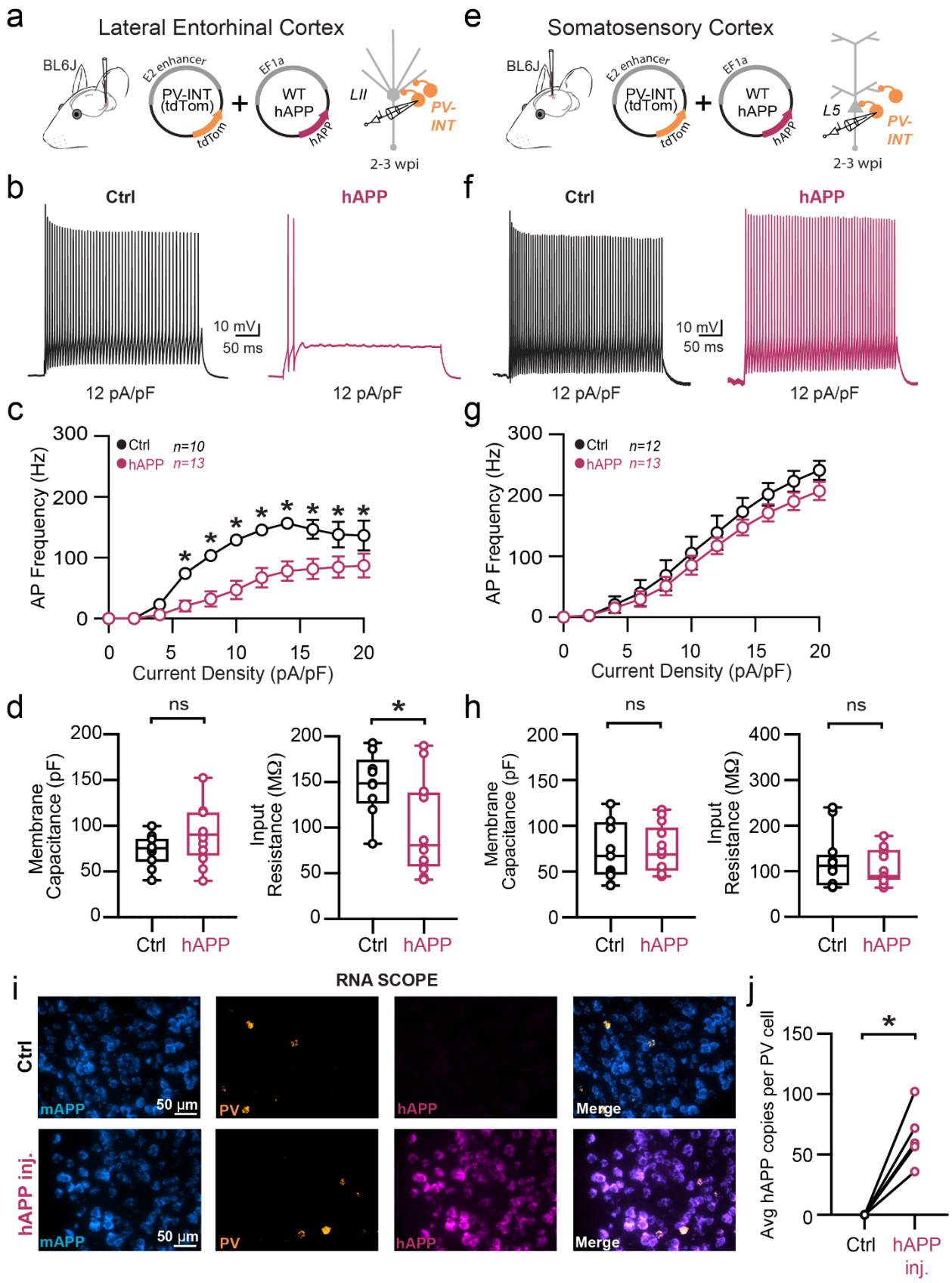
a
Lateral Entorhinal Cortex
BL6J
E2 enhancer
PV-INT (tdTom)
tdTom
EF1a
WT hAPP
hAPP
LII
PV-INT
2-3 wpi
e
Somatosensory Cortex
L5
b
Ctrl
hAPP
10 mV
50 ms
12 pA/pF
f
c
Ctrl n=10
hAPP n=13
AP Frequency (Hz)
Current Density (pA/pF)
g
Ctrl n=12
hAPP n=13
d
ns
*
Membrane Capacitance (pF)
Input Resistance (MΩ)
h
i
RNA SCOPE
Ctrl
hAPP inj.
mAPP
50 µm
PV
hAPP
Merge
j
Avg hAPP copies per PV cell
hAPP inj.

730

Figure 2. Adult-onset human APP expression reduces LEC PV interneuron excitability

a. Graphical summary of AAV.E2.tdTom and AAV.EF1a.hAPP (or for Ctrl, saline) stereotactic injection in the Lateral Entorhinal Cortex. PV-interneurons were fluorescently targeted (tdTom+) for whole-cell current clamp recordings.

b. AP firing elicited by square pulse current injections of varying magnitude normalized to cellular capacitance during recording in tdTom+ PV-INT from L2 LEC at 12 pA/pF.

c. Group data summary of AP firing frequency in L2 LEC from Ctrl (black) and hAPP injected mice (magenta). LEC PV interneurons from hAPP injected mice show a significant reduction in AP Frequency (Hz) when compared to Ctrl(Ctrl: Max: 156.6 ±13.52 Hz, hAPP: Max: 91.84± 8.74 Hz).

d. Summary data of AP properties. L2 LEC PV interneurons after hAPP injection display a significantly decreased input resistance (Ctrl: 145.7 ± 11.61 MΩ, hAPP: 88.78 ± 15.11 MΩ, $p=0.01$, $t=2.73$, $df=21$) and an insignificant increase in membrane capacitance (Ctrl: 68.83 ± 5.34 pF, hAPP: 90.21 ± 9.77 pF, $p=0.07$, $t=1.92$, $df=21$).

e. Graphical summary of AAV.E2.tdTom and AAV.EF1a.hAPP (or for Ctrl, saline) stereotactic injection in the Somatosensory Cortex. PV-interneurons were fluorescently targeted (tdTom+) for whole-cell current clamp recordings.

f. AP firing elicited by square pulse current injections of varying magnitude normalized to cellular capacitance during recording in tdTom+ PV-INT from L5 SS Ctx at 12 pA/pF.

g. Group data summary of AP firing frequency in L5 SS Ctx from Ctrl (black) and hAPP injected mice (magenta). SS Ctx PV interneurons from hAPP injected mice show no significant change in AP Frequency (Hz) when compared to Ctrl (Ctrl: Max: 301.1 ±27.59 Hz, hAPP: Max: 257.2± 24.06 Hz).

h. Summary data of AP properties. SS Ctx interneurons after hAPP injection display an unchanged Membrane Capacitance (Ctrl: 71.91 ± 9.514, hAPP: 73.14 ± 7.327, $p=0.9180$, $t=0.1041$, $df=23$) and input resistance (Ctrl: 121.2 ± 17.14, hAPP: 109.1 ± 10.56, $p=0.5475$, $t=0.6106$, $df=23$).

i. RNAscope representative images at 40x magnification for Ctrl injected (top) and hAPP injected mice (bottom): mAPP mRNA (cyan), Parvalbumin mRNA (gold), human APP mRNA (magenta), and a final merged image.

760 **j.** RNAscope quantification for hAPP copies per PV+ cell comparing control to hAPP injected.
761 hAPP injected show a significant increase in hAPP copies per PV+ cell ($p=0.0039$, $t=5.987$, $df=4$;
762 two-tailed paired t-test).
763 For all summary graphs, data are expressed as mean (± SEM). For c, g, and i: Statistical
764 significance is denoted as *=$p<0.05$, as determined by Two-way ANOVA with Sidak's multiple
765 comparison test. For d, h: Individual data points and box plots are displayed. Statistical
766 significance is denoted as *=$p<0.05$, as determined by two-tailed unpaired t-test.
767
768
769

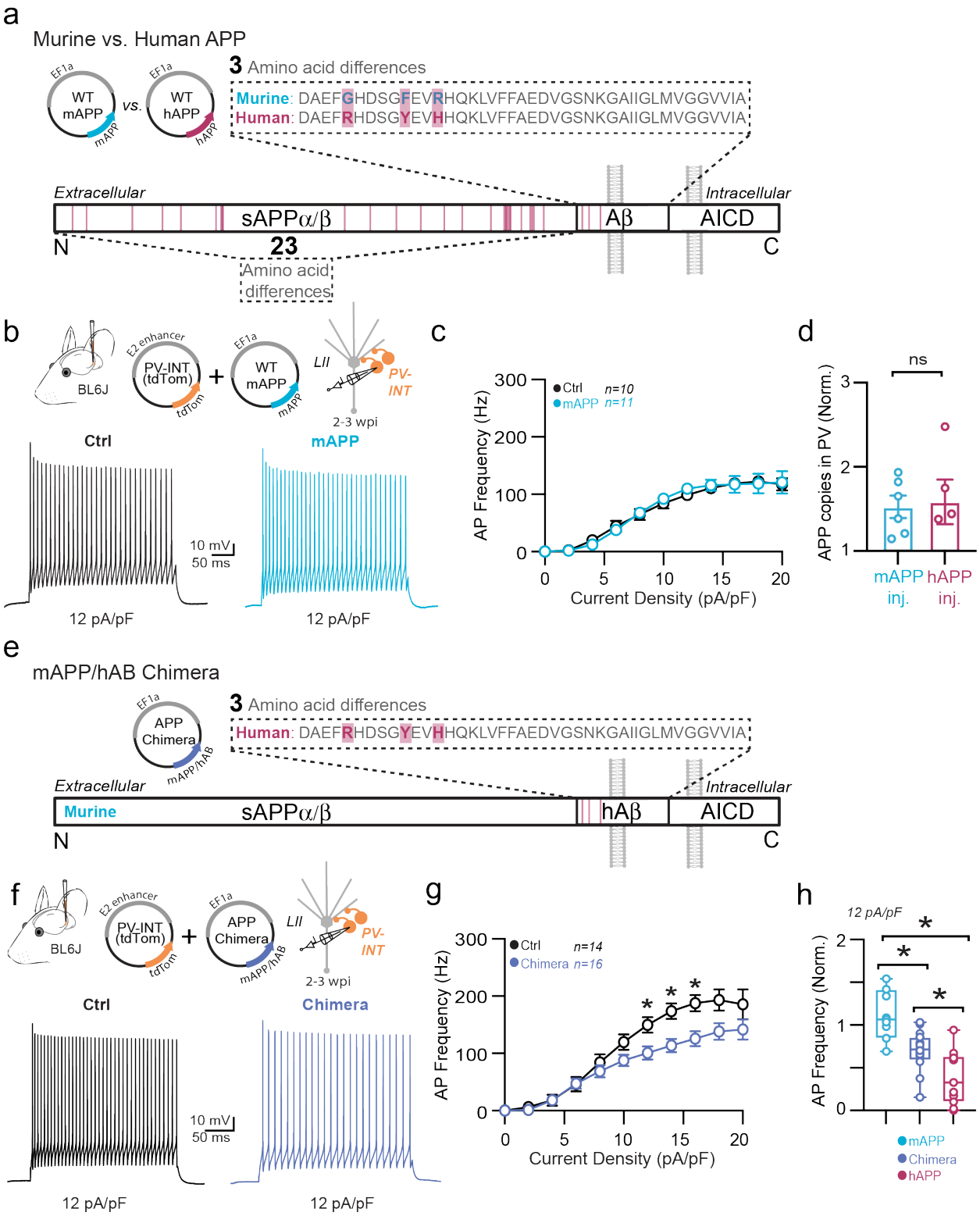

Figure 3. Murine APP does not affect PV interneuron physiology, but mAPP/hAB chimera replicates partial findings of hAPP-induced deficits

773 **a.** Pictorial representation of differing amino acids between murine APP and human APP proteins;
774 26 different amino acids in total, 3 of which are in the amyloid-beta segment of the protein.
775 **b.** Graphical summary of AAV.E2.tdTom and AAV.EF1a.mAPP (or for Ctrl, saline) stereotactic
776 injection in the Lateral Entorhinal Cortex. PV interneurons were fluorescently targeted for whole-
777 cell current clamp recordings**.** AP firing elicited by square pulse current injections of varying
778 magnitude normalized to cellular capacitance during recording in PV interneurons from Ctrl (left)
779 and mAPP injected (right) L2 LEC at 12 pA/pF.
780 **c.** Group data summary of AP firing frequency in Ctrl and mAPP injected mice. PV interneurons
781 between Ctrl and mAPP injected showed no difference in AP Frequency (Hz) (Ctrl: Max: 122.3
782 ±11.11 Hz, mAPP: Max: 120.6 ± 11.50 Hz, p=0.95). Statistical significance is denoted as
783 *=p<0.05, as determined by Two-way ANOVA with Sidak's multiple comparison test.
784 **d.** RNAscope quantification for APP copies per PV+ cell with APP injected (mAPP or hAPP) each
785 normalized to their contralateral hemisphere average endogenous murine APP copy per PV+ cell.
786 mAPP injected and hAPP injected mice show similar increases in increased APP expression.
787 copies per PV+ cell (p=0.84, t=0.21, df=9; two-tailed unpaired t-test).
788 **e.** Pictorial representation of the resultant Chimera protein; murine APP with a humanized
789 amyloid-beta segment.
790 **f.** Graphical summary of AAV.E2.tdTom and AAV.EF1a.mAPP/hAB Chimera (or for Ctrl, saline)
791 stereotactic injection in the Lateral Entorhinal Cortex. PV interneurons were fluorescently targeted
792 for whole-cell current clamp recordings**.** AP firing elicited by square pulse current injections of
793 varying magnitude normalized to cellular capacitance during recording in PV interneurons from
794 Ctrl (left) and Chimera injected (right) L2 LEC at 12 pA/pF.
795 **g.** Group data summary of AP firing frequency in Ctrl and Chimera injected mice. PV interneurons
796 between Ctrl and mAPP injected showed no difference in AP Frequency (Hz) (Ctrl: Max: 193.6
797 ±19.47 Hz, mAPP: Max: 145.4 ± 14.05 Hz, p<0.0001; for 12 pA p=0.0378, for 14 pA p=0.0368,
798 for 16 pA p=0.0426). Statistical significance is denoted as *=p<0.05, as determined by Two-way
799 ANOVA with Sidak's multiple comparison test.
800 **h.** Comparison of PV interneuron firing frequencies expressing mAPP, mAPP/hAB Chimera, or
801 hAPP normalized to their dataset controls at 12 pA/pF. Statistical significance is denoted as
802 *=p<0.05, as determined by Ordinary one-way ANOVA with Tukey's multiple comparisons test.
803 (mAPP vs. Chimera: p=0.0011, mAPP vs. hAPP: <0.0001, Chimera vs. hAPP: p=0.0335; df=35).

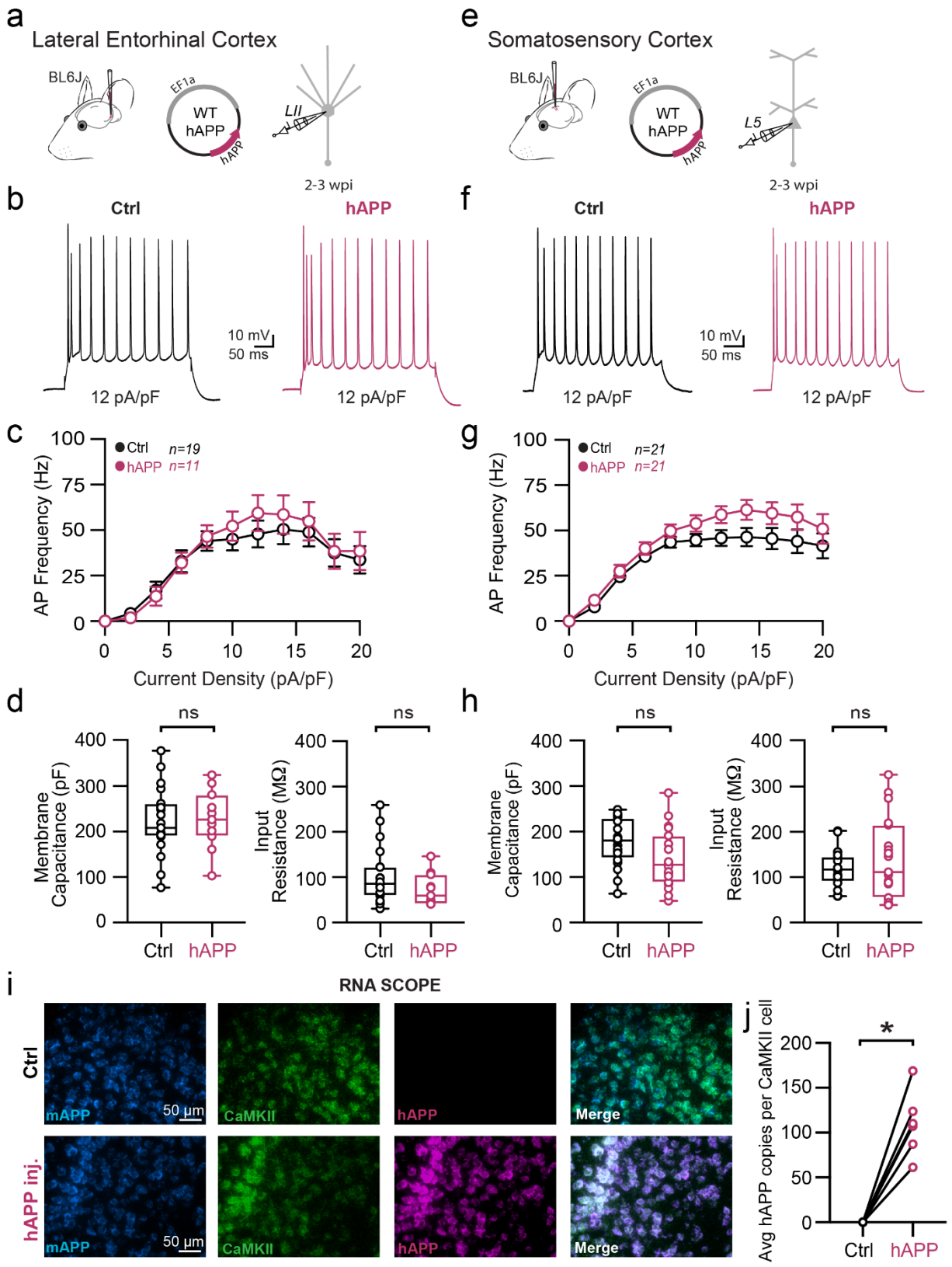
a
Lateral Entorhinal Cortex
BL6J
EF1a
WT
hAPP
hAPP
LII
2-3 wpi
b
Ctrl
hAPP
10 mV
50 ms
12 pA/pF
12 pA/pF
c
Ctrl n=19
hAPP n=11
AP Frequency (Hz)
Current Density (pA/pF)
d
ns
ns
Membrane Capacitance (pF)
Input Resistance (MΩ)
Ctrl
hAPP
e
Somatosensory Cortex
BL6J
EF1a
WT
hAPP
hAPP
L5
2-3 wpi
f
Ctrl
hAPP
10 mV
50 ms
12 pA/pF
12 pA/pF
g
Ctrl n=21
hAPP n=21
AP Frequency (Hz)
Current Density (pA/pF)
h
ns
ns
Membrane Capacitance (pF)
Input Resistance (MΩ)
Ctrl
hAPP
i
RNA SCOPE
Ctrl
hAPP inj.
mAPP
50 µm
CaMKII
hAPP
Merge
j
*
Avg hAPP copies per CaMKII cell
Ctrl
hAPP

806 **Figure 4. Adult-onset human APP expression does not alter excitatory neuron physiology**
807 **a.** Graphical summary of AAV.EF1a.hAPP (or for Ctrl, saline) stereotactic injection in the Lateral
808 Entorhinal Cortex. Excitatory cells were targeted for whole-cell current clamp recordings.
809 **b.** AP firing elicited by square pulse current injections of varying magnitude normalized to cellular
810 capacitance during recording in Ctrl and hAPP injected L2 LEC excitatory cells from at 12 pA/pF.
811 **c.** Group data summary of AP firing frequency in L2 LEC from Ctrl (black) and hAPP injected
812 mice (magenta). Excitatory neurons in L2 LEC from hAPP injected mice show no alteration in AP
813 Frequency (Hz) when compared to Ctrl (Ctrl: Max: 50.42 ± 5.63 Hz, hAPP: Max: 59.43 ± 6.56
814 Hz, p=0.99, df=28).
815 **d.** Summary data of AP properties. L2 LEC excitatory cells after hAPP injection display an
816 unchanged Membrane Capacitance (p=0.83, t=0.27) as well as an unchanged input resistance
817 (p=0.15, t=1.50, df=28).
818 **e.** Graphical summary of AAV.EF1a.hAPP (or for Ctrl, saline) stereotactic injection in the
819 Somatosensory Cortex. Excitatory neurons in L5 were targeted for whole-cell current clamp
820 recordings.
821 **f.** AP firing elicited by square pulse current injections of varying magnitude normalized to cellular
822 capacitance during recording in excitatory cells from L5 SS Ctx at 12 pA/pF.
823 **g.** Group data summary of AP firing frequency in L5 SS Ctx from Ctrl (black) and hAPP injected
824 mice (magenta). SS Ctx excitatory neurons from hAPP injected mice show no significant change
825 in AP Frequency (Hz) when compared to Ctrl (Ctrl: Max: 46.35 ± 5.38 Hz, hAPP: Max: 61.43 ±
826 6.78 Hz, p>0.05, df=40).
827 **h.** Summary data of AP properties. SS Ctx interneurons after hAPP injection display an unchanged
828 Membrane Capacitance and input resistance (Ctrl: 176.9 ± 11.58, hAPP: 140.5 ± 14.31, p=0.06,
829 t=1.98, df=40, two-tailed unpaired t-test).
830 **i.** RNAscope representative images at 40x magnification for Ctrl injected (top) and hAPP injected
831 mice (bottom(: mAPP mRNA (cyan), CaMKIIa mRNA (green), human APP mRNA (magenta),
832 and a final merged image.
833 **j.** RNAscope quantification for hAPP copies per CaMKIIa+ cell comparing control to hAPP
834 injected. hAPP injected show a significant increase in hAPP copies per CaMKIIa+ cell (p=0.0007,
835 t=7.42, df=5; two-tailed paired t-test).

For all summary graphs, data are expressed as mean (± SEM). For c, g: Statistical significance is denoted as *=p<0.05, as determined by Two-way ANOVA with Sidak's multiple comparison test. For d, h: Individual data points and box plots are displayed. Statistical significance is denoted as *=p<0.05, as determined by two-tailed unpaired t-test.

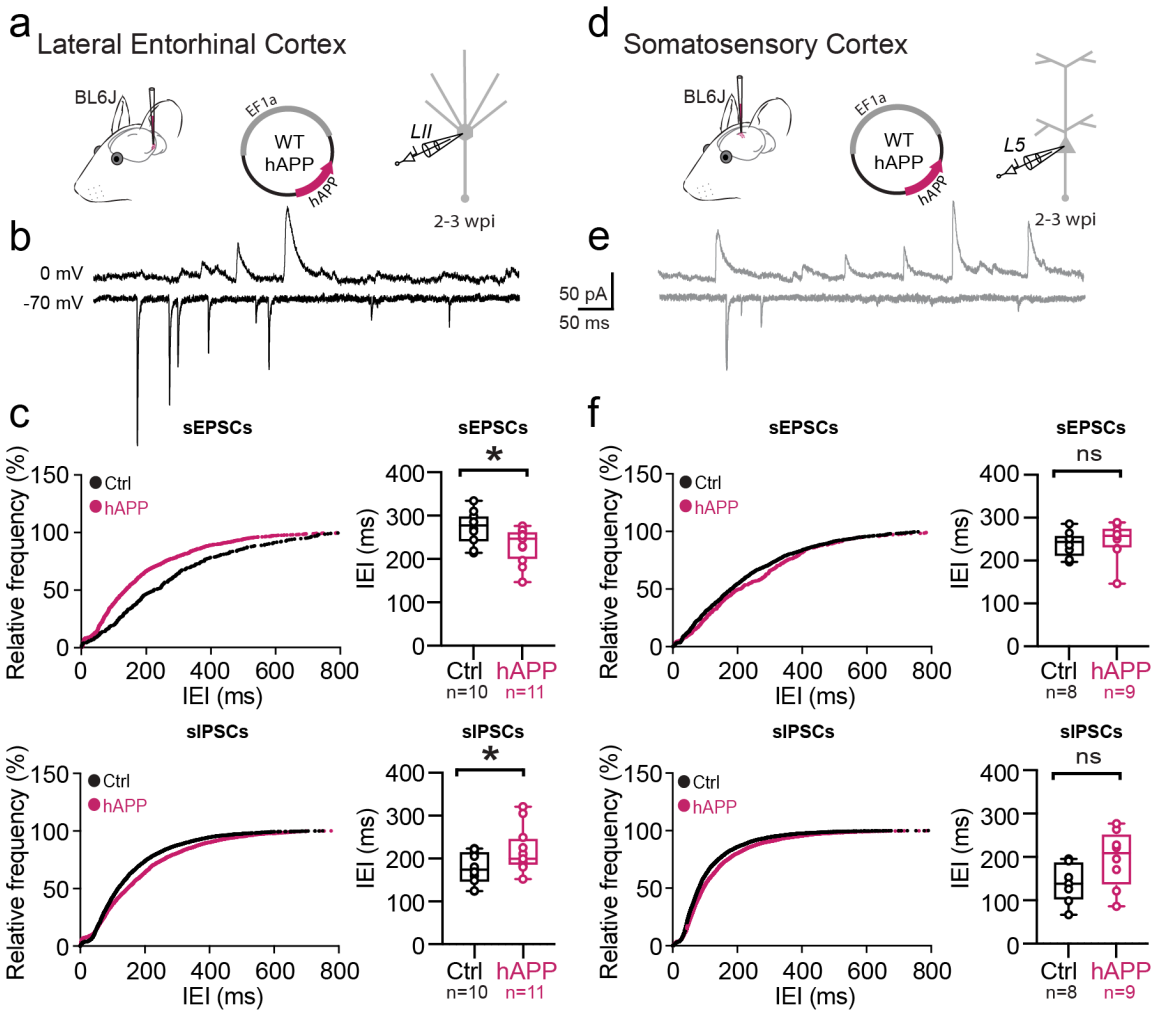

Figure 5. Human APP expression induces hyperexcitability in the LEC but not SS Ctx

a. Graphical summary of AAV.EF1a.hAPP (or for Ctrl, saline) stereotactic injection in the Lateral Entorhinal Cortex. Excitatory cells were targeted for whole-cell voltage-clamp recordings.

b. Spontaneous events obtained by holding cell voltage at 0 mV (inhibitory post-synaptic currents, IPSCs [top]) and -70 mV (excitatory post-synaptic currents, EPSCs [bottom]), interleaved.

849 **c. Top:** Cumulative distribution curve for spontaneous EPSCs in the LEC showing the relationship
850 of relative frequency of events to the inter-event interval (IEI) (left). Quantified averages of IEIs
851 are displayed for each cell as individual data points and compared between Ctrl (black) and hAPP
852 injected (magenta) conditions (right). L2 LEC sEPSCs show a significant reduction in the IEIs
853 (231.7 ± 12.25 ms, 272.7 ± 12.24 ms, hAPP and Ctrl respectively, p=0.029, t=2.361, df=19, two-
854 tailed unpaired t-test). See Extended Data Fig. 13 for mEPSC data. **Bottom:** Cumulative
855 distribution curve for spontaneous IPSCs in the LEC showing the relationship of relative frequency
856 of events to the inter-event interval (left). Quantified averages of IEIs are displayed for each cell
857 as individual data points and compared between Ctrl (black) and hAPP injected (magenta)
858 conditions (right). L2 LEC sIPSCs show a significant increase in the IEIs (219.9 ± 15.84 ms, 177.3
859 ± 12.02 ms, hAPP and Ctrl respectively, p=0.047, t=2.097, df=19, two-tailed unpaired t-test). See
860 Extended Data Fig. 13 for mIPSC data.
861 **d.** Graphical summary of AAV.EF1a.hAPP (or for Ctrl, saline) stereotactic injection in the
862 Somatosensory Cortex. Excitatory cells were targeted for whole-cell voltage-clamp recordings.
863 **e.** Spontaneous events obtained by holding cell voltage at 0 mV (IPSCs [top]) and -70 mV (EPSCs
864 [bottom]), interleaved.
865 **f. Top:** Cumulative distribution curve for spontaneous EPSCs in the SS Ctx showing the
866 relationship of relative frequency of events to the IEIs (left). Quantified averages of IEI are
867 displayed for each cell as individual data points and compared between Ctrl (black) and hAPP
868 injected (magenta) conditions (right). L5 SS Ctx sEPSCs show no change in the IEIs (p=0.7372,
869 t=0.3450, df=15; two-tailed unpaired t-test). See Extended Data Fig. 13 for mEPSC data. **Bottom:**
870 Cumulative distribution curve for spontaneous IPSCs in the SS Ctx showing the relationship of
871 relative frequency of events to the inter-event interval (left). Quantified averages of IEIs are
872 displayed for each cell as individual data points and compared between Ctrl (black) and hAPP
873 injected (magenta) conditions (right). L5 SS Ctx sIPSCs show no change in the IEIs (p=0.0812,
874 t=1.890, df=15; two-tailed unpaired t-test). See Extended Data Fig. 13 for mIPSC data.
875
876
877
878
879

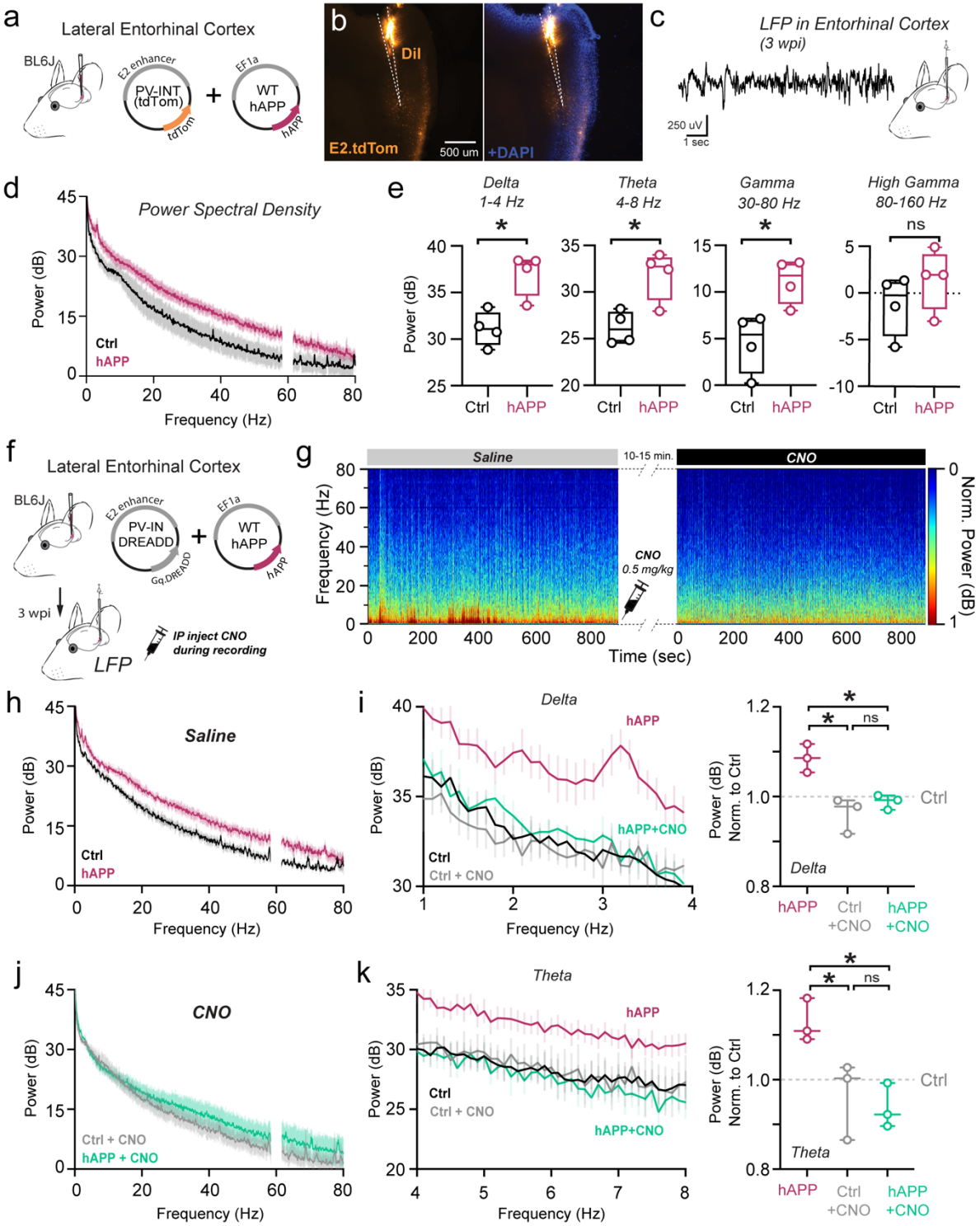

Figure 6. hAPP-induced hyperexcitability observed in vivo can be attenuated by enhancement of PV interneuron excitability

884 **a.** Graphical summary of AAV.EF1a.hAPP (or for Ctrl, E2.tdTom) stereotactic injection in the
885 Lateral Entorhinal Cortex.
886 **b.** 3 weeks post-injection, mice were anesthetized for *in vivo* glass electrode LFP recordings. (b)
887 is a representative slice at 10x magnification from the LEC where DiI coated electrode recorded
888 from a patch of E2.tdTom+ expressing cells.
889 **c.** Raw LFP signal from *in vivo* glass electrode recordings.
890 **d.** Power Spectral Density [PSD] analysis (dark lines: mean, light lines: ±SEM) comparing Ctrl
891 (E2.tdTom+saline injected) to hAPP (E2.tdTom+hAPP injected).
892 **e.** Power derived from PSD analysis averaged for each mouse in the Delta (1-4 Hz), Theta (4-12
893 Hz), Gamma (30-80 Hz), and High Gamma (80-160 Hz) frequency ranges and compared between
894 Ctrl and hAPP. Delta (Ctrl: 31.11± 0.94, Min. 28.86, Max. 33.43, Range. 4.57; hAPP: 37.02 ±
895 1.15, Min. 33.62, Max. 38.43, Range. 4.81; p=0.0073, t=3.98, df=6); Theta (Ctrl: 26.20± 0.88,
896 Min. 24.57, Max. 28.22, Range. 3.65; hAPP: 31.86 ± 1.34, Min. 27.97, Max. 33.98, Range. 6.01;
897 p=0.012, t=3.54, df=6), Gamma (Ctrl: 4.56± 1.59, Min. 0.24, Max. 7.13, Range. 6.89; hAPP: 11.17
898 ± 1.20, Min. 8.01, Max. 13.15, Range. 5.14; p=0.016, t=3.32, df=6), High Gamma (Ctrl: -1.22±
899 1.63, Min. -5.76, Max. 1.35, Range. 7.11; hAPP: 1.49 ± 1.65, Min. -2.98, Max. 4.97, Range. 7.96;
900 p=0.2864, t=1.170, df=6). Individual data points and box plots are displayed. Statistical
901 significance is denoted as *p<0.05, as determined by two-tailed unpaired t-test.
902 **f.** Graphical summary of AAV.E2.Gq.DREADD with AAV.EF1a.hAPP (or for Ctrl DREADD,
903 E2.Gq.DREADD + E2.tdTom) stereotactic injection in the Lateral Entorhinal Cortex. 3 weeks
904 post-injection, mice were anesthetized for *in vivo* glass electrode LFP recordings with
905 administration of saline or 0.5 mg/kg administration of Clozapine-n-oxide [CNO] during the
906 recording with a wait time after administration of 10-15 minutes prior to recording.
907 **g.** Spectrogram heatmap of LFP power (normalized) from the recording of one mouse after
908 intraperitoneal saline injection (left, 15 min.) and intraperitoneal CNO injection (right, 15 min.).
909 **h.** Power Spectral Density analysis (dark lines: mean, light lines: ±SEM) comparing Ctrl
910 DREADD (E2.Gq.DREADD + E2.tdTom + saline) to hAPP DREADD (E2.Gq.DREADD +
911 E2.tdTom + hAPP).
912 **i. [Left]** Power Spectral Density analysis only for the Delta frequency range (1-4 Hz) (dark lines:
913 mean, light lines: ±SEM) comparing Ctrl DREADD (black), Ctrl DREADD after CNO (Gray),
914 hAPP DREADD (maroon), and hAPP DREADD after CNO (green). **[Right]** Power [derived from

PSD analysis] averaged for each mouse in the Delta frequency range. (hAPP to Ctrl DREADD +CNO: p= 0.0063, hAPP DREADD to hAPP DREADD +CNO: p= 0.0193, Ctrl DREADD + CNO to hAPP DREADD + CNO: p= 0.5758, df=7, One-Way ANOVA with Multiple Comparisons).

j. Power Spectral Density analysis (dark lines: mean, light lines: ±SEM) comparing Ctrl DREADD after 0.5 mg/kg Clozapine-n-oxide [CNO] injection (E2.Gq.DREADD + E2.tdTom + saline) to hAPP DREADD after 0.5 mg/kg CNO injection (E2.Gq.DREADD + E2.tdTom + hAPP).

k. [Left] Power Spectral Density analysis only for the Theta frequency range (4-10 Hz) (dark lines: mean, light lines: ±SEM) comparing Ctrl DREADD (black), Ctrl DREADD after CNO (Gray), hAPP DREADD (maroon), and hAPP DREADD after CNO (green). **[Right]** Power [derived from PSD analysis] averaged for each mouse in the Theta frequency range. (hAPP to Ctrl DREADD +CNO: p= 0.0493, hAPP DREADD to hAPP DREADD +CNO: p= 0.0261, Ctrl DREADD + CNO to hAPP DREADD + CNO: p= 0.8593, df=7, One-Way ANOVA with Multiple Comparisons).

Also see Extended Data Figure 14 for related datasets.

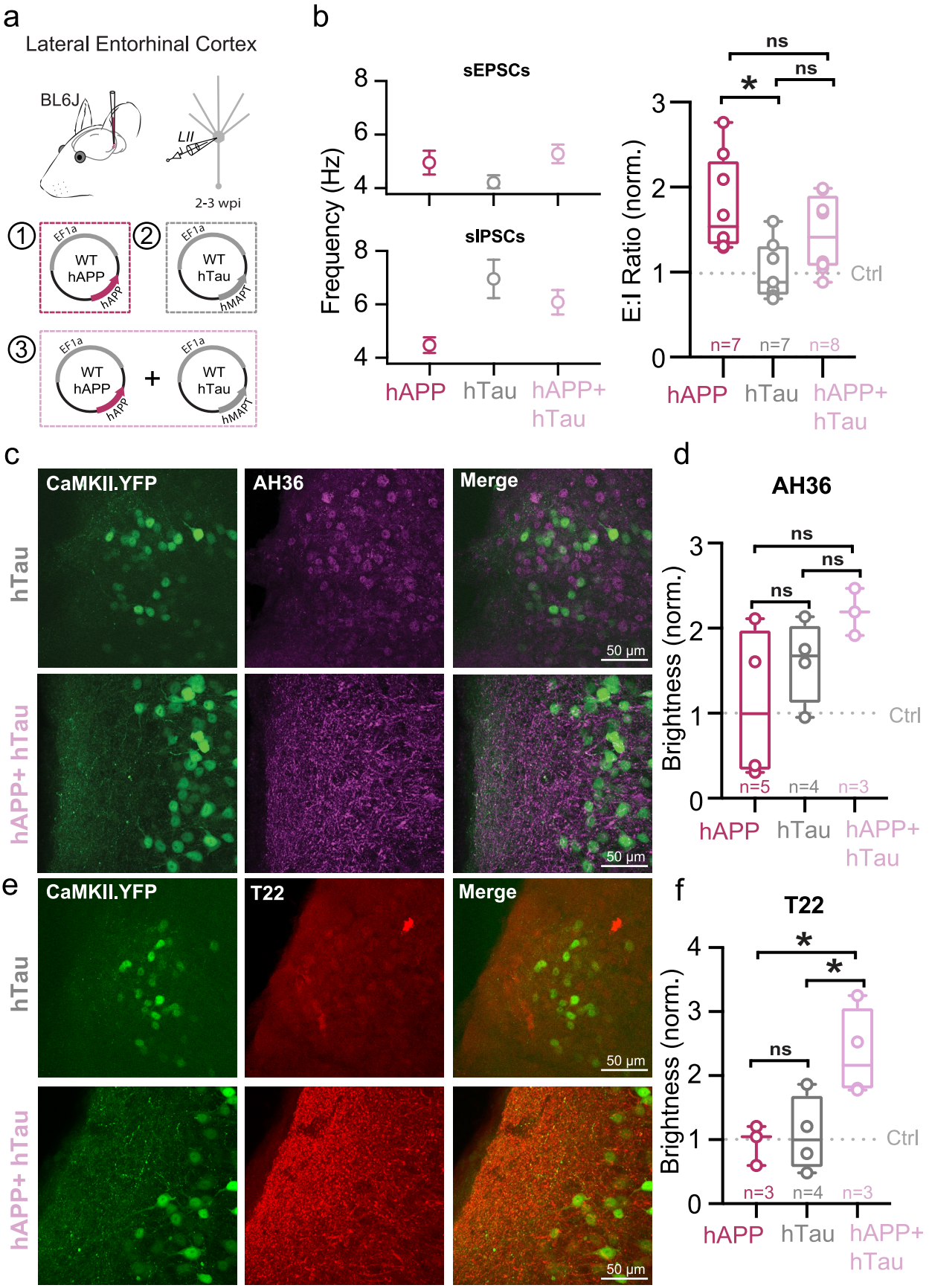
a
Lateral Entorhinal Cortex
BL6J
LII
2-3 wpi
EF1a
WT hAPP
hAPP
WT hTau
hMAPT
b
sEPSCs
sIPSCs
Frequency (Hz)
hAPP
hTau
hAPP+ hTau
E:I Ratio (norm.)
ns
*
Ctrl
n=7
n=7
n=8
c
CaMKII.YFP
AH36
Merge
hTau
hAPP+ hTau
50 µm
d
AH36
Brightness (norm.)
n=5
n=4
n=3
e
T22
f
n=3
n=4
n=3

929

930 **Figure 7. hTau co-expression with hAPP quells hyperexcitability but increases pathological**
931 **tau**
932 **a.** Graphical summary of AAV.EF1a.hAPP, AAV.EF1a.MAPT (hTau), or co-injected
933 AAV.EF1a.hAPP with AAV.EF1a.MAPT stereotactic injection in the Lateral Entorhinal Cortex.
934 Excitatory cells were targeted for whole-cell voltage-clamp recordings.
935 **b.** Spontaneous events obtained by holding cell voltage at -70 mV (excitatory post-synaptic
936 currents, EPSCs [top]) and 0 mV (inhibitory post-synaptic currents, IPSCs [bottom]), interleaved.
937 Quantified averages of event frequency are displayed for each cell normalized to Ctrl values as a
938 ratio of EPSC Frequency to IPSC frequency and compared between hAPP injected (magenta),
939 hTau injected (gray) and hAPP + hTau co-injected (pink) conditions. L2 LEC injected with hAPP
940 showed a significantly elevated E:I ratio compared to hTau injected ($p=0.0136$, $df=20$). hAPP and
941 hTau co-injected E:I ratio was not significantly different from hAPP injected ($p=0.3323$, $df=20$)
942 or hTau injected ($p=0.2175$, $df=20$). For all summary graphs, data are expressed as mean (± SEM).
943 Statistical significance is denoted as *=$p<0.05$, as determined by an Ordinary one-way ANOVA
944 with Multiple comparisons.
945 **c,e.** IHC representative images at 60x magnification for hTau (top) or hAPP+hTau (bottom)
946 injected mice (for Ctrl or hAPP injected, see Extended Data Fig. 15) with staining for either AH36
947 (c) or T22 (e).
948 **d.** hAPP, hTau, and hAPP+hTau were analyzed for AH36 brightness in the first 100 um of every
949 slice. AH36 brightness was normalized to CaMKII.eYFP brightness to control for any potential
950 variability in viral expression. All groups were then normalized to the Ctrl injected condition.
951 hAPP+hTau showed the highest level of AH36 brightness, although it was not significant over
952 hAPP ($p=0.1267$) or hTau ($p=0.4900$) ($df=8$, One-Way ANOVA with Multiple Comparisons).
953 hAPP and hTau were also not significantly different ($p=0.5328$).
954 **e.** hAPP, hTau, and hAPP+hTau were analyzed for T22 brightness in the first 100 um of every
955 slice. AH36 brightness was normalized to CaMKII.eYFP brightness to control for any potential
956 variability in viral expression. All groups were then normalized to the Ctrl injected condition.
957 hAPP+hTau showed a significantly higher level of T22 brightness, above both hAPP ($p=0.0350$)
958 and hTau ($p=0.0.0389$) ($df=8$, One-Way ANOVA with Multiple Comparisons). hAPP and hTau
959 were not significantly different ($p=0.9526$).
960

961 **Methods**

962

963 *Acute slice preparation*

964 All animal procedures were approved by the Emory University IACUC. Acute slices from SS
965 cortex and LEC were prepared from a mixture of C57Bl/6J and PV-Cre mice (8-12 weeks old),
966 evenly dispersed between test and control groups. Male and female mice were used for all
967 experiments with data collected from ≥ 3 mice per experimental condition. Mice were first
968 anesthetized and then killed by decapitation. The brain was then immediately removed by
969 dissection in ice-cold cutting solution (in mM) 87 NaCl, 25 NaHO3, 2.5 KCl, 1.25 NaH2PO4, 7
970 MgCl2, 0.5 CaCl2, 10 glucose, and 7 sucrose. Brain slices (250 µm) were sectioned in the sagittal
971 plane using a vibrating blade microtome (VT1200S, Leica Biosystems) in the same solution. Slices
972 were transferred to an incubation chamber and maintained at 34°C for ~30 min and then at 23-
973 24°C thereafter. During whole-cell recordings, slices were continuously perfused with (in mM)
974 128 NaCl, 26.2 NaHO3, 2.5 KCl, 1 NaH2PO4, 1.5 CaCl2, 1.5MgCl2 and 11 glucose, maintained
975 at 30.0±0.5°C. All solutions were equilibrated and maintained with carbogen gas (95% O2/5%
976 CO2) throughout.

977

978 *Slice Electrophysiology*

979 PV interneurons and excitatory cells were targeted for somatic whole-cell recording in layer 5
980 region of somatosensory cortex or layer 2 lateral entorhinal cortex by combining gradient-contrast
981 video-microscopy with epifluorescent illumination on custom-built or commercial (Olympus)
982 upright microscopes. Electrophysiological recordings were acquired using Multiclamp 700B
983 amplifiers (Molecular Devices). Signals were filtered at 10 kHz and sampled at 50 kHz with the
984 Digidata 1440B digitizer (Molecular Devices). For whole cell recordings, borosilicate patch
985 pipettes were filled with an intracellular solution containing (in mM) 124 potassium gluconate, 2
986 KCl, 9 HEPES, 4 MgCl2, 4 NaATP, 3 L-Ascorbic Acid and 0.5 NaGTP. For experiments
987 recording spontaneous and miniature events, an intracellular solution containing (in mM) 120
988 CsMeSO4, 10 HEPES, 5 TEA.Cl, 4 Na2ATP, 0.5 Na2GTP, 2 MgCl2, 10 L-Ascorbic Acid, and 3
989 Qx314. To obtain miniature events, slices were perfused with 1 µM TTX for 10 minutes prior to
990 recording (at least 10 mL run). The same protocol was used for spontaneous and miniature events.
991 In patch experiments using exogenously applied amyloid, slices were incubated in an equal

992 mixture of 0.25 μM $A\beta_{1-40}$ and $A\beta_{1-42}$, as described previously[10]. LEC slices were incubated with
993 this solution for 3h before being transferred to standard extracellular solution for patch recordings.
994 Pipette capacitance was neutralized in all recordings and electrode series resistance compensated
995 using bridge balance in current clamp. Liquid junction potentials were uncorrected. Recordings
996 had a series resistance < 20 MΩ. Membrane potentials were maintained near -70 mV during current
997 clamp recordings using constant current bias. Action potential trains were initiated by somatic
998 current injection (300 ms) normalized to the cellular capacitance in each recording measured
999 immediately in voltage clamp after breakthrough[78]. For quantification of individual AP
1000 parameters, the 1st AP in a spike train at was analyzed at 12 pA/pF for all cells. Passive properties
1001 were determined by averaging the responses of several 100 ms long, -20pA steps during each
1002 recording. Spontaneous and miniature events were recorded at a holding voltage of -70 and 0 mV,
1003 one second each, interleaved for 3-5 minutes. Statistical analyses of spontaneous and miniature
1004 events using cell averages, to avoid bias in favor of cells which may receive more inputs or less[74,79].
1005 For regional comparisons of PV interneurons, combined controls from datasets in each region were
1006 used. Event detection was carried out using Clampfit (Molecular Devices) using a template
1007 matching algorithm and were curated manually with a 4 kHz low-pass filter.
1008
1009 *In vivo Electrophysiology:*
1010 Electrophysiological recordings (Local Field Potential) were performed in lightly anesthetized
1011 animals (1% v/v isoflurane). Pipettes (1–3 MΩ) with a long shank (~2 cm) were pulled from
1012 borosilicate glass capillaries (1.65mm O.D, #PG52615-4, Sutter instruments Co., USA) using a
1013 vertical puller (Narishige PC-100), coated with Sylgard (DOW), baked in a convection oven at
1014 145 °F for 30 min, and allowed to cool prior to use. The reference electrode (silver chloride) was
1015 implanted in the contralateral cerebellum. For recordings, pipettes were filled with sterile saline,
1016 coated with DiI, slightly trimmed, and placed onto the silver chloride wire. Positive pressure (52-
1017 53.9 mBar) was applied to the pipettes during entry into the cortex and then reduced to <1.0 mBar
1018 prior to recording. Recordings were conducted at the same coordinates as the injection site in the
1019 LEC (X = ± 3.39; Y = −4.52; α = 0°, Z= −2.0). Electrophysiological recordings were acquired
1020 using Multiclamp 700B amplifiers (Molecular Devices). Signals were filtered at 4 kHz (Bessel)
1021 and sampled at 10 kHz with the Digidata 1440B digitizer (Molecular Devices). For each session,
1022 3-5 5 minute recording sessions were completed. Each animal was first injected intraperitoneally

1023 with sterile saline, and after a 15 minute wait period were recorded. Subsequently, each animal
1024 was injected with 0.5 mg/kg Clozapine N-oxide dihydrochloride (#6329, TOCRIS) reconstituted
1025 in sterile saline. Data was analyzed offline. 30 minutes of recording (total) were analyzed for each
1026 mouse: 15 minutes of saline IP injected condition and 15 minutes of the CNO injected condition.
1027 LFP recordings were subjected to a fast-Fourier transformation (FFT) and converted to Power in
1028 decibels using custom code to achieve a power spectral density analysis. Data points for each
1029 frequency range (Delta-High Frequency Oscillations) were averaged for each mouse in each
1030 condition to compare for statistical analysis. Statistical analysis was completed using GraphPad
1031 Prism. Confirmation of electrode location was completed post-hoc with imaging of LEC sagittal
1032 slices on the Nikon Eclipse Ti-E microscope.
1033
1034 *Intracranial viral injections*
1035 5-9 week old mice were injected with AAV(PHP.eB).E2.tdTom with saline or
1036 AAV(PHP.eB).EF1a.hAPP (0.3 μL total, 1:1) in the SBFI vibrissal region of cortex or the Lateral
1037 Entorhinal Cortex. For murine APP experiments AAV(PHP.eB).EF1a.hAPP was replaced with
1038 AAV(PHP.eB).EF1a.mAPP. For murine APP/hAB chimera experiments,
1039 AAV(PHP.eB).EF1a.mAPP/hAB was used. For tau experiments, the four conditions were: Ctrl
1040 (CaMKII.eYFP: saline 1:2), hAPP (EF1a.hAPP: CaMKII.eYFP: saline, 1:1:1), hTau
1041 (AAV(PHP.eB).EF1a.hMAPT: CaMKII.eYFP: saline, 1:1:1), and hAPP+hTau (EF1a.hAPP:
1042 Ef1a.hMAPT: CaMKII.eYFP, 1:1:1). For DREADD experiments, animals were injected with
1043 AAV.E2.Gq.DREADD and AAV(PHP.eB).E2.tdTom and either AAV(PHP.eB).EF1a.hAPP or
1044 sterile saline (1:1:1). When performing intracranial viral injections, mice were head-fixed in a
1045 stereotactic platform (David Kopf Instruments) using ear bars, while under isoflurane anesthesia
1046 (1.5 - 2.0%). Thermoregulation was provided by a heating plate using a rectal thermocouple for
1047 biofeedback, thus maintaining core body temperature near 37°C. Bupivacaine was subcutaneously
1048 injected into the scalp to induce local anesthesia. A small incision was opened 5-10 minutes
1049 thereafter and a craniotomy was cut in the skull (< 0.5 μm in diameter) to allow access for the glass
1050 microinjection pipette. Coordinates (in mm from Bregma) for microinjection in the SS Cortex were
1051 X = ± 0.85; Y = −2.5; α = 0°; Z = −0.85, coordinates for the LEC were X = ± 3.39; Y = −4.52; α
1052 = 0°, Z= −2.4, −1.5. Viral solution (titer $1x10^{09}$ to $1x10^{13}$ vg/mL) was injected slowly (~0.02 μL
1053 min-1) by using a Picospritzer (0.3 μL total). After ejection of virus, the micropipette was held in

1054 place (5 min) before withdrawal. The scalp was closed with surgical sutures and Vetbond (3M)
1055 tissue adhesive and the animal was allowed to recover under analgesia provided by injection of
1056 carprofen and buprenorphine SR. After allowing for onset of expression, animals were sacrificed
1057 acute slices were harvested.
1058
1059 *Retro-orbital (RO) injection*
1060 Male and female mice were given AAV retro-orbital injections as previously described[80]. Mice
1061 were anesthetized with 1.8-2% isoflurane. AAV(PHP.eB).E2.Cre.2A.GFP virus was titrated to
1062 $2.4x10^{11}$ vector genomes total was accompanied by AAV(PHP.eB).Flex.tdTom titrated to $3.1x10^{11}$
1063 and injected in TurboID+ mice[20] to label PV interneurons throughout cortex. Titrated virus was
1064 injected into the retro-orbital sinus of the left eye with a 31G x 5/16 TW needle on a 3/10 mL
1065 insulin syringe. Mice were kept on a heating pad for the duration of the procedure until recovery
1066 and then returned to their home cage. After 3 weeks post-injection, mice were provided with biotin
1067 water continuously. Biotin water was administered for 2 weeks until acute slice sample collection
1068 (total of 5 weeks post-RO injection).
1069
1070 *CIBOP studies*
1071 PV-CIBOP studies were performed by single retro-orbital injections of
1072 AAV(AAV(PHP.eB).E2.Cre.2A.GFP) as described above to Rosa26TurboID/wt mice and WT
1073 littermate animals at 7 weeks of age, as previously described[21]. Control groups in PV-CIBOP
1074 studies also received AAV E2.Cre injections for fair comparisons. After 3 weeks to allow Cre-
1075 mediated recombination and TurboID expression, biotinylation (37.5 mg/L in drinking water) was
1076 performed for 2 weeks[20]. After 5 weeks (total), acute slices were acquired as described above, with
1077 subsequent microdissection of the SS Ctx or the LEC.
1078
1079 *Tissue processing for protein-based analysis, including Western Blot (WB)*
1080 Tissue processing for proteomic studies, including Mass Spectrometry (MS), were performed
1081 similarly to previous CIBOP studies[20,21]. Frozen brain tissues (whole brain homogenate excluding
1082 cerebellum for WB and microdissected cortical regions for Fig 1) either intact or dissected cortex,
1083 was weighed and added to 1.5mL Rino tubes (Next Advance) containing stainless-steel beads (0.9-
1084 2mm in diameter) and six volumes of the tissue weight in urea lysis buffer (8 M urea, 10 mM

1085 Tris, 100 mM NaH2PO4, pH 8.5) containing 1X HALT protease inhibitor cocktail without EDTA
1086 (78425, ThermoFisher). Tissues were homogenized in a Bullet Blender (Next Advance) twice for
1087 5 min cycles at 4 °C. Tissue were further sonicated consisting of 5 seconds of active sonication
1088 at 20% amplitude with 5 seconds incubation periods on ice. Homogenates were let sit for 10
1089 minutes on ice and then centrifuged for 5 min at 12,000 RPM and the supernatants were
1090 transferred to a new tube. Protein concentration was determined by BCA assay using Pierce™
1091 BCA Protein Assay Kit (23225, Thermofisher scientific). For WB analyses, 10µg of protein from
1092 brain lysates were used to verify TurboID expression (anti-V5) and biotinylation (streptavidin
1093 fluorophore conjugate). Standard WB protocols, as previously published, were followed[20]. All
1094 blots were imaged using Odyssey Infrared Imaging System (LI-COR Biosciences) or by
1095 ChemiDoc Imaging System (Bio-Rad) and densitometry was performed using ImageJ software.
1096
1097 *Enrichment of biotinylated proteins from CIBOP brain*
1098 As per CIBOP protocols previously optimized[20], biotinylated proteins were captured by
1099 streptavidin magnetic beads (88817; Thermofisher Scientific) in 1.5 mL Eppendorf LoBind tubes
1100 using 83uL beads per 1mg of protein (here 200 µg of protein with 16.6 µL of beads) in a 500 µL
1101 RIPA lysis buffer (RLB)(50 mM Tris, 150 mM NaCl, 0.1% SDS, 0.5% sodium deoxycholate,
1102 1% Triton X-100). In brief, the beads 16.6 µL beads were washed twice with 1 ml of RLB and
1103 200µg of protein were incubated by making up the total volume of the solution up to 500 µl using
1104 RPL. After incubation at 4 deg C for 1 h with rotation, beads were serially washed at room
1105 temperature (twice with 1 mL RIPA lysis buffer for 8 min, once with 1 mL 1 M KCl for 8 min,
1106 once with 1 mL 0.1 M sodium carbonate (Na2CO3) for ~10 s, once with 1 mL 2 M urea in
1107 10 mM Tris-HCl (pH 8.0) for ~10 s, and twice with 1 mL RIPA lysis buffer for 8 min), followed
1108 by 1 RIPA lysis buffer wash 4 final PBS washes. Finally, after placing the tubes on the magnetic
1109 rack, PBS was removed completely, then the beads were further diluted in 100 µl of PBS. The
1110 beads were mixed and 10% of this biotinylated protein coated beads were used for quality control
1111 studies to verify enrichment of biotinylated proteins (including WB and silver stain of proteins
1112 eluted from the beads). Elution of biotinylated protein was performed by heating the beads in
1113 30 µL of 2X protein loading buffer (1610737; BioRad) supplemented with 2 mM biotin + 20 mM
1114 dithiothreitol (DTT) at 95°C for 10 min. The remaining 90% of sample were stored at -20°C for
1115 western blot or mass spectrometric analysis of biotinylated protein.

1116

1117 *Western blotting and Silver Stain*

1118 To confirm protein enrichment on the pulldown samples the protein were eluted from the beads as
1119 mentioned above and 1/3rd of the eluted protein was resolved on a 4–12% Bris-Tris gel (Invitrogen:
1120 cat# NW04125box) and transferred onto transferred onto iBlot 2 Transfer Stack containing
1121 nitrocellulose membrane using the BOLT transfer system. The membranes were washed once with
1122 TBS-T (0.1% tween-20) and then blocked with Start Block (37543, Thermofisher Scientific) for 1
1123 h. The membrane was then probed with streptavidin-Alexa-680 diluted in Start Block for 1 h at
1124 room temperature. Further, the membranes were washed 3 times and biotinylated proteins were
1125 detected on Odyssey Infrared Imaging System (LI-COR Biosciences). In parallel, 2/3rd of the
1126 eluted protein samples were resolved on a 4–12% Bris-Tris gel (Invitrogen: cat# NW04125box)
1127 and subjected to Silverstein (Pierce™ Silver Stain Kit: Catalog number: 24612) to detect the total
1128 amount of protein in each lane according to the manufactured protocol.

1129

1130 *Protein digestion, MS, protein identification and quantification*

1131 On-bead digestion of proteins (including reduction, alkylation followed by enzymatic digestion by
1132 Trypsin and Lys-C) from SA-enriched pulldown samples (1mg protein used as input) and
1133 digestion of bulk brain (input) samples (25 µg protein), were performed as previously described
1134 with no protocol alterations[20,21]. In brief, after the removal of PBS from remaining 90% of
1135 streptavidin beads (10% used for quality control using western blot and silver stain) were
1136 resuspended in 90 uL of 50 mM ammonium bicarbonate (NH4HCO3) buffer. Biotinylated
1137 proteins were then reduced with 1 mM DTT and further alkylated with 5 mM iodoacetamide
1138 (IAA) in the dark for 30 min each on shaker. Proteins were digested overnight with 0.2 µg of
1139 lysyl (Lys-C) endopeptidase (127-06621; Wako) at RT on shaker followed by further overnight
1140 digestion with 0.4 µg trypsin (90058; ThermoFisher Scientific) at RT on shaker. The resulting
1141 peptide solutions were acidified to a final concentration of 1% formic acid (FA) and 0.1%
1142 triflouroacetic acid (TFA), desalted with a HLB columns (Cat#186003908; Waters). The resulting
1143 protein solution was dried in a vacuum centrifuge (SpeedVac Vacuum Concentrator). Detailed
1144 methods for this protocol have been previously published[20]. Lyophilized peptides were
1145 resuspended followed by liquid chromatography and MS (Q-Exactive Plus, Thermo, data
1146 dependent acquisition mode) as per previously published protocols[20]. As previously published[81-

1147 [83], MS raw data files were searched using SEQUEST, integrated into Proteome Discoverer
1148 (ThermoFisher Scientific, version 2.5) using the Uniprot 2020 database as reference (91,441 target
1149 37 sequences including V5-TurboID). Raw MS data as well as searched Proteome Discoverer data
1150 before and after processing to handle missing values, will be uploaded to the ProteomeXchange
1151 Consortium via the PRIDE repository[84]. The false discovery rate (FDR) for peptide spectral
1152 matches, proteins, and site decoy fraction were 1 %. Other quantification settings were similar to
1153 prior CIBOP studies[20]. Quantitation of proteins was performed using summed peptide abundances
1154 given by Proteome Discoverer. We used razor plus unique peptides for protein level quantitation.
1155 The Proteome Discoverer output data were uploaded into Perseus (Version 1.6.15) and abundance
1156 values were log2 transformed, after which data were filtered so that >50% of samples in a given
1157 CIBOP group expected to contain biotinylated proteins, were non-missing values. Protein
1158 intensities from SA-enriched pulldown samples (expected to have biotinylated proteins by
1159 TurboID) were normalized to sum column intensities prior to comparisons across groups. This was
1160 done to account for any variability in level of biotinylation as a result of variable Cre-mediated
1161 recombination, TurboID expression and/or biotinylation[20].
1162
1163 *Analysis of enrichment of cognitive resilience proteins in regional PV interneuron DEPs*
1164 We cross-referenced PV-CIBOP regional proteins (N=207, unadjusted $p<0.05$) with proteins
1165 previously found to be associated with cognitive decline in humans (N=55 proteins associated with
1166 cognitive slope in the Religious Orders Study and the Rush Memory and Aging Project
1167 (ROSMAP), unadjusted $p<0.05$)[21,22]. In this prior study, cognitive slope was estimated in the
1168 ROSMAP longitudinal study of aging, and cognitive slope was correlated with post-mortem
1169 protein abundances, measured by quantitative MS. Proteins that were associated with stable
1170 cognitive function (positive association with cognitive slope) were identified as protein markers
1171 of cognitive resilience (or pro-resilience proteins). Conversely, proteins ante-correlated with
1172 cognitive stability were labeled as anti-resilience proteins. 55 resilience-associated proteins in
1173 ROSMAP were identified as regional DEPs in our PV-CIBOP study. The median correlation with
1174 cognitive slope for SS Ctx and LEC PV-CIBOP DEPs was estimated and compared across the two
1175 regions (two-tailed Mann-Whitney U test).
1176
1177 *Integration of PV-CIBOP proteomes with existing human AD proteomic datasets*

1178 We cross-referenced our PV-CIBOP regional proteomes with existing human post-mortem
1179 proteomes in which the entorhinal cortex (EC), frontal cortex (FC) and other regions were sampled
1180 from AD cases (early BRAAK stages I-III, late BRAAK stages IV-VI) and non-AD/non-pathology
1181 controls. Proteins were identified as DEPs if they were significantly different comparing AD
1182 versus controls within any given region (total of 737 DEPs identified). PV-CIBOP proteins
1183 identified by our current study were further assessed for evidence of regional differences within
1184 PV interneurons (SS Ctx vs. LEC).
1185
1186 *Assessment of human tau/APP protein-protein interactors among PV-CIBOP regional DEPs*
1187 We cross-referenced our PV-CIBOP regional proteomic data with human tau protein interactors,
1188 previously identified in a meta-analysis across 12 published tau interactome studies[24], in which
1189 2,084 human tau interactors were identified, and among these, 261 were high-confidence
1190 interactors if they were identified by at least 3 studies. PV-CIBOP proteins in our study that were
1191 also found among these 216 human tau interactors, were further analyzed for evidence of regional
1192 differences (SS Ctx vs. LEC) in PV interneurons. The proportions of tau interactors and non-tau
1193 interactors across SS Ctx-enriched, LEC-enriched and non-regional PV interneuron proteins were
1194 compared (Chi square test).
1195 Using a similar approach, we obtained a list of 243 human APP interactors derived from protein-
1196 protein-interaction databases (STRING consortium 2023, Version 12.0, https://string-db.org/)
1197 restricting the interactome to physical interactors with medium confidence stringency (confidence
1198 scores >0.40, including text mining, experiments and databases). We excluded proteomic studies
1199 of extracellular amyloid beta plaques as these are less likely to represent interactions relevant to
1200 intra-neuronal APP processing.
1201
1202 *RNAscope*
1203 RNAscope was performed for confirmation of viral hAPP and mAPP expression, as well as
1204 quantification of viral expression in a cell-type-specific manner. RNAscope was performed as
1205 instructed by Advanced Cell Diagnostics (ACD). Tissue was prepared from C57Bl/6J mice (8-12
1206 weeks old), evenly dispersed between test and control groups. Male and female mice were used
1207 for all experiments with data collected from ≥ 3 mice per experimental condition. Mice were
1208 injected with AAV(PHP.eB).E2.tdTom and AAV(PHP.eB).hAPP or AAV(PHP.eB).mAPP (0.3

1209 uL total, 1:1) in one hemisphere and injected contralaterally with AAV(PHP.eB).E2.tdTom and
1210 saline (0.3 uL total, 1:1), n=3 each. Hemispheres were randomized. After 2-3 weeks, mice were
1211 first anesthetized and then killed by decapitation. The brain was then immediately removed and
1212 flash frozen in isopentane on dry ice. Samples were kept at -80°C prior to sectioning. Tissue was
1213 sectioned on a cryostat at 16 µm thickness, mounted onto Superfrost Plus Slides, and stored at -
1214 80°C until use. Samples were fixed and dehydrated according to the RNAscope kit manufacturer
1215 (ACDBio) standard protocol. In brief, frozen slides containing tissue sections were immediately
1216 dipped in pre-chilled 4% paraformaldehyde (PFA) for 15 minutes at room temperature. After
1217 fixation, slides were briefly rinsed with 1× phosphate buffered saline (PBS) two times to remove
1218 excess fixative. Tissue sections were then dehydrated in a series of ethanol solution 50%, 70% and
1219 100% for 5 min at room temperature. After ethanol washes the slides were transferred into a fresh
1220 100% ethanol solution to sit overnight at -20°C. The following day, slides were taken out of the
1221 ethanol solution, air dried for 5 minutes, and hydrophobic barriers were drawn around each section.
1222 The remainder of the RNAscope assay was then performed following the manufacturer's protocol,
1223 multiplexing two different probe groups on two different sections from each animal: 1) human
1224 APP (catalog #418321), mouse APP (catalog #519001-C2), and CaMKIIα (catalog #445231-C3),
1225 or 2) human APP, mouse APP, and Pvalb (catalog #421931-C3).
1226
1227 *Immunohistochemistry*
1228 Acute slices were acquired as previously described at 100 µm thickness. Immediately following
1229 collection from the vibratome, free-floating sections were placed in 4% paraformaldehyde for
1230 fixation at room temperature for 1-2 hours. Sections were then washed three times in 1x Tris
1231 Buffered Saline (1xTBS) for 10 minutes. To block nonspecific binding, the sections were then
1232 incubated with 5% goat serum (in 1xTBS) for 1 hour at room temperature. Sections were then
1233 incubated overnight at 4°C on a shaker plate in the primary antibody solution, which contained
1234 0.2% Triton X-100, 1% goat serum, and a 1:1000 dilution of either the AH36 antibody (StressMarq
1235 Sciences, #SMC-601) or T22 antibody (Millipore Sigma, #ABN454) in 1xTBS. The next day,
1236 sections were washed three times for 10 minutes in 1xTBS before incubation with the secondary
1237 antibody (Alexa Fluor™ 647 at 1:1000; ThermoFisher Scientific, #A-21245) in 1xTBS for 1 hour
1238 at room temperature on a shaker plate. From the point of secondary antibody incubation, sections
1239 were protected from light using aluminum foil. Following secondary antibody incubation, sections

1240 were washed again three times for 10 minutes in 1xTBS, mounted on slides (Fisher Scientific,
1241 #1255015), and coverslipped with Fluoromount containing DAPI (ThermoFisher Scientific, #00-
1242 4959-52). Slides were then imaged on a Nikon C2 laser-scanning confocal system with an inverted
1243 Nikon ECLIPSE Ti2 microscope. Imaging parameters (e.g., laser power, gain) were defined for
1244 each primary antibody and were kept consistent between all sections in that primary antibody
1245 group.
1246
1247 *Image Analysis*
1248 Images for analysis of RNAscope sections were taken on a Keyence BZ-X800 microscope
1249 (KEYENCE; Osaka, Japan) at 40X magnification. Two images were acquired of each mouse LEC
1250 hemisphere, and 4 sections were imaged per mouse (total: ~8 images/experiment for an n=3). The
1251 acquisition parameters were kept constant throughout imaging of all sections. Four fluorescent
1252 channels were used simultaneously; (1) the green channel was assigned for VIVID 520 dye (human
1253 APP probe), (2) the blue channel was used for DAPI nuclear stain, (3) the red channel was assigned
1254 for VIVID 570 dye (mouse APP probe), and (4) the far-red channel was assigned for VIVID 650
1255 dye (CaMKIIα or Pvalb probes). A z-stack was taken (with 1 μm steps) of each hemisphere, and
1256 the full focus feature in the Keyence BZ-X800 analysis software was applied to compress each 10
1257 μm z-stack. These compressed z-stacks were then used for image analysis in HALO v3.6 FISH-IF
1258 v2.1.4 (Indica Labs). For immunohistochemistry experiments, 2 sections were imaged per
1259 antibody per mouse (total: ~4 images/experiment for an n=3-5). The acquisition parameters were
1260 kept constant throughout imaging of all sections. Two channels were used simultaneously; (1) the
1261 green channel was assigned for CaMKII.eYFP expression, (2) the red channel was assigned for
1262 Alexa Fluor™ 647. For each slice, four line scans of 200 thickness were analyze from the pia to
1263 the end of the 60x photo (~180-200 μm total) using ImageJ software. Antibody brightness was
1264 normalized to CaMKII.eYFP expression for each condition to control for any slight variation in
1265 viral expression. The obtained data was then analyzed for figure generation in Prism (GraphPad).
1266 The process from sample fixation to image analysis covered a four-day time frame.
1267
1268 *Flow Cytometry*
1269 Flow cytometry was performed for the confirmation of viral hAPP protein expression. For positive
1270 control 5xFAD and their wild-type littermates were used and injected stereotactically in the

1271 somatosensory cortex with 1:1 ratio of AAV(PHP.eB).E2.GFP and saline (0.3 µL). While for
1272 hAPP expression C57Bl/6J were also stereotactically injected at a 1:1 ratio with
1273 AAV(PHP.eB).E2.GFP and saline or AAV(PHP.eB).hAPP (0.3 µL total). 2-3 weeks after the
1274 injections, mice were euthanized (8–10 weeks old) by decapitation and acute slices of 250 µm
1275 were obtained and then micro-dissected to isolate the cortical region containing GFP^+ expressing
1276 cells using an epi-fluorescent stereoscope (Olympus SZX12). Virus-injected microdisected
1277 regions of the brain were then placed into a cutting solution with 0.5 mg/mL protease (P5147–
1278 100MG, Sigma-Aldrich) for 60 minutes with continuous carbogen gas bubbling. Samples were
1279 then manually triturated in 300 µL of 1% PBS into a single-cell suspension. Cells were stained
1280 with a human-specific APP antibody (SIG-39320, Biolegend). Cells were first fixed in 1x fixation
1281 buffer (eBioscience; cat# 00-8222-49) for 30 min on ice, then washed 3x in PBS. Cells were then
1282 permeabilized for 30 min using 1x permeabilization buffer (eBioscience; cat# 00-8333-56) on ice.
1283 To determine the presence of hAPP in these cells, fixed and permeabilized cells were incubated
1284 with human-specific APP antibody (SIG-39320, Biolegend) at dilution 1:250 for 1 h. cells were
1285 then washed with permeabilization buffer 3 times and incubated for 30 minutes with a secondary
1286 antibody at dilution 1:500. Cells were finally washed 3 times with permeabilization buffer, as
1287 mentioned above. After the last wash, 250 µl of PBS was added, vortexed and kept on ice in the
1288 dark until flow cytometry was performed. Compensation was performed prior to the experiment
1289 using a single fluorophore labelled OneComp eBeads™ Compensation Beads (Catalog number:
1290 01-1111-41; Thermofisher).
1291
1292 *Statistics and Analysis*
1293 Custom python scripts, Axograph, Graphpad Prism (Graphpad Software), and Excel (Microsoft)
1294 were used for analysis with values in text and figures. Statistical differences were deemed
1295 significant with α values of $p < 0.05$. Two-tailed unpaired and paired t-tests were used for
1296 unmatched and matched parametric datasets, respectively. Where appropriate, group data were
1297 compared with 1 or 2-way ANOVA and significance between groups noted in figures was
1298 determined with Tukey's or Sidak's multiple post-hoc comparison tests. Normality was
1299 determined using D'Agostino & Pearson omnibus or Shapiro-Wilk tests. For permutation-based
1300 false discovery proportion (FDP) estimation, we used permFDP package in R [version 4.3.1],
1301 https://github.com/steven-shuken/permFDP for correcting p-values for multiple hypothesis

1302 testing. Using a family of unadjusted p values, and 500 permutations, this function returned the
1303 corrected rejection threshold to control false discovery (FDR<5%). For this dataset, the adjusted
1304 p-value threshold was 0.0431.
1305
1306 *K-means clustering and Principal Component Analysis*
1307 K-means clustering and Principal component analysis (PCA) were conducted on datasets from
1308 excitatory neurons and PV interneurons, respectively, in the LEC. All passive and active properties
1309 were used for each cell to conduct unsupervised clustering. Post-clustering and analysis, Ctrl or
1310 hAPP identities were restored to their respective cells.
1311
1312 *Analyses of MS data and bioinformatics analyses*
1313 Within each MS study, we compared bulk proteomes to SA-enriched proteomes to confirm that
1314 expected proteins (from either PV-INTs) were indeed enriched while nonneuronal proteins (e.g.
1315 glial proteins) were de-enriched as compared to bulk brain proteomes. We also identified proteins
1316 unique to bulk or SA-enriched pulldown samples. Within SA-enriched biotinylated proteins, we
1317 restricted our analyses to those proteins that were confidently biotinylated and enriched (based on
1318 statistical significance unadj. P<0.05 as well as 2-fold enrichment in biotinylated vs. non
1319 biotinylated samples). This allowed us to exclude proteins that were non-specifically enriched by
1320 streptavidin beads. Within biotinylated proteins, group comparisons were performed using a
1321 combination of approaches, including differential abundance analysis, hierarchical clustering
1322 analysis (Broad Institute, Morpheus, https://software.broadinstitute.org/morpheus), as well as
1323 PCA, (in SPSS Ver 26.0 or R). Differential abundance analyses were performed on log2
1324 transformed and normalized abundance values using two-tailed unpaired T-test for 2 groups
1325 assuming equal variance across groups or one-way ANOVA + post-hoc Tukey HSD tests for >2
1326 groups). Unadjusted and FDR-corrected comparisons were performed, although we relied on
1327 unadjusted p-values along with effect size (fold-enrichment) to improve stringency of analyses.
1328 After curating lists of differentially enriched proteins, gene set enrichment analyses (GSEA) were
1329 performed (AltAnalyze Ver 2.1.4.3) using all proteins identified across bulk and pulldown
1330 proteomes as the reference (background list). Protein-protein-interactions between proteins within
1331 lists of interest were examined using STRING
1332 (https://stringdb.org/cgi/input?sessionId=bqsnbjruDXP6&input_page_show_search=on)123. We

also performed GSVA of DEPs identified in bulk as well as PV interneuron proteomes from SS Ctx and LEC to complement GSEA[85,86]. As previously published, statistical differences in enrichment scores for each ontology comparing two groups, were computed by comparing the true differences in means against a null distribution which was obtained by 1000 random permutations of gene labels. Benjamini & Hochberg false discovery rate adjusted p values <0.05 were considered significant. The reference gene sets for GSVA were the M5 (Mouse) Ontology Gene Sets from MSigDB (https://www.gseamsigdb.org/gsea/msigdb/mouse/collections.jsp?targetSpeciesDB=Mouse#M5).

Data Availability

The PV-interneuron mass spectrometry proteomics data have been deposited to the ProteomeXchange Consortium via the PRIDE partner repository with the dataset identifier PXD053491. The 2020 mouse UniProt database (downloaded from https://www.uniprot.org/help/reference_proteome) was used for searches of mass spectrometry data. Source data are provided with this paper.

Project Name: Cortical region confers neuron-type-specific vulnerability to human APP expression

Project accession: PXD053491

1351 1 Braak, H. & Braak, E. Neuropathological stageing of Alzheimer-related changes. *Acta Neuropathol*
1352 **82**, 239-259, doi:10.1007/BF00308809 (1991).
1353 2 Gomez-Isla, T. *et al.* Profound loss of layer II entorhinal cortex neurons occurs in very mild
1354 Alzheimer's disease. *J Neurosci* **16**, 4491-4500, doi:10.1523/JNEUROSCI.16-14-04491.1996 (1996).
1355 3 Khan, U. A. *et al.* Molecular drivers and cortical spread of lateral entorhinal cortex dysfunction in
1356 preclinical Alzheimer's disease. *Nat Neurosci* **17**, 304-311, doi:10.1038/nn.3606 (2014).
1357 4 Kobro-Flatmoen, A., Nagelhus, A. & Witter, M. P. Reelin-immunoreactive neurons in entorhinal
1358 cortex layer II selectively express intracellular amyloid in early Alzheimer's disease. *Neurobiol Dis*
1359 **93**, 172-183, doi:10.1016/j.nbd.2016.05.012 (2016).
1360 5 Vossel, K. A. *et al.* Incidence and impact of subclinical epileptiform activity in Alzheimer's disease.
1361 *Ann Neurol* **80**, 858-870, doi:10.1002/ana.24794 (2016).
1362 6 Palop, J. J. *et al.* Aberrant excitatory neuronal activity and compensatory remodeling of inhibitory
1363 hippocampal circuits in mouse models of Alzheimer's disease. *Neuron* **55**, 697-711,
1364 doi:10.1016/j.neuron.2007.07.025 (2007).
1365 7 Verret, L. *et al.* Inhibitory interneuron deficit links altered network activity and cognitive
1366 dysfunction in Alzheimer model. *Cell* **149**, 708-721, doi:10.1016/j.cell.2012.02.046 (2012).
1367 8 Mondragon-Rodriguez, S., Gu, N., Manseau, F. & Williams, S. Alzheimer's Transgenic Model Is
1368 Characterized by Very Early Brain Network Alterations and beta-CTF Fragment Accumulation:
1369 Reversal by beta-Secretase Inhibition. *Front Cell Neurosci* **12**, 121, doi:10.3389/fncel.2018.00121
1370 (2018).
1371 9 Petrache, A. L. *et al.* Aberrant Excitatory-Inhibitory Synaptic Mechanisms in Entorhinal Cortex
1372 Microcircuits During the Pathogenesis of Alzheimer's Disease. *Cereb Cortex* **29**, 1834-1850,
1373 doi:10.1093/cercor/bhz016 (2019).
1374 10 Hijazi, S. *et al.* Early restoration of parvalbumin interneuron activity prevents memory loss and
1375 network hyperexcitability in a mouse model of Alzheimer's disease. *Mol Psychiatry* **25**, 3380-3398,
1376 doi:10.1038/s41380-019-0483-4 (2020).
1377 11 Johnson, E. C. B. *et al.* Behavioral and neural network abnormalities in human APP transgenic mice
1378 resemble those of App knock-in mice and are modulated by familial Alzheimer's disease mutations
1379 but not by inhibition of BACE1. *Mol Neurodegener* **15**, 53, doi:10.1186/s13024-020-00393-5
1380 (2020).
1381 12 Zhang, Z. *et al.* Hyper-excitability of corticothalamic PT neurons in mPFC promotes irritability in
1382 the mouse model of Alzheimer's disease. *Cell Rep* **41**, 111577, doi:10.1016/j.celrep.2022.111577
1383 (2022).
1384 13 Olah, V. J. *et al.* Biophysical K(v)3 channel alterations dampen excitability of cortical PV
1385 interneurons and contribute to network hyperexcitability in early Alzheimer's. *Elife* **11**,
1386 doi:10.7554/eLife.75316 (2022).
1387 14 Siskova, Z. *et al.* Dendritic structural degeneration is functionally linked to cellular
1388 hyperexcitability in a mouse model of Alzheimer's disease. *Neuron* **84**, 1023-1033,
1389 doi:10.1016/j.neuron.2014.10.024 (2014).
1390 15 Nuriel, T. *et al.* Neuronal hyperactivity due to loss of inhibitory tone in APOE4 mice lacking
1391 Alzheimer's disease-like pathology. *Nat Commun* **8**, 1464, doi:10.1038/s41467-017-01444-0
1392 (2017).
1393 16 Angulo, S. L. *et al.* Tau and amyloid-related pathologies in the entorhinal cortex have divergent
1394 effects in the hippocampal circuit. *Neurobiol Dis* **108**, 261-276, doi:10.1016/j.nbd.2017.08.015
1395 (2017).
1396 17 Nilssen, E. S. *et al.* Inhibitory Connectivity Dominates the Fan Cell Network in Layer II of Lateral
1397 Entorhinal Cortex. *J Neurosci* **38**, 9712-9727, doi:10.1523/JNEUROSCI.1290-18.2018 (2018).

18 Vormstein-Schneider, D. *et al.* Viral manipulation of functionally distinct interneurons in mice, non-human primates and humans. *Nat Neurosci* **23**, 1629-1636, doi:10.1038/s41593-020-0692-9 (2020).
19 Titlow, J. S. *et al.* Systematic analysis of YFP traps reveals common mRNA/protein discordance in neural tissues. *J Cell Biol* **222**, doi:10.1083/jcb.202205129 (2023).
20 Rayaprolu, S. *et al.* Cell type-specific biotin labeling in vivo resolves regional neuronal and astrocyte proteomic differences in mouse brain. *Nat Commun* **13**, 2927, doi:10.1038/s41467-022-30623-x (2022).
21 Kumar, P. *et al.* Native-state proteomics of Parvalbumin interneurons identifies unique molecular signatures and vulnerabilities to early Alzheimer's pathology. *Nat Commun* **15**, 2823, doi:10.1038/s41467-024-47028-7 (2024).
22 Yu, L. *et al.* Cortical Proteins Associated With Cognitive Resilience in Community-Dwelling Older Persons. *JAMA Psychiatry* **77**, 1172-1180, doi:10.1001/jamapsychiatry.2020.1807 (2020).
23 Mendonca, C. F. *et al.* Proteomic signatures of brain regions affected by tau pathology in early and late stages of Alzheimer's disease. *Neurobiol Dis* **130**, 104509, doi:10.1016/j.nbd.2019.104509 (2019).
24 Kavanagh, T., Halder, A. & Drummond, E. Tau interactome and RNA binding proteins in neurodegenerative diseases. *Mol Neurodegener* **17**, 66, doi:10.1186/s13024-022-00572-6 (2022).
25 Chen, C. *et al.* Early impairment of cortical circuit plasticity and connectivity in the 5XFAD Alzheimer's disease mouse model. *Transl Psychiatry* **12**, 371, doi:10.1038/s41398-022-02132-4 (2022).
26 Koo, E. H. *et al.* Differential expression of amyloid precursor protein mRNAs in cases of Alzheimer's disease and in aged nonhuman primates. *Neuron* **4**, 97-104, doi:10.1016/0896-6273(90)90446-m (1990).
27 Matsui, T. *et al.* Expression of APP pathway mRNAs and proteins in Alzheimer's disease. *Brain Res* **1161**, 116-123, doi:10.1016/j.brainres.2007.05.050 (2007).
28 Lehmann, L., Lo, A., Knox, K. M. & Barker-Haliski, M. Alzheimer's Disease and Epilepsy: A Perspective on the Opportunities for Overlapping Therapeutic Innovation. *Neurochem Res* **46**, 1895-1912, doi:10.1007/s11064-021-03332-y (2021).
29 Chen, L. *et al.* Progressive excitability changes in the medial entorhinal cortex in the 3xTg mouse model of Alzheimer's disease pathology. *bioRxiv*, doi:10.1101/2023.05.30.542838 (2023).
30 Tahvildari, B. & Alonso, A. Morphological and electrophysiological properties of lateral entorhinal cortex layers II and III principal neurons. *J Comp Neurol* **491**, 123-140, doi:10.1002/cne.20706 (2005).
31 Chen, L., Saito, T., Saido, T. C. & Mody, I. Novel Quantitative Analyses of Spontaneous Synaptic Events in Cortical Pyramidal Cells Reveal Subtle Parvalbumin-Expressing Interneuron Dysfunction in a Knock-In Mouse Model of Alzheimer's Disease. *eNeuro* **5**, doi:10.1523/ENEURO.0059-18.2018 (2018).
32 Varga, C., Lee, S. Y. & Soltesz, I. Target-selective GABAergic control of entorhinal cortex output. *Nat Neurosci* **13**, 822-824, doi:10.1038/nn.2570 (2010).
33 Gao, R. Interpreting the electrophysiological power spectrum. *J Neurophysiol* **115**, 628-630, doi:10.1152/jn.00722.2015 (2016).
34 Braak, H., Braak, E., Bohl, J. & Bratzke, H. Evolution of Alzheimer's disease related cortical lesions. *J Neural Transm Suppl* **54**, 97-106, doi:10.1007/978-3-7091-7508-8_9 (1998).
35 Desikan, R. S. *et al.* Amyloid-beta--associated clinical decline occurs only in the presence of elevated P-tau. *Arch Neurol* **69**, 709-713, doi:10.1001/archneurol.2011.3354 (2012).
36 Lue, L. F. *et al.* Soluble amyloid beta peptide concentration as a predictor of synaptic change in Alzheimer's disease. *Am J Pathol* **155**, 853-862, doi:10.1016/s0002-9440(10)65184-x (1999).

1446 37 Naslund, J. *et al.* Correlation between elevated levels of amyloid beta-peptide in the brain and
1447 cognitive decline. *JAMA* **283**, 1571-1577, doi:10.1001/jama.283.12.1571 (2000).
1448 38 Schultz, M. K., Jr. *et al.* Pharmacogenetic neuronal stimulation increases human tau pathology and
1449 trans-synaptic spread of tau to distal brain regions in mice. *Neurobiol Dis* **118**, 161-176,
1450 doi:10.1016/j.nbd.2018.07.003 (2018).
1451 39 Wu, J. W. *et al.* Neuronal activity enhances tau propagation and tau pathology in vivo. *Nat*
1452 *Neurosci* **19**, 1085-1092, doi:10.1038/nn.4328 (2016).
1453 40 Yamada, K. *et al.* Neuronal activity regulates extracellular tau in vivo. *J Exp Med* **211**, 387-393,
1454 doi:10.1084/jem.20131685 (2014).
1455 41 Busche, M. A. *et al.* Tau impairs neural circuits, dominating amyloid-beta effects, in Alzheimer
1456 models in vivo. *Nat Neurosci* **22**, 57-64, doi:10.1038/s41593-018-0289-8 (2019).
1457 42 Minkeviciene, R. *et al.* Amyloid beta-induced neuronal hyperexcitability triggers progressive
1458 epilepsy. *J Neurosci* **29**, 3453-3462, doi:10.1523/JNEUROSCI.5215-08.2009 (2009).
1459 43 Hall, A. M. *et al.* Tau-dependent Kv4.2 depletion and dendritic hyperexcitability in a mouse model
1460 of Alzheimer's disease. *J Neurosci* **35**, 6221-6230, doi:10.1523/JNEUROSCI.2552-14.2015 (2015).
1461 44 Colom-Cadena, M. *et al.* Synaptic oligomeric tau in Alzheimer's disease - A potential culprit in the
1462 spread of tau pathology through the brain. *Neuron* **111**, 2170-2183 e2176,
1463 doi:10.1016/j.neuron.2023.04.020 (2023).
1464 45 Nassar, M. *et al.* Diversity and overlap of parvalbumin and somatostatin expressing interneurons
1465 in mouse presubiculum. *Front Neural Circuits* **9**, 20, doi:10.3389/fncir.2015.00020 (2015).
1466 46 Munoz-Manchado, A. B. *et al.* Diversity of Interneurons in the Dorsal Striatum Revealed by Single-
1467 Cell RNA Sequencing and PatchSeq. *Cell Rep* **24**, 2179-2190 e2177,
1468 doi:10.1016/j.celrep.2018.07.053 (2018).
1469 47 Ekins, T. G. *et al.* Emergence of non-canonical parvalbumin-containing interneurons in
1470 hippocampus of a murine model of type I lissencephaly. *Elife* **9**, doi:10.7554/eLife.62373 (2020).
1471 48 Huang, Y. A., Zhou, B., Wernig, M. & Sudhof, T. C. ApoE2, ApoE3, and ApoE4 Differentially
1472 Stimulate APP Transcription and Abeta Secretion. *Cell* **168**, 427-441 e421,
1473 doi:10.1016/j.cell.2016.12.044 (2017).
1474 49 Lee, S. I. *et al.* APOE4-carrying human astrocytes oversupply cholesterol to promote neuronal lipid
1475 raft expansion and Abeta generation. *Stem Cell Reports* **16**, 2128-2137,
1476 doi:10.1016/j.stemcr.2021.07.017 (2021).
1477 50 Thakur, M. K. & Mani, S. T. Estradiol regulates APP mRNA alternative splicing in the mice brain
1478 cortex. *Neurosci Lett* **381**, 154-157, doi:10.1016/j.neulet.2005.02.014 (2005).
1479 51 Bjelik, A. *et al.* Human apoB overexpression and a high-cholesterol diet differently modify the
1480 brain APP metabolism in the transgenic mouse model of atherosclerosis. *Neurochem Int* **49**, 393-
1481 400, doi:10.1016/j.neuint.2006.01.026 (2006).
1482 52 Bjelik, A. *et al.* APP mRNA splicing is upregulated in the brain of biglycan transgenic mice.
1483 *Neurochem Int* **50**, 1-4, doi:10.1016/j.neuint.2006.07.009 (2007).
1484 53 Dubal, D. B., Broestl, L. & Worden, K. Sex and gonadal hormones in mouse models of Alzheimer's
1485 disease: what is relevant to the human condition? *Biol Sex Differ* **3**, 24, doi:10.1186/2042-6410-3-
1486 24 (2012).
1487 54 Notkola, I. L. *et al.* Serum total cholesterol, apolipoprotein E epsilon 4 allele, and Alzheimer's
1488 disease. *Neuroepidemiology* **17**, 14-20, doi:10.1159/000026149 (1998).
1489 55 Kivipelto, M. *et al.* Apolipoprotein E epsilon4 allele, elevated midlife total cholesterol level, and
1490 high midlife systolic blood pressure are independent risk factors for late-life Alzheimer disease.
1491 *Ann Intern Med* **137**, 149-155, doi:10.7326/0003-4819-137-3-200208060-00006 (2002).

1492 56 Honig, L. S., Kukull, W. & Mayeux, R. Atherosclerosis and AD: analysis of data from the US National
1493 Alzheimer's Coordinating Center. *Neurology* **64**, 494-500,
1494 doi:10.1212/01.WNL.0000150886.50187.30 (2005).
1495 57 Wang, J. *et al.* Enhanced Gamma Activity and Cross-Frequency Interaction of Resting-State
1496 Electroencephalographic Oscillations in Patients with Alzheimer's Disease. *Front Aging Neurosci*
1497 **9**, 243, doi:10.3389/fnagi.2017.00243 (2017).
1498 58 Saito, T. *et al.* Single App knock-in mouse models of Alzheimer's disease. *Nat Neurosci* **17**, 661-
1499 663, doi:10.1038/nn.3697 (2014).
1500 59 Baglietto-Vargas, D. *et al.* Generation of a humanized Abeta expressing mouse demonstrating
1501 aspects of Alzheimer's disease-like pathology. *Nat Commun* **12**, 2421, doi:10.1038/s41467-021-
1502 22624-z (2021).
1503 60 Mucke, L. *et al.* High-level neuronal expression of abeta 1-42 in wild-type human amyloid protein
1504 precursor transgenic mice: synaptotoxicity without plaque formation. *J Neurosci* **20**, 4050-4058,
1505 doi:10.1523/JNEUROSCI.20-11-04050.2000 (2000).
1506 61 Mehr, A. *et al.* Lack of APP and APLP2 in GABAergic Forebrain Neurons Impairs Synaptic Plasticity
1507 and Cognition. *Cereb Cortex* **30**, 4044-4063, doi:10.1093/cercor/bhaa025 (2020).
1508 62 Yamamoto, K., Yamamoto, R. & Kato, N. Amyloid beta and Amyloid Precursor Protein
1509 Synergistically Suppress Large-Conductance Calcium-Activated Potassium Channel in Cortical
1510 Neurons. *Front Aging Neurosci* **13**, 660319, doi:10.3389/fnagi.2021.660319 (2021).
1511 63 Agsten, M. *et al.* BACE1 modulates gating of KCNQ1 (Kv7.1) and cardiac delayed rectifier
1512 KCNQ1/KCNE1 (IKs). *J Mol Cell Cardiol* **89**, 335-348, doi:10.1016/j.yjmcc.2015.10.006 (2015).
1513 64 Lehnert, S. *et al.* Ion channel regulation by beta-secretase BACE1 - enzymatic and non-enzymatic
1514 effects beyond Alzheimer's disease. *Channels (Austin)* **10**, 365-378,
1515 doi:10.1080/19336950.2016.1196307 (2016).
1516 65 Wong, H. K. *et al.* beta Subunits of voltage-gated sodium channels are novel substrates of beta-
1517 site amyloid precursor protein-cleaving enzyme (BACE1) and gamma-secretase. *J Biol Chem* **280**,
1518 23009-23017, doi:10.1074/jbc.M414648200 (2005).
1519 66 Manville, R. W. & Abbott, G. W. The Amyloid Precursor Protein C99 Fragment Modulates Voltage-
1520 Gated Potassium Channels. *Cell Physiol Biochem* **55**, 157-170, doi:10.33594/000000397 (2021).
1521 67 Furukawa, K., Barger, S. W., Blalock, E. M. & Mattson, M. P. Activation of K+ channels and
1522 suppression of neuronal activity by secreted beta-amyloid-precursor protein. *Nature* **379**, 74-78,
1523 doi:10.1038/379074a0 (1996).
1524 68 Mayordomo-Cava, J., Yajeya, J., Navarro-Lopez, J. D. & Jimenez-Diaz, L. Amyloid-beta(25-35)
1525 Modulates the Expression of GirK and KCNQ Channel Genes in the Hippocampus. *PLoS One* **10**,
1526 e0134385, doi:10.1371/journal.pone.0134385 (2015).
1527 69 Sepulveda, F. J., Parodi, J., Peoples, R. W., Opazo, C. & Aguayo, L. G. Synaptotoxicity of Alzheimer
1528 beta amyloid can be explained by its membrane perforating property. *PLoS One* **5**, e11820,
1529 doi:10.1371/journal.pone.0011820 (2010).
1530 70 Harris, J. A. *et al.* Human P301L-mutant tau expression in mouse entorhinal-hippocampal network
1531 causes tau aggregation and presynaptic pathology but no cognitive deficits. *PLoS One* **7**, e45881,
1532 doi:10.1371/journal.pone.0045881 (2012).
1533 71 Pickett, E. K. *et al.* Spread of tau down neural circuits precedes synapse and neuronal loss in the
1534 rTgTauEC mouse model of early Alzheimer's disease. *Synapse* **71**, doi:10.1002/syn.21965 (2017).
1535 72 Cope, Z. A., Murai, T. & Sukoff Rizzo, S. J. Emerging Electroencephalographic Biomarkers to
1536 Improve Preclinical to Clinical Translation in Alzheimer's Disease. *Front Aging Neurosci* **14**,
1537 805063, doi:10.3389/fnagi.2022.805063 (2022).

1538 73 Kelberman, M. A. *et al.* Age-dependent dysregulation of locus coeruleus firing in a transgenic rat
1539 model of Alzheimer's disease. *Neurobiol Aging* **125**, 98-108,
1540 doi:10.1016/j.neurobiolaging.2023.01.016 (2023).
1541 74 Caccavano, A. *et al.* Inhibitory Parvalbumin Basket Cell Activity is Selectively Reduced during
1542 Hippocampal Sharp Wave Ripples in a Mouse Model of Familial Alzheimer's Disease. *J Neurosci*
1543 **40**, 5116-5136, doi:10.1523/JNEUROSCI.0425-20.2020 (2020).
1544 75 Rodriguez, G. A., Barrett, G. M., Duff, K. E. & Hussaini, S. A. Chemogenetic attenuation of neuronal
1545 activity in the entorhinal cortex reduces Abeta and tau pathology in the hippocampus. *PLoS Biol*
1546 **18**, e3000851, doi:10.1371/journal.pbio.3000851 (2020).
1547 76 Bero, A. W. *et al.* Neuronal activity regulates the regional vulnerability to amyloid-beta deposition.
1548 *Nat Neurosci* **14**, 750-756, doi:10.1038/nn.2801 (2011).
1549 77 Olney, J. W. Brain lesions, obesity, and other disturbances in mice treated with monosodium
1550 glutamate. *Science* **164**, 719-721, doi:10.1126/science.164.3880.719 (1969).
1551 78 Taylor, A. L. What we talk about when we talk about capacitance measured with the voltage-
1552 clamp step method. *J Comput Neurosci* **32**, 167-175, doi:10.1007/s10827-011-0346-8 (2012).
1553 79 Pelkey, K. A. *et al.* Evolutionary conservation of hippocampal mossy fiber synapse properties.
1554 *Neuron* **111**, 3802-3818 e3805, doi:10.1016/j.neuron.2023.09.005 (2023).
1555 80 Chan, K. Y. *et al.* Engineered AAVs for efficient noninvasive gene delivery to the central and
1556 peripheral nervous systems. *Nat Neurosci* **20**, 1172-1179, doi:10.1038/nn.4593 (2017).
1557 81 Johnson, E. C. B. *et al.* Large-scale deep multi-layer analysis of Alzheimer's disease brain reveals
1558 strong proteomic disease-related changes not observed at the RNA level. *Nat Neurosci* **25**, 213-
1559 225, doi:10.1038/s41593-021-00999-y (2022).
1560 82 Rangaraju, S. *et al.* Quantitative proteomics of acutely-isolated mouse microglia identifies novel
1561 immune Alzheimer's disease-related proteins. *Mol Neurodegener* **13**, 34, doi:10.1186/s13024-
1562 018-0266-4 (2018).
1563 83 Rayaprolu, S. *et al.* Flow-cytometric microglial sorting coupled with quantitative proteomics
1564 identifies moesin as a highly-abundant microglial protein with relevance to Alzheimer's disease.
1565 *Mol Neurodegener* **15**, 28, doi:10.1186/s13024-020-00377-5 (2020).
1566 84 Perez-Riverol, Y. *et al.* The PRIDE database resources in 2022: a hub for mass spectrometry-based
1567 proteomics evidences. *Nucleic Acids Res* **50**, D543-D552, doi:10.1093/nar/gkab1038 (2022).
1568 85 Galea, E. *et al.* Multi-transcriptomic analysis points to early organelle dysfunction in human
1569 astrocytes in Alzheimer's disease. *Neurobiol Dis* **166**, 105655, doi:10.1016/j.nbd.2022.105655
1570 (2022).
1571 86 Hanzelmann, S., Castelo, R. & Guinney, J. GSVA: gene set variation analysis for microarray and
1572 RNA-seq data. *BMC Bioinformatics* **14**, 7, doi:10.1186/1471-2105-14-7 (2013).

1573

1574 **Acknowledgements**

1575 Contributions:

1576 Conceptualization: AMG, MJR

1577 Methodology and investigation: AMG, EB, PK, KEM, VJO, KS, CCR, AE, DD, NTS, SR, DW,
1578 MJR

1579 Writing-Original draft: AMG, MJR

1580 Writing-Review and Editing: MJR, AMG, SR, DW, CF

Funding acquisition: MJR, SR, AMG, EB

Resources: MJR, NTS, SR

Conflicts of interest/Disclosures

Authors report no financial disclosures or conflicts of interest.

Funding: MJR: R56AG072473, RF1AG079269, R21NS133960, Emory ADRC grant 00100569. SR: R01 NS114130, RF1 AG071587, R01 AG075820. CF: RF1AG079269. NTS: U01AG061357, RF1 AG071587 and R01 AG075820. AMG: F31AG076289. EB: F31AG086006

Table 1

Principal cells in LEC and SS Ctx

Features	Average±SEM LEC EXC	Average±SEM SS Ctx EXC	p-value	t-value	Degrees of Freedom
AHP (mV)	9.66±0.75	6.33±0.64	<0.01	3.41	40
Threshold (mV)	-41.97±1.18	-44.61±1.26	0.14	1.53	40
dV/dt Max	353.40±13.97	469.60±31.50	<0.01	3.37	40
Input Resistance (MΩ)	103.60±14.51	117.80±8.93	0.40	0.86	40
Resting Membrane Potential (mV)	-63.39±1.18	-71.31±1.50	<0.01	4.00	40
Membrane Capacitance (pF)	205.40±14.68	183.30±12.73	0.26	1.14	40
Membrane Tau (ms)	19.65±1.84	20.64±1.74	0.70	0.39	40
Accomodation Ratio	2.52±0.47	2.93±0.28	0.45	0.77	40

All were Unpaired t-tests, Two-tailed

PV Interneurons in LEC and SS Ctx

Features	Average±SEM LEC PV-IN	Average±SEM SS Ctx PV-IN	p-value	t-value	Degrees of Freedom
AHP (mV)	20.68±1.01	19.47±1.19	0.44	0.78	25
Threshold (mV)	-40.02±1.14	-46.14±0.55	<0.01	2.47	25
dV/dt Max	553.70±29.76	571.60±20.48	0.65	0.46	25
Input Resistance (MΩ)	147.30±16.44	121.20±17.14	0.29	1.08	25
Resting Membrane Potential (mV)	-60.38±1.60	-65.71±1.89	0.04	3.15	25
Membrane Capacitance (pF)	70.17±5.46	71.91±9.51	0.87	0.17	25
Membrane Tau (ms)	9.98±0.62	7.39±0.47	<0.01	3.181	25
Accomodation Ratio	2.14±0.24	1.71±0.09	0.154	1.470	25

All were Unpaired t-tests, Two-tailed

Extended Data Table 1. Passive and active properties of LEC and SS Ctx neurons

Passive and active properties of principal excitatory cells (top) or tdTom+ PV interneurons (bottom) in L2 LEC and L5 SS Ctx.

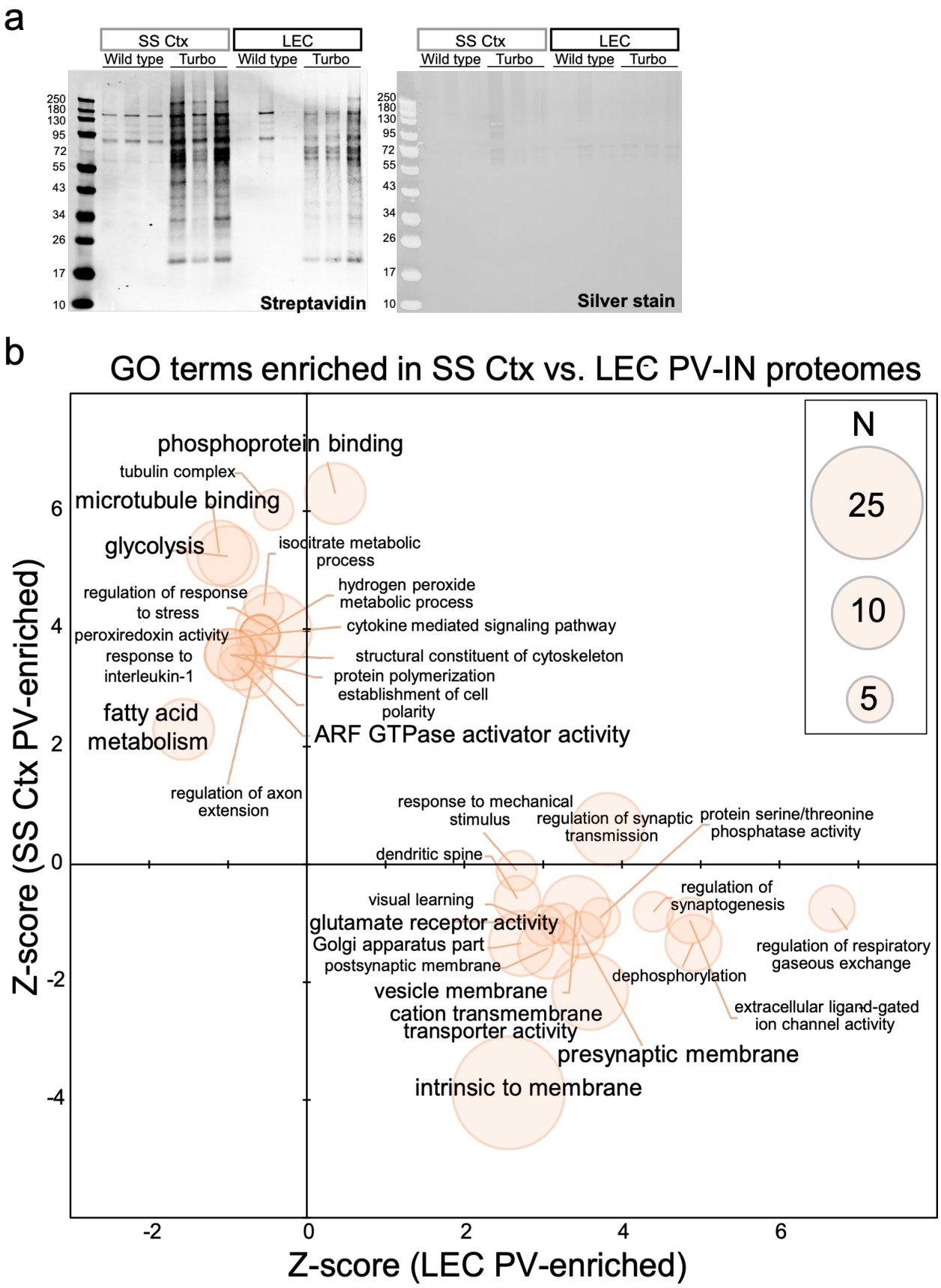
a
SS Ctx
LEC
Wild type
Turbo
Wild type
Turbo
250
180
130
95
72
55
43
34
26
17
10
Streptavidin
Silver stain
b
GO terms enriched in SS Ctx vs. LEC PV-IN proteomes
N
25
10
5
phosphoprotein binding
tubulin complex
microtubule binding
glycolysis
isocitrate metabolic process
hydrogen peroxide metabolic process
regulation of response to stress
cytokine mediated signaling pathway
peroxiredoxin activity
response to interleukin-1
structural constituent of cytoskeleton
protein polymerization
establishment of cell polarity
fatty acid metabolism
ARF GTPase activator activity
regulation of axon extension
response to mechanical stimulus
regulation of synaptic transmission
protein serine/threonine phosphatase activity
dendritic spine
regulation of synaptogenesis
visual learning
glutamate receptor activity
Golgi apparatus part
regulation of respiratory gaseous exchange
postsynaptic membrane
dephosphorylation
vesicle membrane
extracellular ligand-gated ion channel activity
cation transmembrane transporter activity
presynaptic membrane
intrinsic to membrane
Z-score (SS Ctx PV-enriched)
Z-score (LEC PV-enriched)
6
4
2
0
-2
-4
-2
0
2
4
6

1597

1598 **Extended Data Figure 1. Enriched biotinylated PV-interneuron proteins from the SS Ctx**
1599 **and LEC are neuron-specific**
1600 **a.** Western blot (left) and silver stain (right) visualization of enriched biotinylated proteins in PV-
1601 interneurons (IN) from the SS Ctx and LEC after streptavidin-pulldown and elution of biotinylated
1602 proteins from a 10% aliquot of beads.
1603 **b.** GSEA of [3] 2-fold enriched biotinylated PV-interneuron proteins from the SS Ctx and LEC from
1604 PV-CIBOP mice, as compared to a reference protein list of both regions (n = 807) showed
1605 enrichment of synaptic and neuronal proteins confirming neuronal labeling. The orange dot size
1606 represents the number of gene symbols represented in each GO term. WT (Control) or
1607 Rosa26TurboID/wt (PV-CIBOP) mice (n=3 per genotype, including males and females).
1608
1609
1610
1611

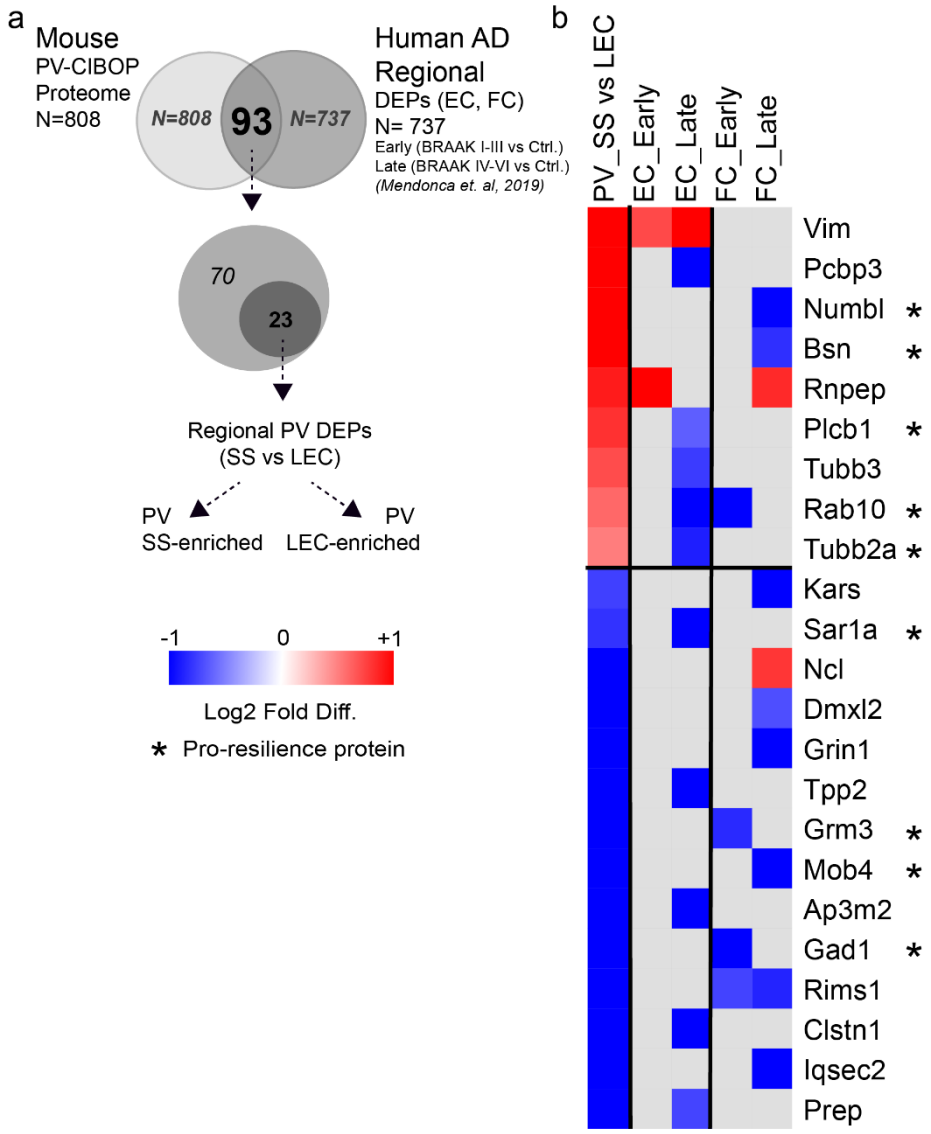

Extended Data Figure 2. PV-CIBOP regional proteins that also demonstrate region-specific changes in human AD brain (related to Figure 1).

a. Mouse PV-CIBOP regional proteins (SS Ctx vs. LEC) that were also identified as regional DEPs (AD vs. Ctrl) from human post-mortem brain regions (EC and FC)[23]. (EC: Entorhinal Cortex; FC: Frontal Cortex; Early: Braak I-III vs. Ctrl; Late: Braak IV-VI vs. Ctrl).

See also Extended Data Datasheet 2 for related data and analyses.

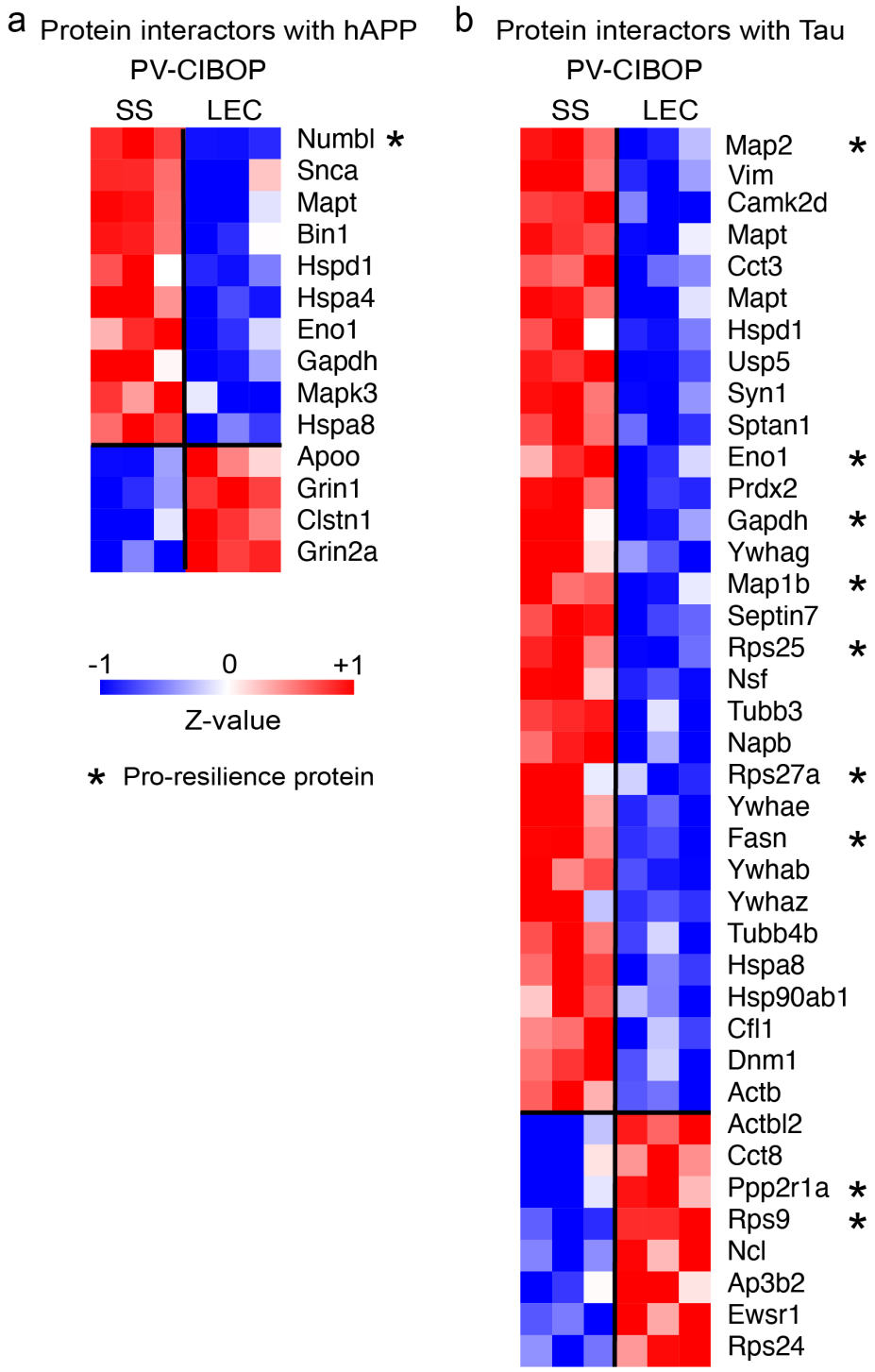

Extended Data Figure 3. PV-CIBOP identified regional proteins with known interactions with human APP and Tau (Related to Figure 1).

a. Heatmap representation of PV regional DEPs (SS Ctx vs. LEC) that are known protein-protein interactors with human APP (from 243 known APP interactors derived from the STRING database). Proteins marked with * indicate those that are also known pro-resilience proteins. As

expected, the APP interactors were enriched in proteins involved in lipid binding, amyloid beta processing, cholesterol metabolism, and complement and coagulation cascade.

b. Heatmap representation of PV interneuron regional DEPs (SS Ctx vs. LEC) that are known protein-protein interactors with Tau from human brain. Proteins marked with * indicate those that are also known pro-resilience proteins.

Also see Extended Data Datasheets 3 and 4 for related results and analyses.

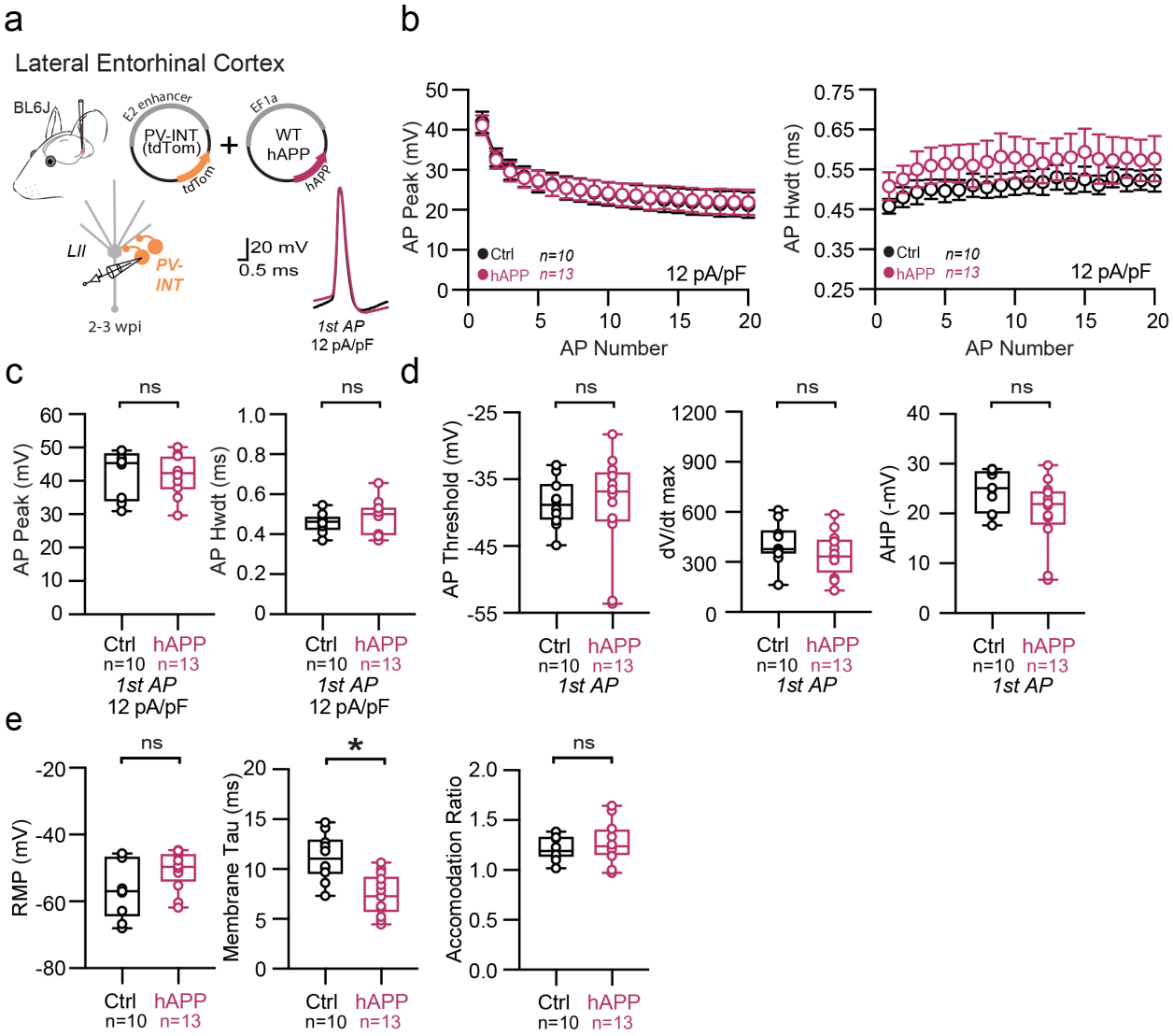

Extended Data Figure 4. Passive and active properties of LEC PV interneurons after hAPP injection

a. Graphical summary of AAV.E2.tdTom and AAV.EF1a.hAPP (or for Ctrl, saline) stereotactic injection in the Lateral Entorhinal Cortex. tdTom+ PV interneurons were fluorescently targeted

for whole-cell current-clamp recordings. AP waveforms of tdTom+ PV interneurons were compared at 12 pA/pF square pulse injections in WT mice from Ctrl and hAPP injected. Aps from the 1st spike in the train are superimposed for comparison.

b. Relationship between AP peak ($p=0.88$, $df=21$) or width ($p<0.0001$, $df=21$) in WT mice and AP # during spike trains elicited with a 12 pA/pF current injection.

c. Summary data of AP properties. LEC PV interneurons after hAPP injection 1st AP peak ($p=0.94$, $t=0.08$) and half-width remains unchanged ($p=0.51$, $t=0.67$, $df=21$).

d. Summary data of AP properties. LEC PV interneurons after hAPP injection AP threshold ($p=0.85$, $t=0.20$), dV/dt max ($p=0.12$, $t=1.6$), and AHP (0.63, $t=0.49$) ($df=21$) remained unchanged.

e. Summary data of AP properties. LEC PV interneurons after hAPP injection show unchanged Resting Membrane Potential ($p=0.09$, $t=1.79$) and Accomodation Ratio ($p=0.66$, $t=0.44$), but a reduction in Membrane Tau($p=0.0008$, $t=3.93$) ($df=21$).

For all summary graphs, data are expressed as mean (± SEM). For **b**: Statistical significance is denoted as *=$p<0.05$, as determined by Two-way ANOVA with Sidak's multiple comparison test. For c, d, e: Individual data points and box plots are displayed. Statistical significance is denoted as *=$p<0.05$, as determined by two-tailed unpaired t-test.

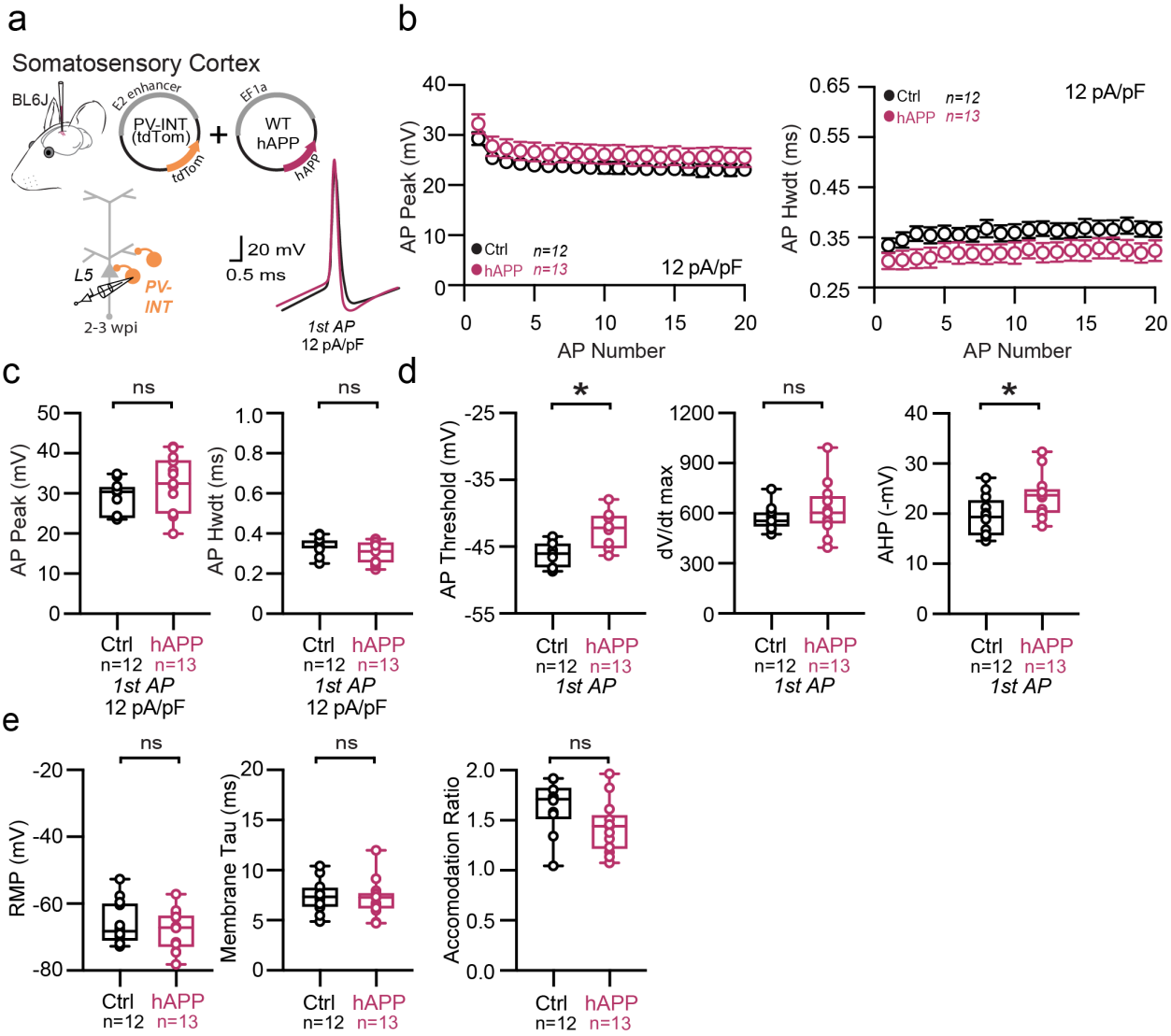

Extended Data Figure 5. Passive and active properties of SS Ctx interneurons after hAPP injection

a. Graphical summary of AAV.E2.tdTom and AAV.EF1a.hAPP (or for Ctrl, saline) stereotactic injection in the SS Cortex. tdTom+ PV interneurons were fluorescently targeted for whole-cell current-clamp recordings. AP waveforms of tdTom+ PV interneurons were compared at 12 pA/pF square pulse injections in WT mice from Ctrl and hAPP injected. Aps from the 1st spike in the train are superimposed for comparison.

b. Relationship between AP peak (p=0.17, t=1.42 df=23) or width (p=0.15, t=1.49 df=23) for in WT mice and AP # during spike trains elicited with a 12 pA/pF current injection.

c. Summary data of AP properties. SS PV interneurons after hAPP injection 1st AP peak (p=0.17, t=1.42) and half-width (p=0.15, t=1.49) (df=23) remain unchanged.

d. Summary data of AP properties. SS PV interneurons after hAPP injection dV/dt max remains unchanged ($p=0.32$, $t=1.01$). AP Threshold ($p=0.001$, $t=3.84$) and AHP ($p=0.02$, $t=2.42$)($df=23$) significantly increase after hAPP injection.

e. Summary data of AP properties. SS PV interneurons after hAPP injection show unchanged Resting Membrane Potential ($p=0.40$, $t=0.85$), Accomodation Ratio ($p=0.08$, $t=1.84$), and Membrane Tau ($p=0.81$, $t=0.24$) ($df=23$).

For all summary graphs, data are expressed as mean (± SEM). For **b**: Statistical significance is denoted as *=$p<0.05$, as determined by Two-way ANOVA with Sidak's multiple comparison test. For c, d, e: Individual data points and box plots are displayed. Statistical significance is denoted as *=$p<0.05$, as determined by two-tailed unpaired t-test.

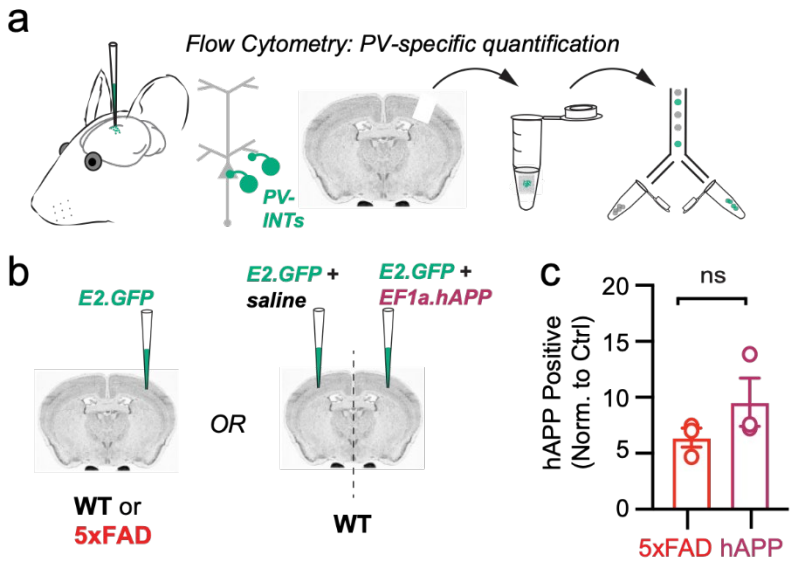

Extended Data Figure 6. Confirmation of hAPP protein in PV interneurons using PV-specific flow cytometry

a. Graphical summary of PV-specific flow cytometry workflow. Region containing fluorescent PV interneurons after AAV.E2.GFP stereotactic injection in the SS Cortex was microdissected, triturated, and sorted based on GFP+ signal. Subsequent confirmation specifically for human APP was completed.

b. WT and 5xFAD mice (~ 2 months) were injected with AAV.E2.GFP and sorted using flow cytometry. WT mice were also used to compare AAV.E2.GFP + EF1a.hAPP injected SS Ctx to the contralateral hemisphere where EF1a was replaced with an equal volume of saline.

c. Both groups were normalized to their control groups (WT littermates for 5xFAD; contralateral hemi for the hAPP control). The number hAPP expressing PV-interneurons did not significantly differ between 5xFAD and hAPP injected ($p=0.24$, $t=1.37$, $df=4$).

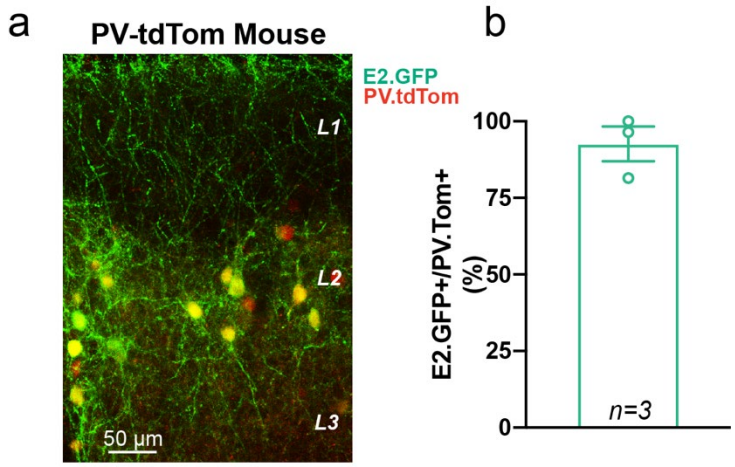

1713

1714

1715 **Extended Data Figure 7. Specificity of AAV.pHP-eB.E2.GFP in the Lateral Entorhinal**
1716 **Cortex for stereotactic and retro-orbital injections**

1717 **a.** Stereotactic injection of AAV.pHP-eB.E2.GFP into the LEC of a PV-tdTom transgenic mouse.
1718 **b.** For three animals, three slices were analyzed for E2.GFP+ cells which were also PV.tdTom+
1719 (Mean: 92.62 ± 5.7% for three biological replicates).

1720

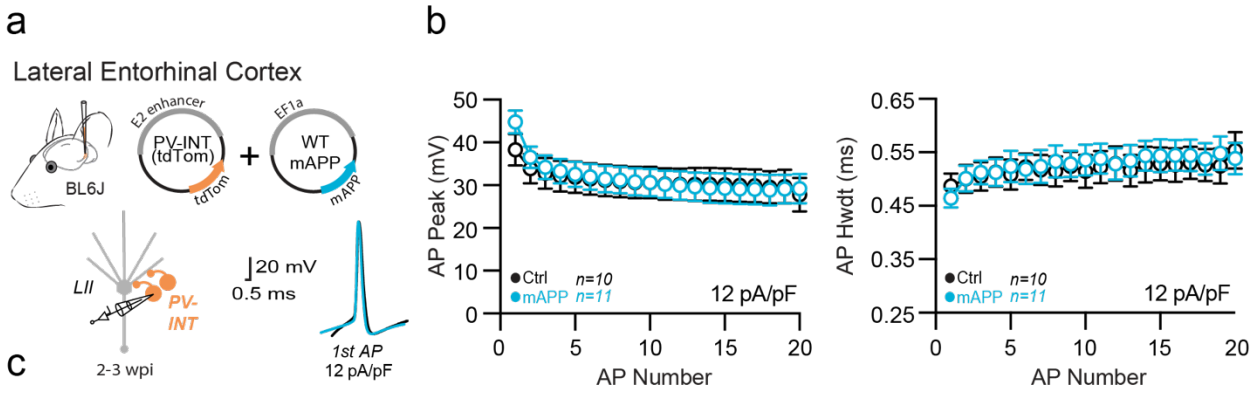

c

Features	Average±SEM Ctrl PV	Average±SEM mAPP PV	p-value	t-value	Degrees of Freedom
AHP (mV)	23.88±0.98	20.96±1.07	0.06	2.01	19
Threshold (mV)	-43.80±1.82	-42.68±1.68	0.66	0.45	19
dV/dt Max	494.30±30.21	567.00±28.11	0.09	1.76	19
Input Resistance (MΩ)	111.90±15.59	149.20±17.96	0.14	1.53	19
Resting Membrane Potential (mV)	-59.41±2.33	-63.80±1.27	0.12	1.66	19
Membrane Capacitance (pF)	71.04±7.65	71.02±6.67	0.99	0.002	19
Membrane Tau (ms)	8.78±0.60	10.52±0.91	0.15	1.52	19
Accomodation Ratio	1.67±0.23	2.14±0.22	0.17	1.43	19

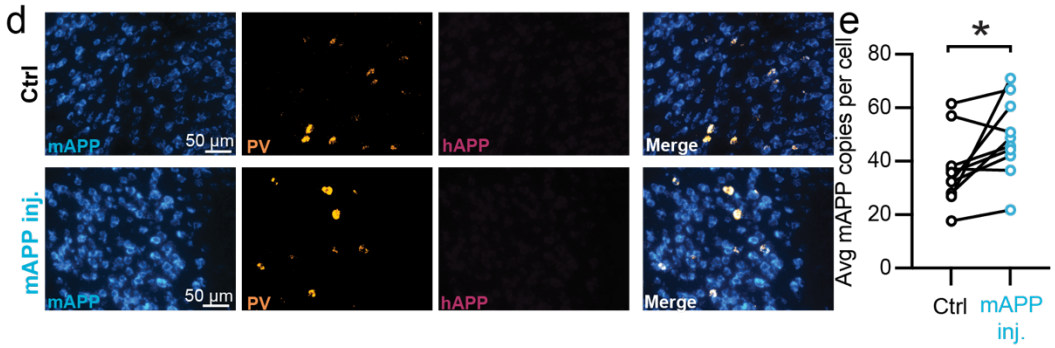

Extended Data Figure 8. Passive and active properties of LEC PV interneurons after mAPP injection

a. Graphical summary of AAV.E2.tdTom and AAV.EF1a.mAPP (or for Ctrl, saline) stereotactic injection in the SS Cortex. tdTom+ PV interneurons were fluorescently targeted for whole-cell current-clamp recordings. AP waveforms of tdTom+ PV interneurons were compared at 12 pA/pF

1727 square pulse injections in WT mice from Ctrl and mAPP injected. Aps from the 1st spike in the
1728 train are superimposed for comparison.
1729 **b.** Relationship between AP peak (p=0.61) or width (p=0.35) in WT mice and AP # during spike
1730 trains elicited with a 12 pA/pF current injection.
1731 **c.** Summary table of AP properties.
1732 d. RNAscope representative images at 40x magnification for Ctrl (top) and mAPP (bottom)
1733 injected mice: mAPP mRNA (cyan), Parvalbumin mRNA (gold), human APP mRNA (magenta),
1734 and a final merged image.
1735 **e.** RNAscope quantification for mAPP copies per DAPI+ cell comparing mAPP injected to the
1736 contralateral hemisphere endogenous mAPP expression. mAPP injected show a significant
1737 increase in mAPP copies in the injected hemisphere (p=0.03, t=2.57, df=9; two-tailed paired t-
1738 test).
1739
1740 For all summary graphs, data are expressed as mean (± SEM). For **b**: Statistical significance is
1741 denoted as *=p<0.05, as determined by Two-way ANOVA with Sidak's multiple comparison test.
1742 For c, e: statistical significance is denoted as *=p<0.05, as determined by two-tailed unpaired t-
1743 test.
1744
1745
1746
1747
1748
1749
1750
1751
1752

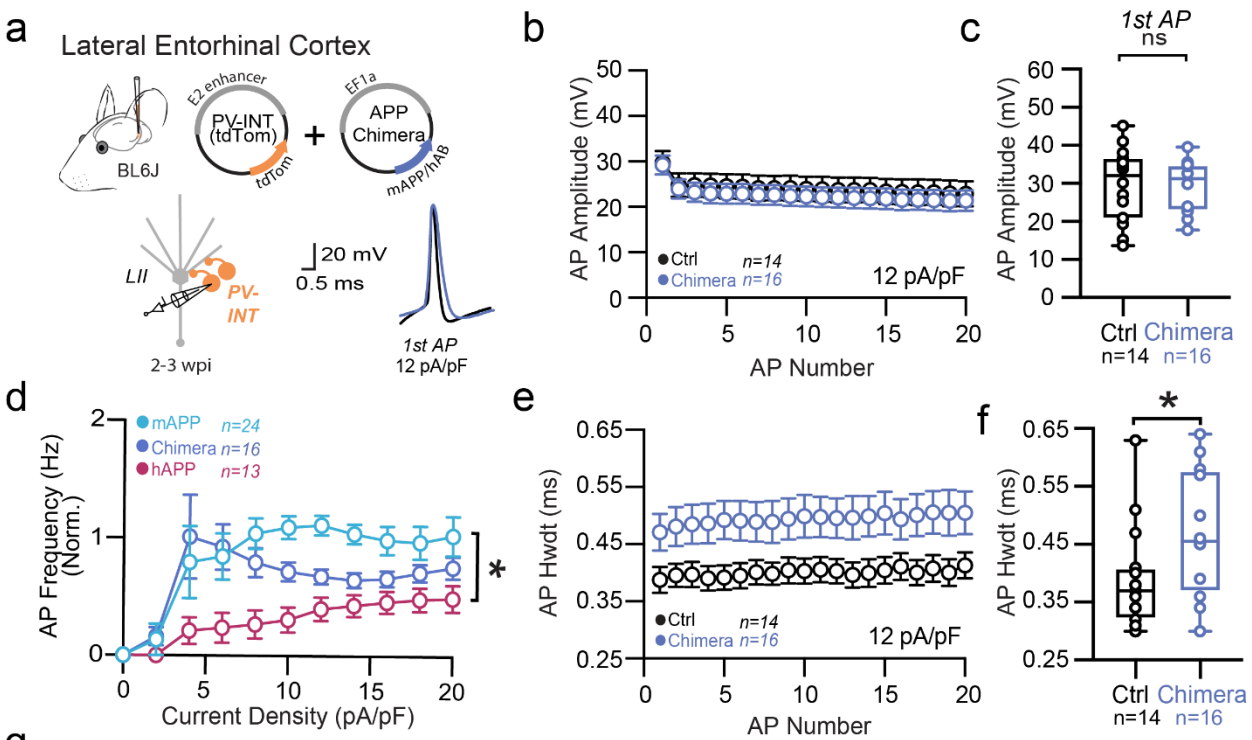

g

Features	Average±SEM Ctrl	Average±SEM APP Chimera	p-value	t-value	Degrees of Freedom
AHP (mV)	24.54±1.16	23.21±0.97	0.39	0.88	29
Threshold (mV)	-44.17±1.53	-43.29±1.08	0.64	0.48	29
dV/dt Max	518.10±40.35	456.00±36.29	0.26	1.15	29
Input Resistance (MΩ)	141.50±12.70	156.30±23.50	0.60	0.50	29
Resting Membrane Potential (mV)	-69.38±1.38	-70.57±2.06	0.65	0.47	29
Membrane Capacitance (pF)	66.96±8.06	72.59±4.21	0.53	0.64	29
Membrane Tau (ms)	8.28±0.70	10.29±1.12	0.15	1.47	29

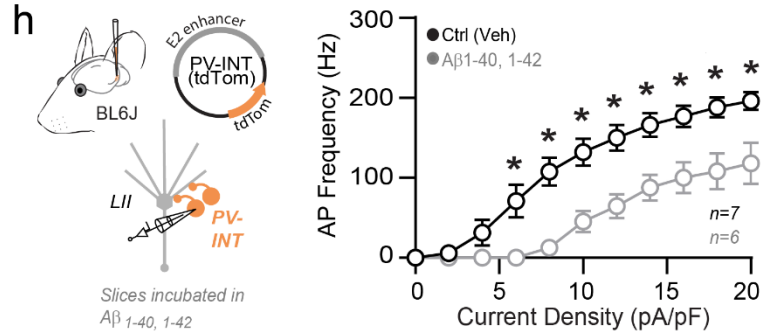

1753

1754 **Extended Data Figure 9. Passive and active properties of LEC PV interneurons after**
1755 **mAPP/hAB Chimera injection**
1756 **a.** Graphical summary of AAV.E2.tdTom and AAV.EF1a.mAPP/hAB Chimera (or for Ctrl,
1757 saline) stereotactic injection in the SS Cortex. tdTom+ PV interneurons were fluorescently targeted
1758 for whole-cell current-clamp recordings. AP waveforms of tdTom+ PV interneurons were
1759 compared at 12 pA/pF square pulse injections in WT mice from Ctrl and mAPP injected. Aps from
1760 the 1st spike in the train are superimposed for comparison.
1761 **b.** Relationship between AP peak (b) or width (e) in WT mice and AP # during spike trains elicited
1762 with a 12 pA/pF current injection.
1763 **c.** Summary data of AP properties. LEC PV cells after Chimera injection 1st AP peak (29.74 ± 2.61
1764 mV, 29.18 ± 2.08 mV, hAPP and Ctrl respectively, p=0.87, t=0.17, df=24) remains unchanged.
1765 **d.** Group data summary of AP firing frequency in L2 LEC from mAPP injected (blue), Chimera
1766 injected (purple), and hAPP injected mice (magenta), all normalized to their dataset controls.
1767 **e.** Relationship between AP width in WT mice and AP # during spike trains elicited with a 12
1768 pA/pF current injection.
1769 **f.** AP half-width displays a significant increase in the chimera group (0.39± 0.02 ms, 4.80 ± 0.03
1770 ms, hAPP and Ctrl respectively, p=0.04, t=2.14, df=24).
1771 **g.** Summary table of effects of the mAPP/hAβ chimera.
1772 **h**. Summary of AP firing frequency in L2 PV interneurons from LEC Aβ incubated slices and
1773 vehicle controls.
1774
1775 For all summary graphs, data are expressed as mean (± SEM). For c, f, g: statistical significance
1776 is denoted as *=p<0.05, as determined by two-tailed unpaired t-test.
1777
1778

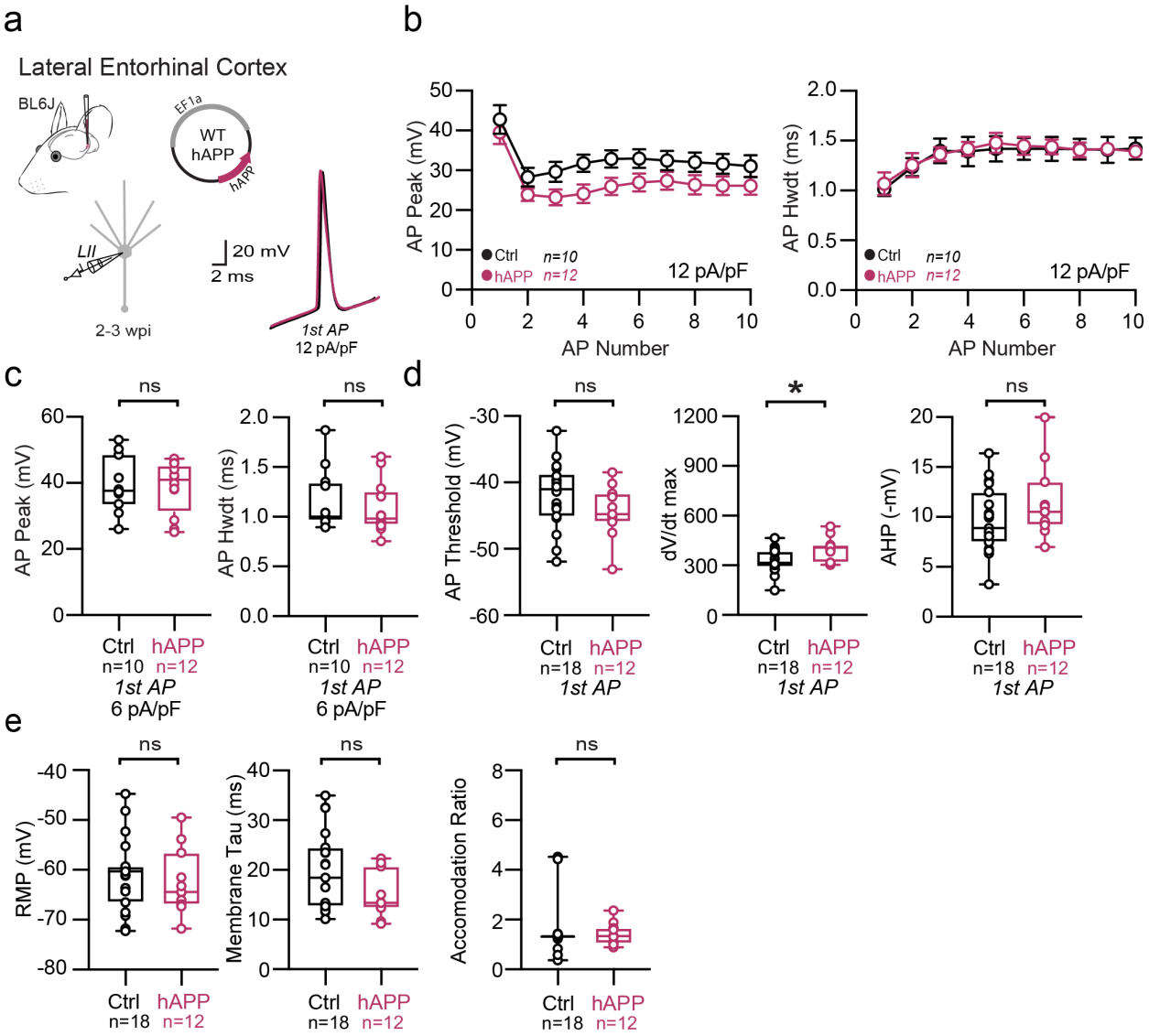

Extended Data Figure 10. Passive and active properties of LEC excitatory neurons after hAPP injection

a. Graphical summary of AAV.EF1a.hAPP (or for Ctrl, saline) stereotactic injection in the LEC. Excitatory cells were targeted for whole-cell current-clamp recordings. AP waveforms of excitatory cells were compared at 12 pA/pF square pulse injections in WT mice from Ctrl and hAPP injected. Aps from the 1st spike in the train are superimposed for comparison.

b. Relationship between AP peak or width in WT mice and AP # during spike trains elicited with a 12 pA/pF current injection.

1789 **c.** Summary data of AP properties. LEC excitatory cells after hAPP injection 1st AP peak (29.36 ±
1790 4.14 mV, 28.62 ± 2.34 mV, hAPP and Ctrl respectively, p=0.87, t=0.17, df=28) and half-width
1791 remains unchanged (1.26 ± 0.10 ms, 1.50 ± 0.13 ms, hAPP and Ctrl respectively, p=0.23, t=1.28,
1792 df=28).
1793 **d.** Summary data of AP properties. LEC excitatory cells after hAPP injection AP threshold
1794 (p=0.18, t= 1.38, df = 28) and AHP remain unchanged (p=0.16, t=1.46, df=28), but dV/dt max
1795 shows a significance increase (399.7 ± 21.82, 331.0 ± 16.71) , hAPP and Ctrl respectively, p=0.02,
1796 t=2.49, df=28).
1797 **e.** Summary data of AP properties. LEC excitatory cells after hAPP injection show unchanged
1798 Resting Membrane Potential (p=0.60, t=0.53, df=28), Accomodation Ratio (p=0.69, t=0.40,
1799 df=28), and Membrane Tau (p=0.08, t=1.84, df=28).
1800 For all summary graphs, data are expressed as mean (± SEM). For **b**: Statistical significance is
1801 denoted as *=p<0.05, as determined by Two-way ANOVA with Sidak's multiple comparison test.
1802 For c, d, e: Individual data points and box plots are displayed. Statistical significance is denoted
1803 as *=p<0.05, as determined by two-tailed unpaired t-test.
1804

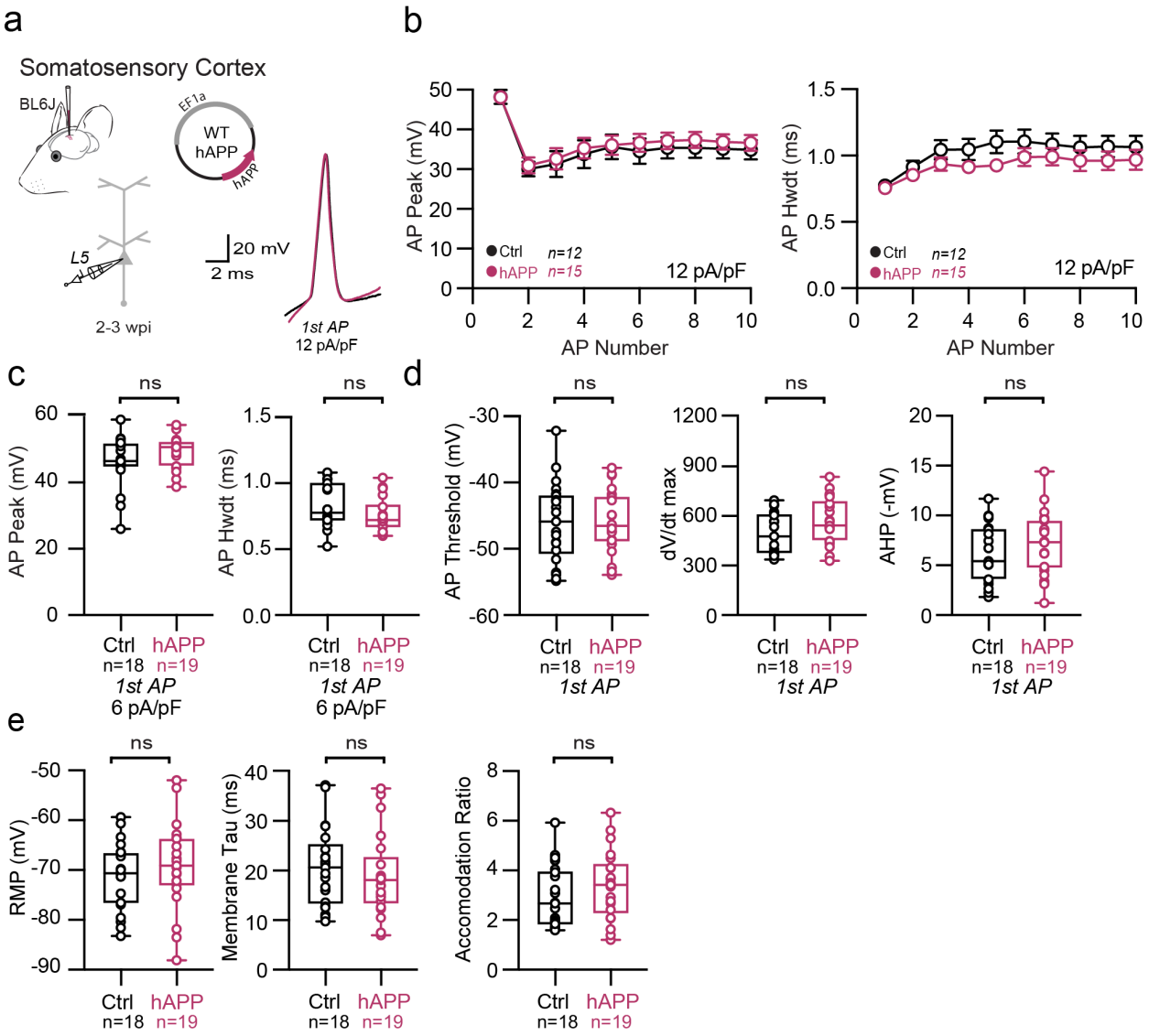

Extended Data Figure 11. Passive and active properties of SS Ctx excitatory neurons after hAPP injection

a. Graphical summary of AAV.EF1a.hAPP (or for Ctrl, saline) stereotactic injection in the SS Ctx. Excitatory cells were targeted for whole-cell current-clamp recordings. AP waveforms of excitatory cells were compared at 12 pA/pF square pulse injections in WT mice from Ctrl and hAPP injected. Aps from the 1st spike in the train are superimposed for comparison.

b. Relationship between AP peak or width in WT mice and AP # during spike trains elicited with a 12 pA/pF current injection.

c. Summary data of AP properties. SS Ctx excitatory cells after hAPP injection 1st AP peak ($p=0.19$, $t=1.34$) and half-width ($p=0.17$, $t=1.41$) ($df=40$) remains unchanged.

1816 **d.** Summary data of AP properties. SS Ctx excitatory cells after hAPP injection AP threshold
1817 (p=0.97, t=0.04, df=40), dV/dt max (p=0.08, t=1.79, df=40), and AHP remain unchanged (p=0.32,
1818 t=1.00, df=40).
1819 **e.** Summary data of AP properties. SS Ctx excitatory cells after hAPP injection show unchanged
1820 Resting Membrane Potential (p=0.37, t=0.90, df=40), Accomodation Ratio (p=0.25, t=1.16,
1821 df=40), and Membrane Tau(p=0.48, t=0.71, df=40).
1822 For all summary graphs, data are expressed as mean (± SEM). For **b**: Statistical significance is
1823 denoted as *=p<0.05, as determined by Two-way ANOVA with Sidak's multiple comparison test.
1824 For c, d, e: Individual data points and box plots are displayed. Statistical significance is denoted
1825 as *=p<0.05, as determined by two-tailed unpaired t-test.
1826

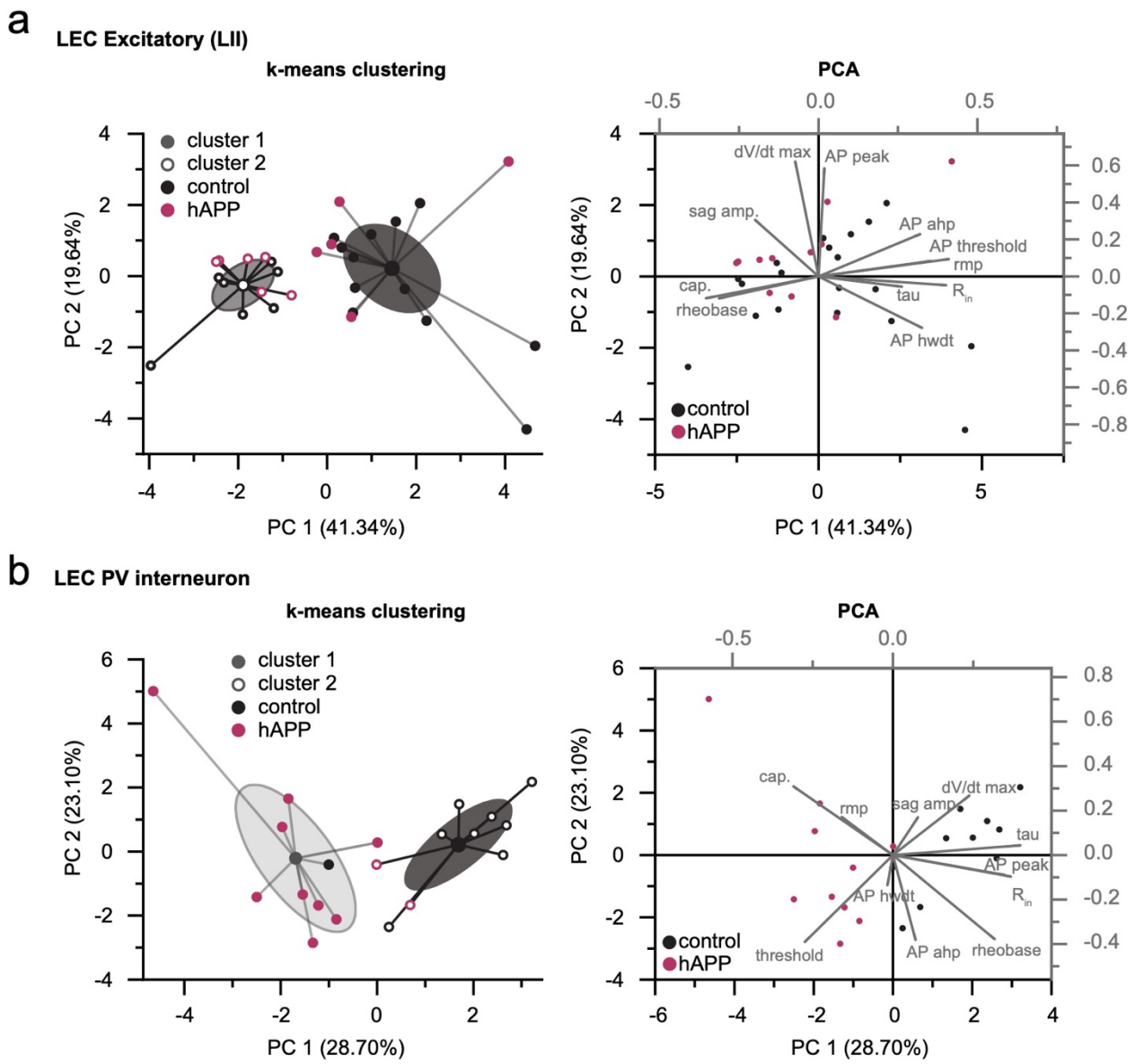

Extended Data Figure 12. PCA analysis of LEC cell populations after hAPP injection

K-means clustering and Principal component analysis (PCA) plot performed on all cells based on active and passive properties for (a) excitatory cells and (b) PV interneurons. a. K-mean clustering fails to separate LEC excitatory cells based on hAPP identity (left), due to largely homogeneous active and passive properties, suggesting differences along different axes. b. Unsupervised clustering preserves hAPP identity in LEC PV interneurons.

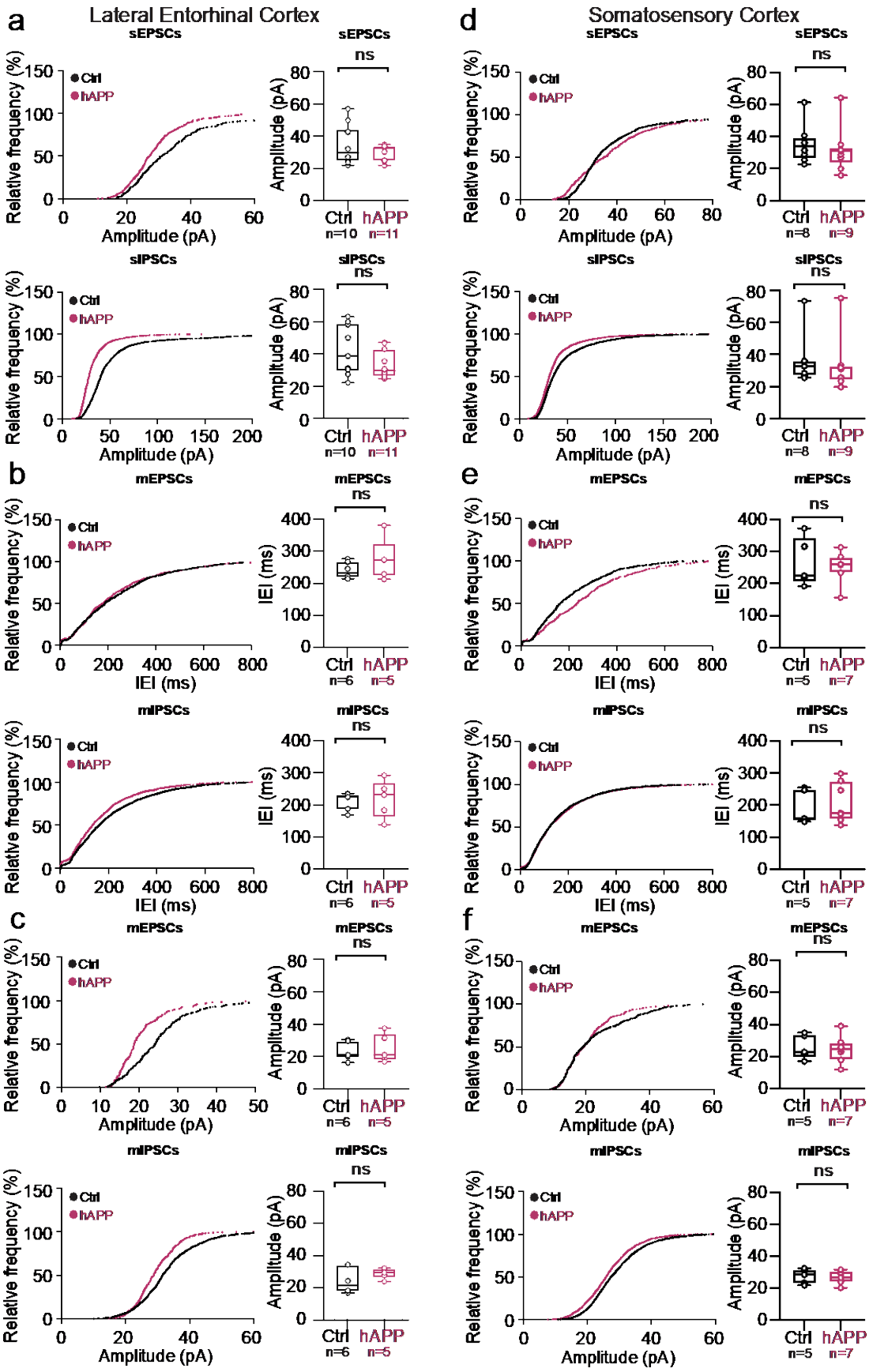
a
Lateral Entorhinal Cortex
sEPSCs
Relative frequency (%)
Amplitude (pA)
Ctrl
hAPP
ns
Ctrl n=10
hAPP n=11
sIPSCs
b
mEPSCs
IEI (ms)
Ctrl n=6
hAPP n=5
mIPSCs
c
d
Somatosensory Cortex
Ctrl n=8
hAPP n=9
e
Ctrl n=5
hAPP n=7
f

1834

1835 **Extended Data Figure 13. Adult-onset human APP does not alter mini frequencies or event**
1836 **kinetics in the LEC or SS Ctx**
1837 **a. Top:** Cumulative distribution curve for spontaneous EPSCs in the LEC showing the relationship
1838 of relative frequency of events to the amplitude (left). Quantified averages of event amplitude are
1839 displayed for each cell as individual data points and compared between Ctrl (black) and hAPP
1840 injected (magenta) conditions (right). L2 LEC sEPSCs showed no amplitude change (p=0.34,
1841 t=0.97, df=19). **Bottom:** Cumulative distribution curve for spontaneous IPSCs in the LEC showing
1842 the relationship of relative frequency of events to the amplitude (left). Quantified averages of event
1843 amplitude are displayed for each cell as individual data points and compared between Ctrl (black)
1844 and hAPP injected (magenta) conditions (right). L2 LEC sIPSCs show an unchanged amplitude
1845 (p=0.11, t=1.66, df=19).
1846 **b. Top:** Cumulative distribution curve for miniature EPSCs in the LEC showing the relationship
1847 of relative frequency of events to the inter-event interval (left). Quantified averages of IEIs are
1848 displayed for each cell as individual data points and compared between Ctrl (black) and hAPP
1849 injected (magenta) conditions (right). L2 LEC mEPSCs show no change in the IEIs (p=0.28,
1850 t=1.16, df=9). **Bottom:** Cumulative distribution curve for miniature IPSCs in the LEC showing
1851 the relationship of relative frequency of events to the IEIs (left). Quantified averages of IEIs are
1852 displayed for each cell as individual data points and compared between Ctrl (black) and hAPP
1853 injected (magenta) conditions (right). L2 LEC mIPSCs show no change in the IEIs (p=0.80, t=0.27,
1854 df=9).
1855 **c. Top:** Cumulative distribution curve for miniature EPSCs in the LEC showing the relationship
1856 of relative frequency of events to the amplitude (left). Quantified averages of event amplitude are
1857 displayed for each cell as individual data points and compared between Ctrl (black) and hAPP
1858 injected (magenta) conditions (right). L2 LEC mEPSCs no amplitude change (p=0.67, 0.45, df=9).
1859 **Bottom:** Cumulative distribution curve for miniature IPSCs in the LEC showing the relationship
1860 of relative frequency of events to the amplitude (left). Quantified averages of event amplitude are
1861 displayed for each cell as individual data points and compared between Ctrl (black) and hAPP
1862 injected (magenta) conditions (right). L2 LEC mIPSCs show an unchanged amplitude (p=0.27,
1863 t=1.18, df=9).
1864 **d. Top:** Cumulative distribution curve for spontaneous EPSCs in the SS Ctx showing the
1865 relationship of relative frequency of events to the amplitude (left). Quantified averages of event

amplitude are displayed for each cell as individual data points and compared between Ctrl (black) and hAPP injected (magenta) conditions (right). L5 SS Ctx sEPSCs no amplitude change (p= 0.57, t=0.59, df=15). **Bottom:** Cumulative distribution curve for spontaneous IPSCs in the SS Ctx showing the relationship of relative frequency of events to the amplitude (left). Quantified averages of event amplitude are displayed for each cell as individual data points and compared between Ctrl (black) and hAPP injected (magenta) conditions (right). L5 SS Ctx sIPSCs show an unchanged amplitude (p=0.75, t=0.33, df=15).

e. Top: Cumulative distribution curve for miniature EPSCs in the SS Ctx showing the relationship of relative frequency of events to the IEIs (left). Quantified averages of IEIs are displayed for each cell as individual data points and compared between Ctrl (black) and hAPP injected (magenta) conditions (right). L2 LEC mEPSCs show no change in the IEIs (p=0.74, t=0.35, df=10). **Bottom:** Cumulative distribution curve for miniature IPSCs in the SS Ctx showing the relationship of relative frequency of events to the IEIs (left). Quantified averages of IEIs are displayed for each cell as individual data points and compared between Ctrl (black) and hAPP injected (magenta) conditions (right). L5 SS Ctx mIPSCs show no change in the IEIs (p=0.65, t=0.47, df=10; mEPSC: p=0.74, t=0.35, df=10).

f. Top: Cumulative distribution curve for miniature EPSCs in the SS Ctx showing the relationship of relative frequency of events to the amplitude (left). Quantified averages of event amplitude are displayed for each cell as individual data points and compared between Ctrl (black) and hAPP injected (magenta) conditions (right). L5 SS Ctx mEPSCs no amplitude change (p=0.77, t=0.31, df=10). **Bottom:** Cumulative distribution curve for miniature IPSCs in the SS Ctx showing the relationship of relative frequency of events to the amplitude (left). Quantified averages of event amplitude are displayed for each cell as individual data points and compared between Ctrl (black) and hAPP injected (magenta) conditions (right). L5 SS Ctx mIPSCs show an unchanged amplitude (p=0.78, t=0.29, df=10).

For a, b, c, d, e, f: Individual data points and box plots are displayed. Statistical significance is denoted as *=p<0.05, as determined by two-tailed unpaired t-test

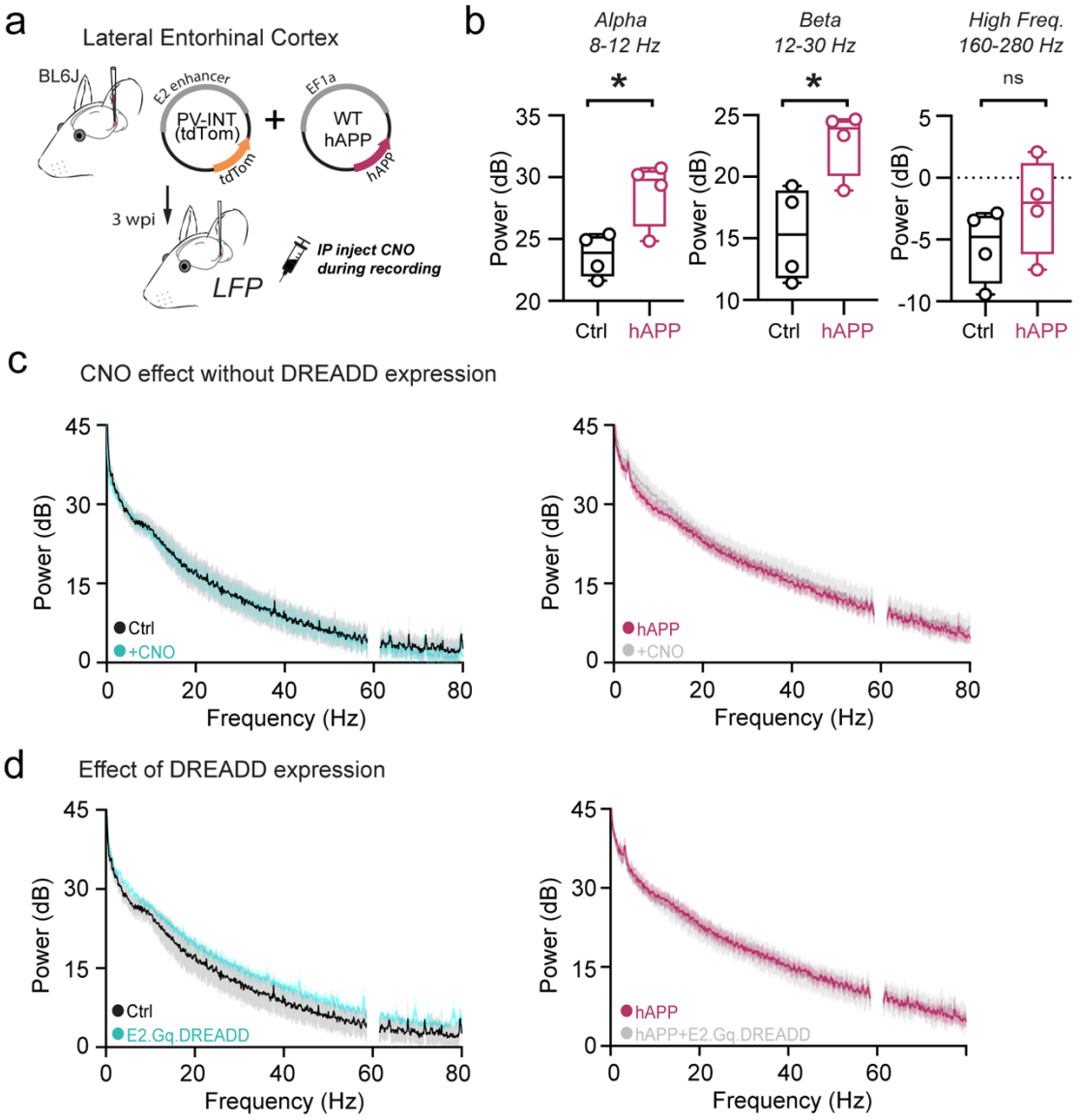

Extended Data Figure 14. DREADD expression or CNO injections alone do not impact LEC circuit excitability

a. Graphical summary of AAV.EF1a.hAPP (or for Ctrl, E2.tdTom) stereotactic injection in the Lateral Entorhinal Cortex.

b. Power [derived from PSD analysis] averaged for each mouse in the Alpha (8-12 Hz), Beta (12-30 Hz), High Frequency (160-280 Hz) frequency ranges and compared between Ctrl and hAPP. Alpha (Ctrl: 23.70± 0.89, Min. 21.64, Max. 25.40, Range. 3.76; hAPP: 28.79 ± 1.35, Min. 24.84, Max. 30.74, Range. 5.90; p=0.020, t=3.15, df=6); Beta (Ctrl: 15.32± 1.93, Min. 11.38, Max. 19.26, Range. 7.88; hAPP: 22.86 ± 1.35, Min. 18.90, Max. 24.67, Range. 5.77; p=0.019, t=3.20, df=6),

High Frequency (Ctrl: -5.47± 1.50, Min. -9.43, Max. -2.87, Range. 6.56; hAPP: -2.34 ± 1.97, Min. -7.43, Max. 2.08, Range. 9.51; p=0.2530, t=1.26, df=6). Individual data points and box plots are displayed. Statistical significance is denoted as *=p<0.05, as determined by two-tailed unpaired t-test.

c. Power Spectral Density [PSD] analysis to assess if CNO administration impacts excitability in the absence of DREADD expression (dark lines: mean, light lines: ±SEM) comparing Ctrl (E2.tdTom+saline injected intracranially) pre- and post- CNO administration (left) or hAPP (E2.tdTom+hAPP injected intracranially) pre- and post CNO administration (right).

d. Power Spectral Density [PSD] analysis to assess if DREADD expression impacts excitability in the absence of CNO administration (dark lines: mean, light lines: ±SEM) comparing Ctrl (E2.tdTom+saline injected intracranially) to Ctrl DREADD (E2.tdTom+ E2.Gq.DREADD+saline injected intracranially) (left) or hAPP (E2.tdTom+hAPP injected intracranially) to hAPP DREADD (E2.tdTom+E2.Gq.DREADD + hAPP injected intracranially) (right).

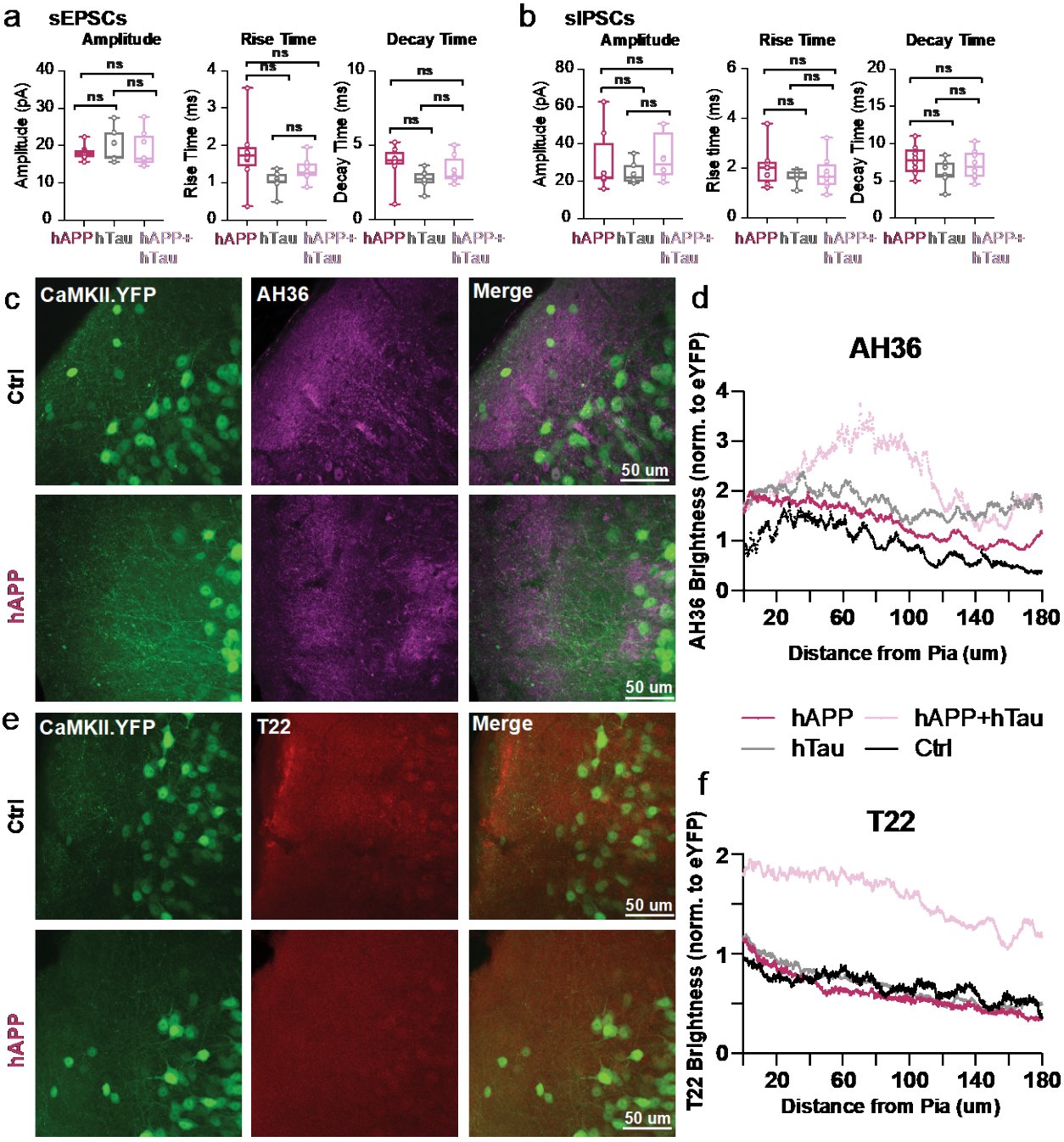

Extended Data Figure 15. hTau co-injection with hAPP spontaneous properties and Ctrl IHC images

a. Summary data of sEPSC properties. sEPSC properties between hAPP injection, hTau injection, or hAPP+hTau injection are not significantly different (Amplitude: hAPP vs. hTau p=0.75, hAPP vs. hAPP+hTau p=0.94, hTau vs. hAPP +hTau p=0.92; Rise Time: hAPP vs. hTau p=0.05, hAPP vs. hAPP+hTau p=0.31, hTau vs. hAPP +hTau p=0.55; Decay Time: hAPP vs. hTau p=0.11, hAPP

vs. hAPP+hTau p=0.54, hTau vs. hAPP +hTau p=0.55; df=20, One-way ANOVA with Multiple Comparisons).

b. Summary data of sIPSC properties. sIPSC amplitudes between hAPP injection, hTau injection, or hAPP+hTau injection are not significantly different (Amplitude: hAPP vs. hTau p=0.69, hAPP vs. hAPP+hTau p=0.88, hTau vs. hAPP +hTau p=0.41; Rise Time: hAPP vs. hTau p=0.39, hAPP vs. hAPP+hTau p=0.65, hTau vs. hAPP +hTau p=0.88; Decay Time: hAPP vs. hTau p=0.21, hAPP vs. hAPP+hTau p=0.76, hTau vs. hAPP +hTau p=0.53; df=20, One-way ANOVA with Multiple Comparisons).

c,e. IHC representative images at 60x magnification for Ctrl (top) or hAPP (bottom) injected mice with staining for either AH36 (c) or T22 (e).

d. Ctrl, hAPP, hTau, and hAPP+hTau were analyzed for AH36 brightness using four line scans in each slice. AH36 brightness was normalized to CaMKII.eYFP brightness to control for any potential variability in viral expression. hAPP+hTau showed the highest level of AH36 brightness, most notably between 40-120 μm from the pia.

f. hAPP, hTau, and hAPP+hTau were analyzed for T22 brightness using four line scans in each slice. AH36 brightness was normalized to CaMKII.eYFP brightness to control for any potential variability in viral expression. hAPP+hTau showed a higher level of T22 brightness, above all other groups which displayed only background levels of T22 positivity.

Extended Data Datasheet 1. Regional-specific PV Proteomics (Attached)

Extended Data Datasheet 2. LEC/SS PV IntegHuman (Attached)

Extended Data Datasheet 3. APP and Tau Interactors (Attached)

Extended Data Datasheet 4. Kavanagh Tau Interactome/PV (Attached)